Kinoshita, M., Tobin, H., Ashi, J., Kimura, G., Lallemant, S., Screaton, E.J., Curewitz, D., Masago, H., Moe, K.T., and the Expedition 314/315/316 Scientists
Proceedings of the Integrated Ocean Drilling Program, Volume 314/315/316

Expedition 316 Site C0007[1]

Expedition 316 Scientists[2]

Chapter contents

Background and objectives

Integrated Ocean Drilling Program (IODP) Site C0007 (proposed Site NT1-03A; Kimura et al., 2007) targets the main frontal thrust at the seaward edge of the accretionary prism (Figs. F1, F2). This site was drilled during IODP Expedition 316 after hole conditions at IODP Site C0006 precluded reaching the main frontal thrust fault. Based on seismic data and submersible studies, this thrust was interpreted to have placed moderately consolidated (and presumably older) clastic rocks over weak and unlithified late Quaternary trench section clastic sediments (Ashi et al., 2002). Site C0007 is located trenchward of Site C0006. At this location, a thrust fault is observed in the seismic section at ~200 meters below seafloor (mbsf), and the frontal thrust is interpreted to occur at ~400 mbsf. The scientific objectives of drilling at Site C0007 are the same as those at Site C0006: to clarify the evolution of the frontal thrust from its birth to death, the function of the frontal thrust with respect to large earthquakes, and the relationship between fluid behavior, slip, and deformation within this fault zone.

Hole C0007D was located ~185 m northwest (upslope) of Hole C0007C to avoid thick gravels encountered in Hole C0007C. The last core recovered from Hole C0007C reached 166.59 m core depth below seafloor (CSF). Because of its upslope position, initiation of coring at 175.00 m CSF in Hole C0007D allowed overlap with equivalent horizons from Hole C0007C, as identified in seismic profiles (Fig. F2).

Core samples from Expedition 316 drilling at this site will be integrated with the existing three-dimensional (3-D) seismic and Site C0006 results to characterize physical properties, strength, composition, and structure of the hanging wall, frontal thrust, and footwall at this site. In situ temperature data were also collected to assess the thermal gradient and heat flow in this area.

Operations

Positioning on Site C0007

The D/V *Chikyu* relocated to Site C0007 (proposed Site NT1-03A) on 13 January 2008. The remotely operated vehicle (ROV) was launched in order to deploy seafloor transponders below the Kuroshio Current (running at 2.0–2.5 kt at the time), the ROV was recovered, and the hydraulic piston coring system (HPCS)/

[1] Expedition 316 Scientists, 2009. Expedition 316 Site C0007. *In* Kinoshita, M., Tobin, H., Ashi, J., Kimura, G., Lallemant, S., Screaton, E.J., Curewitz, D., Masago, H., Moe, K.T., and the Expedition 314/315/316 Scientists, *Proc. IODP,* 314/315/316: Washington, DC (Integrated Ocean Drilling Program Management International, Inc.). doi:10.2204/iodp.proc.314315316.135.2009
[2] Expedition 314/315/316 Scientists' addresses.

doi:10.2204/iodp.proc.314315316.135.2009

extended shoe coring system (ESCS) bottom-hole assembly (BHA) was rigged up and readied while the vessel was calibrating for dynamic positioning system navigation and positioning over the site. The BHA was run to the seafloor, and Hole C0007A (33°01.23258′N, 136°47.94852′E; water depth = 4081 m mud depth below sea level [MSL]) was tagged at 2230 h on 14 January.

Holes C0007A, C0007B, and C0007C

The first core (316-C0007A-1H) was a successful mudline core that penetrated to 3.14 m CSF with 100% recovery. Because of operational and curatorial issues, the following core was labeled Core 316-C0007B-1H. This core was taken from 3.14 m CSF and it recovered 10.06 m of sediment with 105.9% recovery. Because the bit came out of the borehole during recovery of this core and no set standard for hole naming dealt with this issue, the following core was labeled Core 316-C0007C-1H. This core was taken from 12.64 m CSF and recovered 7.95 m of sediment with 100% recovery. All further coring was conducted continuously in Hole C0007C from this point. Cores 316-C0007C-2H through 4H, 5X through 15X, and 16H through 18H were collected with a total recovery of 59.31 m at a rate of 36.29% in interlayered silt, sand, and coarse pebbles. The piston core barrel jammed during collection of Core 316-C0007C-18H at ~1500 h on 17 January 2008, requiring several hours of operational down time and resulting in abandonment of Hole C0007C. The inner core barrel was lost during attempts to recover Core 316-C0007C-18H.

The BHA was pulled out of the hole and recovered between 1200 and 2400 h on 18 January. During this operation, a request was made for permission to drill an alternate hole 185 m northwest of Hole C0007C and permission was granted via the Center for Deep Earth Exploration (CDEX) and the Environmental Protection and Safety Panel (EPSP). Because of consideration of the science target and time requirements, the decision was made to run the rotary core barrel (RCB) coring system. Table **T1** shows the cores collected, meters recovered, and recovery percentage for Holes C0007A, C0007B, and C0007C.

Hole C0007D

After permission to core at Hole C0007D was granted, the vessel was repositioned 185 m northwest of Hole C0007C. The RCB BHA was made up and run in the hole, and Hole C0007D (33°1.3167′N, 136°47.8872′E; water depth = 4049 m MSL) was spudded at 0330 h on 19 January 2008. Jet-in and wash to 18.0 m CSF and drilling to 175.0 m CSF were conducted to the first coring point, which was reached at 1330 h on 19 January. Coring operations in Hole C0007D resulted in the collection of Cores 316-C0007D-1R through 35R (175.0–493.5 m CSF) with total recovery of 87.9 m at a rate of 27.61%. A combination of

- Determination that the primary scientific target had been reached,
- Deteriorating hole conditions,
- Repeated zero-recovery cores, and
- Recovery of small amounts of loose fine sand in the final core (316-C0007D-35R)

resulted in the determination (made at 1500 h on 24 January) to pull out of the hole, kill the hole with dense mud, and recover the BHA to the surface. The BHA was recovered at 0130 h on 25 January. All sea bottom acoustic navigation beacons were recovered from Sites C0006 and C0007, and the vessel moved to Site C0008 (contingency Site NT2-10) on 26 January. Table **T2** shows the cores collected, meters recovered, and recovery percentage for Hole C0007D.

Lithology

Four lithologic units were recognized during examination of cores from Site C0007 (Fig. **F3;** Tables **T3, T4**). Four subunits are recognized in Unit II. Units and subunits are differentiated based on contrasts in grain size, mineralogy, composition, and presence (and thickness) of gravel, sand, and ash layers. In choosing unit boundaries, we also considered biostratigraphic information, paleomagnetic data, X-ray computed tomography (CT) images, observations of structural style, interpretation of seismic data, and LWD data from nearby Site C0006. Deformation within the succession makes the original stratigraphic thickness difficult to determine.

Unit I

Intervals: Sections 316-C0007A-1H-1, 0 cm, through 1H-CC, 27.5 cm; Sections 316-C0007B-1H-1, 0 cm, through 1H-CC, 58.5 cm; and Sections 316-C0007C-1H-1, 0 cm, through 3H-5, 80 cm
Depths: Hole C0007A = 0.00–3.22 m CSF, Hole C0007B = 3.14–13.27 m CSF, and Hole C0007C = 12.64–33.94 m CSF
Age: Pleistocene

The dominant lithology of Unit I is greenish gray silty clay that contains clay minerals, quartz, feldspar, lithic fragments, vitric fragments, and calcareous nannofossils (Fig. **F3A;** Table **T3**). Unit I consists of a fining-upward succession of silty clay, sand, silty sand, and rare volcanic ash layers. Calcite content determined by X-ray diffraction (XRD) is a defining

characteristic of this unit and ranges from 0% to 5.5% and averages ~1%. The mud is internally structureless and locally has green color banding. Sand and silty sand layers are extensively disrupted by probable coring disturbance that in some cases creates mixtures of sand and mud in the upper part of Unit I.

Steepened bedding and faults are present throughout most of this unit (Fig. **F4;** see also **"Structural geology"**). Lower in the unit, thin to thick sand beds with sharp bases and graded tops fine upward into the overlying mud (Fig. **F4**). Generally, sand layers become thinner upward. The sand component is mainly fine to very fine grained and consists of quartz, feldspar, lithic grains, and vitric fragments. Several thick layers (~20 cm) of light olive-gray volcanic ash with abundant pumice fragments are present near the base of the unit. A dark brown ash is present higher in the unit (Fig. **F4**). The contact between Unit I and underlying Unit II is distinguished by the appearance of thick beds of dark gray sand below and the increase in mud content above the unit boundary.

Deposition of this unit occurred on the lowermost slope above the trench floor by hemipelagic settling, turbidite deposition, and possibly subsequent soft sediment slumping on an oversteepened slope.

Unit II

Intervals: Sections 316-C0007C-3H-5, 80 cm, through 17H-CC, 13 cm, and Sections 316-C0007D-1R-1, 0 cm, through 21R-CC, 36 cm

Depths: Hole C0007C = 33.94–159.13 m CSF and Hole C0007D = 175.00–362.26 m CSF

Age: Pleistocene

Unit II is divided into four subunits based mainly on variations in silt, sand, and gravel content (Fig. **F3A;** Tables **T3, T4**). The unit displays a general coarsening-upward trend marked by a progressive increase in silt, sand, and gravel content upsection. Subunits IIA and IIC reoccur at discrete intervals in Holes C0007C and C0007D (Subunits IIAi, IIAii, IIAiii, IICi, and IICii; Fig. **F3A, F3B**). Heterogeneity in XRD data (Tables **T5, T6, T7, T8**) throughout this section can be attributed to the varied lithologies sampled (sand to silty clay; Fig. **F5**).

The repeated subunits within Unit II may be either structural repetitions of the same stratigraphic intervals or recurrences of equivalent facies deposited at different times. For example, spatial concentration of sand and gravel could have been affected by migration of an axial channel across the floor of the trench and/or temporal changes in sediment supply due to fluctuations in sea level.

Subunit IIA

Intervals: Sections 316-C0007C-3H-5, 80 cm, through 8X-2, 98 cm; Sections 316-C0007C-12X-1, 0 cm, through 17H-CC, 13 cm; Sections 316-C0007D-1R-1, 0 cm, through 3R-1, 5 cm; and Sections 316-C0007D-11R-1, 20 cm, through 15R-1, 0 cm

Depths: Hole C0007C = 33.94–73.99 m CSF and 109.59–159.13 m CSF and Hole C0007D = 175.00–190.05 m CSF and 266.20–303.50 m CSF

Age: Pleistocene

Subunit IIA is recognized in three intervals. The upper interval (Subunit IIAi) is present only in Hole C0007C and extends from 33.94 to 73.99 m CSF. The middle interval (Subunit IIAii) is present in Hole C0007C, where it extends from 109.59 to the base of core recovery at 159.13 m CSF, and in Hole C0007D from 175.00 to 190.05 m CSF. The deepest occurrence of this subunit (Subunit IIAiii) is in Hole C0007D and extends from 266.20 to 303.50 m CSF.

The defining characteristic of Subunit IIA is the presence of thick sand and/or gravel. The dominant lithology of Subunit IIAi is olive-gray to dark gray fine-grained sand, consisting dominantly of metamorphic and volcanic lithic fragments with secondary quartz and feldspar. Calcareous nannofossils are almost completely absent from Subunit IIA as shown by the calcite XRD plot (Fig. **F5**). Only two samples contained detectable calcite (0.1% and 0.3%) by XRD.

Individual beds are generally 1–6 m thick and structureless although any original sedimentary structures may have been destroyed by coring. The thickest bed is at least 6.5 m thick (34.00–40.05 m CSF) and contains abundant pumice and scoria fragments (Fig. **F6**). Sand beds typically have sharp bases and grade into olive-gray silt and sometimes greenish gray silty clay with indistinct boundaries between the different lithologies. Silty clay interbeds are typically <1 m thick with minor sandy silt and clayey silt intervals.

The dominant lithology of Subunit IIAii is dark gray fine to very coarse grained sand, consisting dominantly of metamorphic and volcanic lithic fragments with secondary quartz and feldspar. Sand is interbedded with thin olive-gray silty clay and clayey silt. At least one thick (1.7 m) normally graded gravel sequence is present at the base of Hole C0007C with a grain size changing from medium-grade gravel (8–16 mm) at the base to fine sand at the top (Fig. **F7**). The gravel is clast-supported with no obvious matrix and is moderately sorted. Clasts are subrounded to subangular. The clast assemblage

is polymictic with grain types including chert, sandstone, mudstone, mylonitic quartzite, quartz-rich metamorphic, volcanic, and quartzo-feldspathic plutonic lithic fragments (Figs. **F8, F9**). Some clasts have a partial coating of pyrite (Fig. **F7**) that locally appears to have been abraded, indicating that clasts were transported and deposited after the pyrite coating had formed. Assessment of Subunit IIAii was hampered by poor core recovery, possibly indicating substantial loss of sand and gravel during coring.

Subunit IIAiii has a dominant lithology of fine-grained dark gray polymictic gravel (grains 2–5 mm; Fig. **F10**), which fines upward into olive-gray sand and silt. Silty clay interbeds are thin and rare. The clasts in this gravel are similar to those in Subunit IIAii and may be a lateral equivalent of this facies or an older unit of similar source deposited in a similar depositional environment. Overall, poor core recovery makes it difficult to determine if the repetition of Subunit IIA is related to temporal flucuations in channel position or sediment supply or is, in part, structural in nature.

Subunit IIB (outer trench wedge)

Interval: Sections 316-C0007C-8X-2, 98 cm, through 12X-1, 0 cm
Depth: Hole C0007C = 74.00–109.59 m CSF
Age: Pleistocene

Subunit IIB consists of interbedded fine-grained sand, silty sand, and silty clay in approximately equal abundance. Dark gray fine-grained sand and dark olive-gray silt are dominated by metamorphic and volcanic lithic grains with secondary quartz and feldspar, although the proportion of lithic fragments decreases in very fine sand and silt. Calcite content by XRD is minimal, ranging from 0% to 0.1%. Sand is typically <1 m thick and normally graded with indistinct upper boundaries that grade into silty clay. Silty clay is greenish gray and is only slightly bioturbated or mottled in places. Ash horizons are either absent or not recovered in this subunit.

Subunit IIC (marginal trench wedge)

Intervals: Sections 316-C0007D-3R-1, 5 cm, through 11R-1, 20 cm, and Sections 316-C0007D-15R-1, 0 cm, through 17R-3, 79 cm
Depths: Hole C0007D = 190.05–266.20 m CSF and 303.50–326.02 m CSF
Age: Pleistocene

Subunit IIC is recognized in two intervals in Hole C0007D. The upper interval (Subunit IICi) extends from 190.05 to 266.20 m CSF, and the lower interval (Subunit IICii) extends from 303.50 to 326.02 m CSF (Fig. **F3B**). The dominant lithology is greenish gray silty clay, which is interbedded with olive-gray clayey silt and volcanic ash. Many of the silt beds have parallel lamination and diffuse upper boundaries. Ash layers are relatively abundant in comparison with overlying units (Fig. **F11**), particularly near the base of the Subunit IICi, although there may be some repetition of these (see **"Structural geology"**). Mottling and bioturbation are common in both intervals, and *Chondrites* burrows are present in places (Fig. **F12**). A downhole increase in total clay mineral content is observed in Subunit IICi with a corresponding decrease in the relative proportions of quartz and feldspar (Fig. **F5**). Calcite content is also slightly higher (locally up to 4%, averaging ~1%) in Subunit IICi because of the presence of calcareous nannofossils. In comparison to Subunit IICi, Subunit IICii has a slightly higher clay mineral content (average = 52% versus 48% in Subunit IICi), less quartz and plagioclase (22% and 25%, respectively, versus 24% and 27% in Subunit IICi), and calcite is rarely present except at the base of the interval. Incomplete recovery in the upper part of Subunit IICii has hampered this assessment.

Subunit IID

Interval: Sections 316-C0007D17R-3, 79 cm, through 21R-CC, 36 cm
Depth: Hole C0007C = 326.26–362.26 m CSF
Age: Pleistocene

The dominant lithology of Subunit IID is greenish gray silty clay, and minor lithologies include silt and ash. It is discriminated from the overlying subunits of Unit II in part by its higher clay content, averaging 54%. In addition, silt layers are thin-bedded and relatively rare and sand is completely absent. Ash layers are relatively abundant in comparison with overlying units (Fig. **F11**). Silty clay exhibits green (glauconitic?) color bands which increase in frequency toward the base of the subunit. Mottling and slight to moderate bioturbation are common, but positive identification of *Chondrites* burrows is limited to the upper part of the subunit.

Unit II is interpreted as having been deposited in a trench setting with increasing proximity to the axial portion of the trench upsection. The repetition of the axial-channel fill facies (Subunit IIA) indicates either a repetition of the sequence because of thrust faulting or shifting of the position of the trench channel.

Unit III

Interval: Sections 316-C0007D-21R-CC, 36 cm, through 29R-CC, 29 cm
Depth: Hole C0007D = 362.26–439.44 m CSF

Age: Pliocene

Unit III is 77.18 m thick (Fig. **F3B;** Table **T4**), although this thickness is exaggerated by repetition of the unit along thrust faults (see **"Structural geology"**). The unit consists of greenish gray clay and silty clay with interbedded volcanic ash layers, including one occurrence of calcite-cemented tuff. The mud has a clay content substantially higher than overlying Unit II, averaging 65% (Fig. **F5**). In concert with the increased clay mineral content, quartz and plagioclase are diminished, making up only 19% and 15% of the mud, respectively.

In contrast to Subunit IID, Unit III has a greater proportion of volcanic glass reflecting greater ash input, perhaps compounded by lower sedimentation rates. Volcanic ashes range from white, light gray, light greenish gray, to black. They have sharp lower and diffuse upper contacts and are locally burrowed. They consist mainly of glass with minor pumice, quartz, feldspar, and calcareous nannofossils. Black ash includes abundant scoria.

Widespread and diverse bioturbation includes *Zoophycos, Chondrites,* large (>1 cm) subvertical burrows, and other types (Fig. **F12**). Some bioturbation is made visible by color mottling. Green color bands (glauconization?) are also abundant throughout the unit and some display sharp tops. Sand-size glauconite particles are common and dispersed through the mudstones. Small (1 mm) tubular agglutinated tests and possible burrow linings made mostly of volcanic ash particles and concentration of heavy minerals are widely distributed through the unit (Fig. **F12**). Pyrite nodules and pyrite-filled burrows occur throughout the unit (Fig. **F12**).

In contrast to Site C0006, no change in color within this unit has been noted downhole. Smear slide observations indicate that grain size decreases downhole.

Unit III contains lithologies similar to those described in the deep marine Shikoku Basin succession of the western Nankai Trough (Shipboard Scientific Party, 2001a, 2001b; Moore et al., 2001) and was deposited by hemipelagic settling with accumulation of volcanic ash.

Unit IV

Interval: Sections 316-C0007D-29R-CC, 36 cm, through 35R-CC, 19 cm
Depth: Hole C0007D = 439.44–484.44 m CSF
Age: Pleistocene?

Unit IV was encountered below a low-angle thrust fault observed on seismic sections at the site, but only limited recovery was achieved. The presence of thick unconsolidated sand is suggested by the significant increase of drilling penetration rate for the lowermost 3 m of Core 316-C0007D-29R and subsequent cores. Only 25 cm of dark gray sand (Fig. **F13**) and a few drilling-affected mudstone fragments were recovered from Core 316-C0007D-35R. The sand is fine- to medium-grained and consists of abundant black lithic fragments, metamorphic rock fragments, ferromagnesian minerals, quartz, feldspar, and opaque grains. From seismic data and LWD interpretation of equivalent intervals at Site C0006 (see the **"Expedition 314 Site C0006"** chapter), Unit IV is interpreted as the underthrust part of the Pleistocene trench wedge.

Diagenesis

Overall, diagenetic effects observed at this site are minimal. Given the overall low temperature (see **"Physical properties"**), even allowing for uplift, the detrital feldspar assemblage, heavy minerals, and clay mineral assemblage are expected to provide reasonably faithful records of provenance information. Volcanic glass observed at this site is water-clear in transmitted light and shows no discernible evidence of alteration at the scale of smear slide observation.

Only minor evidence of chemical diagenesis could be detected at this site using macroscopic core observation and smear slides. Pyrite in the form of framboids, pyritized burrows, and small (up to 1 cm) nodules is distributed widely through the mud in all of the units and is appreciated most fully in X-ray CT images.

One occurrence of ash cemented by calcite (see **"Lithology"** in the "Expedition 316 Site C0006" chapter for a description of other similar examples) was also encountered in interval 316-C0007D-31R-1, 16–24 cm. Measurements of resistivity and velocity in this sample indicate values far in excess of that observed for silty clays (see **"Physical properties"**).

An interesting petrographic feature of uncertain significance was observed in Unit III. Locally within deformed zones (e.g., Section 316-C0007D-27R-CC; see **"Structural geology"** for further description of this interval), the silt particles (primarily quartz and feldspar) are coated with thin rims composed of highly oriented clay particles (Fig. **F14**). The isopachous rims are ~5–10 µm thick and have a high degree of orientation that is readily observed in crosspolar observation and made starkly visible by use of the gypsum plate. Clays within the silt coatings are aligned with their 001 surfaces approximately parallel to the grain surfaces. In samples that display these clay rims, almost every grain has a rim developed to some degree, though the rims are more readily observed on the larger particles. The rims do not appear to be selective to grain type and are observed on quartz, feldspar, lithic fragments, sponge spicules,

heavy minerals, and opaque grains including pyrite framboids.

X-ray CT number

X-ray CT images were used extensively for evaluation of sedimentological and structural features. Figure F15 shows the depth trends for CT numbers (averaged pixel intensity for a 1 mm² area) determined for coherent rock pieces and tectonic breccia clasts of silt clay. CT number reflects the average sample density at the scale of the CT observation, a value that is affected by sample composition (mineral composition and density) and porosity (bulk density), although in these porous samples, it is largely dominated by the porosity. Throughout Units I and II CT number increases with depth. CT number decreases from 1410 to 1270 in the upper part of Unit III. The lowest value of 1240 in this section is shown at 380 m CSF, and CT number recovers to 1360 at 418 m CSF. This relatively low CT number zone is consistent with the lower clay-dominated part of the site.

Structural geology

Site C0007 yielded a variety of deformation structures, as expected for penetration through the toe of the prism and the frontal thrust. All structural data are given as a supplementary material (see C0007_STRUCT_DATA.XLS in folder 316_STRUCTURE in "Supplementary material"). Where possible, we corrected the measurements of planar and linear structures to true geographic coordinates using paleomagnetic data (see "Structural geology" in the "Expedition 316 methods" chapter). The distribution of planar structures and lithologic divisions with depth is shown in Figure F16. Slump-related structures are observed in lithologic Unit I (0.00–33.94 m CSF). The chief structural features in the prism are subhorizontal bedding and fissility, deformation bands in less sandy portions of lithologic Unit II, healed faults and sediment-filled veins in lithologic Unit III, and three fault zones developed in the hanging wall of the frontal thrust.

Slump-related structures in Unit I

Bedding dips between 20° and 70° in Unit I, in contrast to gently dipping (0°–30°) beds in the prism below (Fig. F16). Bedding dips southeastward after paleomagnetic orientation (Fig. F17A). In places, faults offset bedding with normal or reverse sense of shear and displacement of less than a few centimeters (Fig. F18). Faults show scattered orientations after paleomagnetic correction (Fig. F17B). Sandy layers are locally disturbed and form inclusions in the muddy matrix (Fig. F18). In the extreme case, sandy layers are chaotically mixed with muddy layers. Faults tend to be present near disturbed or chaotically mixed bedding. These features and large variations in bedding attitude most likely record slumping of sediments above the prism.

Deformation structures in the prism

Bedding and fissility (foliation parallel to bedding) dip gently (generally ~30°) throughout the prism (Fig. F16). The orientations of bedding and fissility after paleomagnetic correction are shown in Figure F19. Deformation features are not present in Unit II where sediments are dominated by coarser-grained material such as sands and gravels. Deformation structures are concentrated in mudstone-dominated Units II and III.

Deformation bands

Deformation bands are developed in portions of Unit II where fissility is well developed in nonbioturbated mudstone (Fig. F16B; C0007_STRUCT_DATA.XLS in folder 316_STRUCTURE in "Supplementary material"). In the cores, bands are defined by bedding oblique dark bands that change in thickness from ~1 to 5 mm along their length. Typically, deformation bands occur as two sets that dip in opposite directions, and one of the bisectors of the dihedral angle (~90°) is oriented parallel to the bedding-parallel fissility (Fig. F20A, F20B). Where there is offset between these two sets of deformation bands, shear sense is always reverse and displacement is less than a few millimeters. These features clearly indicate that deformation bands were formed by layer-parallel contraction. The orientations of deformation bands after paleomagnetic correction predominantly strike northeast (Fig. F21).

On X-ray CT images, deformation bands are displayed as bright bands or seams with relatively high CT numbers (Fig. F20C). This suggests that the bands are denser than the surrounding material. Overall, structural features seen in cores and CT images are consistent with those observed at Site C0006 (see "Structural geology" in the "Expedition 316 Site C0006" chapter) and deformation bands in the Muroto transect in the Nankai accretionary prism (e.g., Ujiie et al., 2004), which were formed by northwest-directed plate convergence–related tectonic deformation in the accretionary prism.

Healed faults and sediment-filled veins

Healed faults and sediment-filled veins are observed in Unit III where bioturbation is well developed in hemipelagic mudstone. Two types of healed faults are recognized in the cores. One type of healed fault

is defined by dark seams <1 mm thick that dip between 30° and 90°. The faults are braided and curviplanar to irregular. Where offset markers occur, the sense of shear is always normal (Fig. F22A). The orientations of these healed faults, after paleomagnetic correction, exhibit random strike (Fig. F22B). This type of healed fault is similar to that reported in the hemipelagic mudstone at the base of Site C0006 (see "Structural geology" in the "Expedition 316 Site C0006" chapter) and in the Muroto transect in the Nankai accretionary prism (Moore, Taira, Klaus, et al., 2001) and is thought to result from vertical compaction of sediments during burial.

The other type of healed fault is defined by dark bands generally <5 mm thick, which are parallel or subparallel to bedding (dips <30°). The orientations of these healed faults after paleomagnetic correction predominantly dip southward (Fig. F22C). The bedding-parallel or subparallel occurrence of the healed faults is similar to layer-parallel faults observed in mudstone in the accretionary prism on land (Hanamura and Ogawa, 1993). The origin of this type of healed fault is controversial; it either developed as slip surface associated with slumping or resulted from thrust faulting during frontal accretion.

Sediment-filled veins are recognized as parallel sets of sigmoidal or planar seams generally less than a few millimeters wide (Fig. F23) that tend to extend perpendicular to bedding with length ranging from 1 to 28 cm. Some sediment-filled veins offset bedding or greenish layers and show normal slip with displacement less than a few millimeters.

Fault zones

Three fault zones were identified in the prism of Hole C0007D (Fig. F16B) based on the following criteria:

- Rocks are broken along polished and striated fracture surfaces with spacing of fractures <10 cm.
- Preservation of fault breccia and fault gouge. The size of brecciated fragments is ~1–10 mm.
- Changes in lithology, deformation style, and kinematics of structures with depth.

Outside fault zones, rocks are not brecciated except for drilling-induced brecciation (see definition of drilling-induced breccia in "Structural geology" in the "Expedition 316 methods" chapter) and the spacing of natural fractures is >10 cm.

Fault Zone 1 (237.5–259.3 m CSF)

The structural elements in fault Zone 1 are shown in Figure F24. Rock in fault Zone 1 is predominately fractured. Fault breccias are 17–19 cm thick and are characterized by angular to subangular fragments 1–10 mm in size (Fig. F25). Brecciated fragments are commonly polished and slickenlined and lineations indicate multiple slip directions. The 21.8 m thick fault Zone 1 is developed in the muddy portion of Unit II and is located just above the sand- and gravel-dominated portion of Unit II (Fig. F16). Deformation bands, which are developed in Unit II between 230 and 248 m CSF, are absent below fault Zone 1, consistent with a change in lithology across fault Zone 1. These features suggest that fault Zone 1 is related to the thrust faulting that places mudstone onto sands and gravels.

The prominent feature in fault Zone 1 is preservation of light grayish ash layers. On CT images, three such ash layers are similar in character (see also "Lithology"). They are recognized as dark layers bounded above and below by bright layers (Fig. F24). The thicknesses of the ash layers are similar: 15, 10, and 12 cm from lowest to highest in depth. Occurrence of these similar ash layers may simply indicate the deposition of volcanic ash at three different times. Alternatively, the three ash layers within fault Zone 1 may reflect a repetition of the same layer by thrust faulting.

Fault Zone 2 (341.5–362.3 m CSF)

Fault Zone 2 is located where lithology changes from mudstone in Unit II to bioturbated hemipelagic mudstone in Unit III (Fig. F16B). The location of this zone is comparable to the interval where a subhorizontal strong reflector is recognized in a nearby seismic line (Fig. F2). The structural elements in fault Zone 2 are shown in Figure F26 and consist mostly of fractured rocks characterized by fragmentation along sets of polished and striated surfaces (Fig. F27A). Concentration of deformation at the bottom of fault Zone 2 is indicated by occurrence of breccia and fault gouge (Fig. F27B). Fault breccia includes subangular to rounded fragments ~1 mm–2 cm in size and a random texture. Fault breccia is replaced by fault gouge at 362.1 m CSF. This change is marked by a decrease in size and volume fraction of fragments to <2 mm and 30%, respectively. Fault gouge is weakly foliated and the angle between a foliation defined by alignment of fragments and the horizontal plane is 38°.

It is possible that fault breccia and fault gouge have been affected by drilling-related deformation because they are often recovered within the core catcher. However, in this hole, the core below is characterized by relatively unbroken hemipelagic mudstone, showing an asymmetric distribution of fractured rocks with respect to fault breccia/fault gouge zone. As in the case of fault Zone 1, deformation bands are concentrated above fault Zone 2 and

band kinematics show reverse slip associated with northwest-directed contraction (Figs. F16B, F20, F21). Deformation bands are absent below fault Zone 2, but healed faults are well developed and show normal slip consistent with vertical compaction of sediments during burial (Fig. F22). The changes in deformation style and kinematics of structures across fault Zone 2, as well as the asymmetric distribution of fractured rock, suggest that the major slip zone is located at the bottom of fault Zone 2, possibly represented by the fault breccia/fault gouge zone. Although distribution of deformation bands could be controlled by lithology, it is also possible that deformation bands record stress concentration in the hanging wall of the fault.

Fault Zone 3 (398.5–446.0 m CSF)

Fault Zone 3 is located at the basal part of the prism above the frontal thrust that juxtaposes the hemipelagic mudstone (Unit III) above and sand-dominated sediments (Unit IV) below. The structural elements of fault Zone 3 are shown in Figure F28. This zone is marked by a heterogeneous distribution of fractured and brecciated hemipelagic mudstone (Fig. F29). Despite intense fracturing, bedding has not been rotated significantly along the fractures. Fractures commonly have polished and slickenlined surfaces, and steps on the surfaces were used to determine shear direction and shear sense. The orientations of fracture surfaces after paleomagnetic correction are scattered with complex and heterogeneous slip directions and shear senses (Fig. F30).

Two zones of concentrated deformation are recognized within fault Zone 3: one contains a foliated fault gouge at 418.83–418.94 m CSF, and the other contains a 2 mm thick dark layer at 438.57 m CSF. The fault gouge at 418.83–418.94 m CSF was recovered in the core catcher and thus could be affected by drilling-related deformation. Despite this fact, the core sample preserves a foliation defined by an alignment of <1 mm size fragments in a clayey matrix and color banding (Fig. F31). The dip direction of the foliation changes across a drilling-induced biscuit boundary, suggesting that the foliation was formed prior to drilling and is a product of natural shear deformation. The foliation is cut by slip surfaces, imparting a composite planar fabric (Chester and Logan, 1987). The shear sense of fault gouge indicated by this composite planar fabric is consistent with thrust faulting. In places, fragments are surrounded by anastomosing slip surfaces.

The lowermost part of fault Zone 3 at 438.28–438.57 m CSF is intensely brecciated into fragments ~1–10 mm in size (Fig. F32A, F32B). This 29 cm thick breccia shows a foliated aspect from an anastomosing network of polished and striated surfaces. At the base of this zone, the 2 mm thick dark layer sharply separates intensely brecciated hemipelagic mudstone above from unbroken hemipelagic mudstone and ash below (Fig. F32C). There is a biostratigraphic age reversal across the lowermost part of fault Zone 3; an intensely brecciated interval above is older than the coherent sediments below (see "Biostratigraphy"). These features indicate that the thin dark layer most likely represents extreme localization of slip associated with thrust faulting.

Biostratigraphy

The biostratigraphy determined for Site C0007 was based on examination of calcareous nannofossils, radiolarians, and foraminifers from Holes C0007C and C0007D.

Calcareous nannofossils

Sediments recovered from Holes C0007C and C0007D are dominated by interbedded sand layers and volcanic ash layers (see "Lithology"), yielding few to rare and moderate to poorly preserved nannofossils in most samples from core catchers and cores. This deficiency results in difficulties establishing the biostratigraphy, including few nannofossils, poor preservation, and reworking. To solve these problems, we used the same methods as those used at Site C0006 (see "Biostratigraphy" in the "Expedition 316 Site C0006" chapter), allowing us to obtain common to abundant nannofossils from a number of samples (Tables T9, T10).

For Hole C0007C, two nannofossil biostratigraphic events were recognized (Table T11). The uppermost Sample 316-C0007C-1H-CC, 7.0–12.0 cm, contains common *Pseudoemiliania lacunosa;* therefore, this sample was assigned to Zone NN19. Sample 316-C0007C-14X-CC, 24 cm, contains dominant *Gephyrocapsa* spp. medium I and medium II but rare *P. lacunosa*. This case has been commonly observed in Zone NN20 nannofossil assemblages in the Pacific warm regions where rare *P. lacunosa* is present as reworked in Zone NN20 assemblages. This sample was therefore assigned to Zone NN20. Common *P. lacunosa* occurs again in Sample 316-C0007C-15X-CC, marking its "repeated" last occurrence (LO) in this horizon (Fig. F33). The Zone NN20 sediments and the repeated LO of *P. lacunosa* suggest a possible disturbance of the sediment sequence. Core 316-C0007C-17H contains gravels in which no nannofossils were available.

In Hole C0007D, a total of 17 nannofossil biostratigraphic events were recognized: 7 Pleistocene Zone NN19 events and 10 Pliocene Zone NN16–NN12 events, including 3 possible repeated events (Table

T11). Based on these events, three repeated intervals and one age gap were recognized (Fig. F33).

The uppermost repeated event is the LO of *P. lacunosa* at 138 m CSF. The normal LO of *P. lacunosa* was observed in Sample 316-C0007C-1H-CC, 7.0–12.0 cm. However, a repeated LO of *P. lacunosa* was seen in Sample 316-C0007C-15X-CC. In Hole C0007D, a few *P. lacunosa* specimens were found in Sample 316-C0007D-1R-CC, 0–5 cm, but they are common in Sample 316-C0007D-1R-CC, 10 cm. These samples contain abundant *Gephyrocapsa* spp. medium I and medium II, which are the dominant species in Zone NN20 and common in the uppermost part of Zone NN19. It is reasonable to consider the common occurrence of *P. lacunosa* in Sample 316-C0007D-1R-CC, 0–5 cm, as the repeated LO, in correlation with the repeated LO of *P. lacunosa* at 138 m CSF in Hole C0007C. The repeated LO of *P. lacunosa* indicates an age reversal, probably caused by faulting.

Determination of the reentrance (RE) of *Gephyrocapsa* spp. (≥4 µm) was somewhat difficult because the record of the RE of this group was interrupted by samples lacking fossils or poor preservation and by faulting (Table T10). However, the records of this *Gephyrocapsa* group suggest one "normal" sequence to 249.46 m CSF and another sequence from 266.57 to 305.82 m CSF. Therefore, we placed the normal RE of *Gephyrocapsa* spp. (≥4 µm) at 249.46 m CSF and considered the lowest RE of *Gephyrocapsa* spp. (≥4 µm) at 305.82 m CSF as repeated. This conclusion is in reasonable accord with the results from seismic and structural studies. The first fault zone (fault Zone 1 in Fig. F33) in Hole C0007D was observed between 237.50 and 259.30 m CSF (see **"Structural geology"**). The repetition of the RE of *Gephyrocapsa* spp. (≥4 µm) might be caused by this fault.

The lower part of Zone NN19, marked by the base of a middle Zone NN19 event, the first consistent occurrence (FCO) of *Gephyrocapsa* spp. large (>5.5 µm), was truncated by a number of late Pliocene events: the LOs of *Discoaster brouweri* (marker of Zone NN18), *Discoaster pentaradiatus* (marker of Zone NN17), and *Discoaster surculus* (marker of Zone NN16) at 361.79 m CSF (Tables T10, T11; Fig. F33), indicating the absence of the lower part of lower Pleistocene Zone NN19 and upper Pliocene Zones NN18 and NN17. We noted a similar truncation in the same time interval at Sites C0004 and C0006 (see **"Biostratigraphy"** in the "Expedition 316 Site C0004" chapter and **"Biostratigraphy"** in the "Expedition 316 Site C0006" chapter) but lack an explanation at the present time. For Site C0007, this age gap is correlated with a second fault zone (fault Zone 2 in Fig. F33) between 341.50 and 362.30 m CSF in Hole C0007D (see **"Structural geology"**).

The interval from 362.15 to 376.17 m CSF in Hole C0007D was assigned to middle Pliocene calcareous nannofossil Zone NN16, based on the co-occurrence of *D. surculus* (marker of the top of Zone NN16) and *Discoaster tamalis,* as well as the absence of *Reticulofenestra pseudoumbilicus* (>7 µm) (marker of top of Zones NN15–NN14) (Table T10). Recognition of the LO of *Sphenolithus* spp. at 370.88 m CSF provides a subdivision of this zone. The moderate numbers of *R. pseudoumbilicus* at this horizon were considered to be reworked, as this species occurs commonly as reworked in the sequence above. The interval from 370.88 to 390.35 m CSF was assigned to lower Pliocene Zones NN15–NN14 with its top marked by the LO of *R. pseudoumbilicus* (>7 µm) and its bottom marked by the presence of *D. asymmetricus* (marker of base of Zones NN15–NN14). The rare presence of *Ceratolithus acutus* at 409.93 m CSF was taken as the reliable LO of this species, whereas its trace and sporadic presence in the upper sequence of Hole C0007D was considered to be due to reworking. This phenomenon subdivides Zone NN13. The lowest occurrence of the *Ceratolithus rugosus* (marker of Zone NN13/NN12 boundary) at 418.38 m CSF was considered as its FO, marking the boundary between Zones NN13 and NN12. The sequence from 418.78 to 438.13 m CSF was assigned to Zone NN12, according to continuous occurrence of *C. acutus* (FO = 5.32 Ma) in this interval and the absence of *D. quinqueramus* (marker of top of Zone NN11; LO = 5.59 Ma).

An age reversal was seen in the interval from 438.24 to 438.61 m CSF in Core 316-C0007D-29R (Fig. F34), where sediments were fractured and brecciated by faulting (fault Zone 3 in Fig. F33) (see **"Structural geology"**). The occurrence of *C. acutus,* together with the common presence of *R. pseudoumbilicus* and *Sphenolithus* spp. in Sample 316-C0007D-29R-2, 33 cm, and in samples above (e.g., Sample 316-C0007D-29R-1, 16 cm), suggests a Zone NN12 age (or ~5.32 Ma) for this horizon. On the other hand, the nannofossil assemblage in Sample 316-C0007D-29R-2, 70 cm, and the two samples below suggest a Zone NN16 assemblage, characterized by the common presence of *P. lacunosa* and *Sphenolithus* spp., trace but continuous *D. tamalis,* and lack of a reliable presence of *R. pseudoumbilicus*. Thus, the sediment ages change from Zones NN12 to NN16 in this 37 cm interval. This age reversal in coordination with the results of structural studies implies a significant sequence disturbance by faulting. To estimate the time difference, we took the occurrence of *Sphenolithus* spp. in this horizon as its repeated LO (3.65 Ma) in the top of the reversed sequence, giving an estimate of ~1.67 m.y.

Age assignment was not possible for samples below 439.39 m CSF because of lack of fossils (Sample 316-

C0007-34R-CC) or uncertainty whether samples were in situ or fallen pieces (Samples 316-C0007-30R-CC, 31R-CC, and 35R-CC; see "Lithology").

Other microfossil groups

All core catcher samples were processed for radiolarian analysis, but most of them were barren. Sample 316-C0007A-1H-CC revealed a moderately preserved assemblage of radiolarians, some foraminifers, and a few broken diatom frustules. In Sample 316-C0007-15X-CC, abundant diatom frustule fragments and a few broken radiolarian shells and foraminifers were observed. Discrete horizons within cores were also sampled for diatoms and radiolarians, but those that were not barren revealed only very rare broken diatom frustules.

Summary

A total of 19 nannofossil biostratigraphic events were recognized in sediments recovered from Site C0007, which were then assigned an age of Pliocene Zone NN12–NN20. The uppermost sediments at this site might contain a thin Holocene deposit; however, it is not possible to determine the age of this interval by means of nannofossil biostratigraphy. Plots of age versus depth for Holes C0007C and C0007D were combined with magnetostratigraphic results from the same hole (Fig. F33).

Three age reversals and an age gap were suggested by the nannofossil record and may be caused by faulting.

Paleomagnetism

Pass-through magnetometer measurements on all split-core archive sections were made at 5 cm intervals. Archive half cores were demagnetized to 40 mT using alternating-field (AF) demagnetization. Before the measurement data were uploaded to the J-CORES database, we excluded data from voids and from the top and bottom ~15 cm to avoid end-core edge effects. We demagnetized a total of 88 discrete samples using both AF and thermal demagnetization techniques in order to test the half-core data and to identify magnetic carriers.

Natural remanent magnetization and magnetic susceptibility

Downhole variations of paleomagnetic data obtained at Site C0007 are shown in Figures F35 and F36. As in previous sites, drilling-induced remagnetization exists in the recovered cores (Figs. F35, F36, F37). However, we noticed that in cores drilled using a nonrotary core barrel, especially in those drilled using the ESCS (i.e., Cores 316-C0007B-5X though 15X, 43.00–138.18 m CSF), drilling has very little effect on magnetic declination but significantly affects magnetic inclination and natural remanent magnetization (NRM) intensity (Fig. F36). In almost all cases, we were able to remove drilling-induced remagnetization with 20 mT AF demagnetization and to isolate the characteristic remanent magnetization (ChRM) direction using higher fields.

Variations of magnetic properties among various lithologies are similar to those observed at Site C0006. In the nannofossil-bearing mud and sand cores in lithologic Unit I, both NRM intensity and magnetic susceptibility show a steady downhole increase with an average intensity of 5 mA/m and susceptibility value of 60×10^{-3} SI units. Pleistocene aged sediments in Unit II have relatively high NRM intensity (average = 15 mA/m) and magnetic susceptibility (~190×10^{-3} SI units). These are caused by the presence of numerous volcanic ash and sand layers throughout this unit, which have relatively high concentrations of magnetic minerals. Recovered cores in Unit III are hemipelagic mudstone and have the lowest NRM intensity (mean = ~0.25 mA/m) and magnetic susceptibility (mean = ~9×10^{-3} SI units). Poor recovery of the underthrust trench wedge type sands and rocks in Unit IV limits paleomagnetic work, although a few pass-through whole-core magnetic susceptibility measurements give an indication for relatively high susceptibility values (>300×10^{-3} SI units) (Fig. F36).

There are more significant variations in susceptibility within Unit II than Unit III. In particular, magnetic susceptibility records at both drilled locations in Site C0007 (i.e., Hole C0007C at ~159 m CSF and Hole C0007D at ~190 m CSF) show a similar discrete trough of lower susceptibility values, confirming the accuracy of the subunit boundaries defined by shipboard sedimentologists and also suggesting that this magnetic susceptibility trough can be used for stratigraphic correlation.

Discrete samples and core orientation

Remanent magnetization of discrete samples were investigated using stepwise AF or thermal demagnetization (Fig. F37). The steep downward component of magnetization imparted by the coring process can be removed by both demagnetization techniques, but thermal demagnetization appears to be more effective in removing this drilling-induced component (Fig. F37). Most samples show unblocking temperatures between 200° and 400°C, indicating that titanomagnetites are likely the main magnetic carriers in these samples. A histogram of inclinations isolated from the 88 discrete samples is shown in Figure F38. Inclinations from these discrete samples are

mostly concentrated at 52° (Fig. F38), suggesting these samples maintain an inclination close to the theoretically predicted value for the latitude of this site (52°) and indicating they may represent the primary ChRM. As with previous sites, results from discrete sample demagnetization in combination with the pass-through sample results were used to reorient core pieces to a common geographic framework. We used either the stable ChRM isolated from progressive demagnetization of discrete samples and small homogeneous segments (that contain structural features) or an average declination from 3–4 consecutive measurement intervals with the same inclination sign from the archive half core data.

Magnetostratigraphy

We used ChRM inclinations from both pass-through and discrete measurements to define magnetic polarity sequences for Site C0007 (Fig. F39). Faulting and incomplete recovery affect and complicate the magnetostratigraphy at this site. Nevertheless, a few magnetic reversals identified on the basis of changes in sign of inclinations can be identified. Because biostratigraphic samples in the depth interval between 5 and 20 m CSF in Hole C0007C have been assigned ages ~0.43 Ma, the observed negative inclinations between 10.81 and 13.92 m CSF (Fig. F35) suggest that these sediments were deposited within the Emperor event (0.42 Ma), a short reversal within the upper part of the Brunhes normal chron according to the Vostok ice core data (Gradstein et al., 2004).

Shipboard biostratigraphic data suggest that sediments between 200 and 320 m CSF in Hole C0007D are 0.8–1.1 Ma. This information suggests that the relatively well defined record of change in polarity from normal to reversed at ~210 m CSF represents the Brunhes/Matuyama Chron boundary (0.78 Ma), and the shift in polarity from reversed to normal at ~330 m CSF represents the end of the Jaramillo normal polarity subchron (1.07 Ma). Below 360 m CSF, a dominantly normal polarity sequence extends to at least 410 m CSF (Fig. F39). This normal polarity sequence appears to correspond to the Gauss normal chron as nannofossil biostratigraphic Zones NN15/NN14 and NN13 are also placed in this depth interval (see **"Biostratigraphy"**). At least three thrust faults are inferred in this depth interval (Fig. F39) (see **"Structural geology"**), preventing more precise reconstruction of the magnetostratigraphy.

Inorganic geochemistry

The main objectives of the geochemical program at Site C0007 are to

- Characterize in situ biogeochemical reactions;
- Constrain in situ inorganic diagenetic reactions with depth;
- Identify potential deep-sourced fluids within fault zones and other permeable horizons, as well as fluid-sediment reactions at the source; and
- Constrain the subsurface hydrology, including fluid flow pathways and possible transport mechanisms.

A total of 40 whole-round samples were collected for interstitial water analyses at Site C0007 (2 from Hole C0007A, 2 from Hole C0007B, 12 from Hole C00007C, and 24 from Hole C0007D). Holes C0007A, C0007B, and C0007C actually constitute one hole, and the three different designations were a clerical error; thus, they are combined on figures designated Hole C0007C in this report. Whole-round lengths ranged from 11 to 44 cm with longer sections taken in and adjacent to fault zones. Samples were collected at a higher spatial resolution in the uppermost 30 m to constrain the dominant microbially mediated reactions occurring within the shallow sediments at this site and identify the presence or absence of anaerobic oxidation of methane (AOM) at the sulfate-methane transition (SMT). Below Core 316-C0007C-3H, one sample was taken per core if recovery was sufficient. The main geochemical objectives below the region of most intense organic matter degradation in Holes C0007C and C0007D were to identify the main in situ diagenetic reactions in the sediment section and identify any exotic/deeper-sourced fluids along the fault zones. This was done through analysis of dissolved elements that reflect inorganic fluid-rock reactions or microbially mediated reactions.

The SMT was not recovered at Site C0007. Sulfate reduction is relatively rapid in the upper ~20 m of the sediment section of Hole C0007C; however, sulfate never reaches depletion and increases toward the bottom of Hole C0007C. Within the first cores from Hole C0007D (only ~20 m below the base of Hole C0007C), sulfate is totally depleted with localized horizons of elevated sulfate. Because we did not recover this geochemical boundary, it is difficult to ascertain whether slight variations in sulfate are the result of drill water contamination or if they reflect in situ pore water sulfate. Thus, pore fluid elemental concentrations were not corrected for drilling contamination based on dissolved SO_4 concentration at this site. Uncorrected concentrations of all of the elements analyzed are presented in Tables **T12, T13,** and **T14,** and the corresponding chemical and isotopic profiles are presented in Figures **F40, F41, F42, F43, F44, F45,** and **F46.**

Sulfate concentration ranges between 8 mM and near-seawater value in Hole C0007C. Typically, sulfate is depleted in the upper sediment section as a result of microbial reduction of sulfate by organic matter oxidation and, in some cases, methane oxidation. Enrichments in sulfate below the SMT therefore indicate pore fluid contamination during the core recovery process. Thus, in Hole C0007C it is difficult to determine if a fraction of pore fluids collected throughout the hole have been compromised by drill water contamination. All of the whole rounds collected, except Section 316-C0007-16H-2 at 149.1 m CSF, were clay-rich or silty clay lithologies and are therefore considered to have a low likelihood of contamination. All samples from Hole C0007C were collected using the HPCS. HPCS cores are typically not contaminated by drilling fluid because they are collected ahead of the drill bit. The most suspect of the pore water samples is Sample 316-C0007-16H-2, collected at 149.1 m CSF. Sample 316-C0007-16H-2 is a fine-grained sand, and many of the major and minor elements approach seawater value in this section. However, this sample was bounded by >1 m clay sections above and below, precluding significant flushing with drill water or seawater during core recovery. Furthermore, there is a lack of evidence of sulfate depletion based on the CH_4 concentration profile throughout Hole C0007C; CH_4 concentration remains near the detection limit (see **"Organic geochemistry"**). Because we have these reasons to believe that samples throughout Hole C0007C might be representative of in situ pore fluids, we present data in this report uncorrected; however, these data should be viewed with caution. Postcruise analyses will focus on constraining whether the elevated SO_4 is an artifact of drill water contamination or reflects in situ SO_4. As discussed below, low sulfate concentration was measured in Hole C0007D. Because these samples were collected with the RCB, it is likely the measured sulfate reflects a small amount of seawater contamination.

Because of the paucity of argon, which is used as a carrier gas for both inductively coupled plasma–atomic emission spectroscopy (ICP-AES) and inductively coupled plasma–mass spectrometry (ICP-MS) analyses, at the time of drilling Site C0007, the ICP-MS measurement program was halted for the remainder of Expedition 316. This ensured that there was enough argon available to measure the major and minor element concentrations via ICP-AES at all sites. Trace elements (V, Cu, Zn, Rb, Mo, Cs, Pb, U, and Y) were subsequently determined via shore-based ICP-MS, and $\delta^{18}O$ was analyzed onshore by isotope ratio mass spectrometry. Trace metal and $\delta^{18}O$ data are presented in Table **T14.**

Salinity, chloride, and sodium

Pore fluid salinity generally decreases with depth from 35.33 at 1.5 m CSF to 33.23 at the base of Hole C0007D (437.0 m CSF). Superimposed on this general salinity trend are three excursions. The first is characterized by a relatively rapid decrease in salinity from 35.33 at 1.5 m CSF to 34.22 at 17.0 m CSF. This initial decrease in salinity reflects active SO_4 reduction, which consumes pore fluid SO_4 and precipitates Ca and minor Mg in authigenic carbonates (Figs. **F41C, F43A, F43B**). The second excursion is typified by an increase in salinity from 34.28 at 102.7 m CSF to 35.44 at 149.1 m CSF, indicating a change to more seawater-like values within this depth interval. Salinity then decreases from the base of Hole C0007C to 32.83 at the top of Hole C0007D. The third excursion in the salinity profile is manifested by a sharp decrease from 32.39 at 314.2 m CSF to 29.33 at 325.5 m CSF coincident with minima in the Cl, Na, Br, and Sr profiles.

Chloride varies from 1.5 to 33.0 m CSF in Hole C0007C, ranging from 551 to 559 mM (Fig. **F40B**). Chloride then remains fairly constant to the base of Hole C0007D, ranging from 540 to 564 mM. One negative excursion in Cl is at 325.5 m CSF, where Cl drops from 548 to 499 mM (~11% less than modern seawater value). This excursion is likely due to dissociation of gas hydrates within this interval during drilling and core retrieval operations. Furthermore, the slightly reduced Cl in Hole C0007D (~1%–3% less than modern seawater value) likely reflects disseminated gas hydrate within the sediment pore space that dissociated upon core recovery. Local Cl values slightly above seawater value may indicate horizons of localized formation of hydrous silicates during ash alteration. At the base of Hole C0007D, from 431.6 to 437.0 m CSF, Cl increases slightly to 557 mM, close to modern seawater value (559 mM).

In general, sodium is higher than modern seawater value at Site C0007 (Fig. **F40C**). Initially, Na rapidly increases from 486 mM at 1.5 m CSF to 501 mM at 55.3 m CSF with local minima. Sodium then remains relatively constant to the base of Hole C0007D. Superimposed on the elevated but relatively constant Na is a sharp minimum at 325.5 m CSF coincident with minima in pore fluid salinity and Cl and Br, also reflecting a localized occurrence of gas hydrate. Besides this inferred gas hydrate–bearing interval, Na is decoupled from Cl with localized minima and maxima (Fig. **F40D, F40H**), indicating that the elevated Na is not the result of water consumption during the formation of authigenic silicates but rather indicating that the elevated Na may be the result of continued ion exchange with ammonium, dissolution of volcanic ash, and/or feldspar weathering.

Pore fluid constituents controlled by microbially mediated reactions

Sulfate and alkalinity

An interesting and thought-provoking outcome of the geochemical program at Site C0007 is that the SMT was not recovered (Fig. **F41B, F41F**). The SMT at Sites C0004 and C0006 was reached at relatively shallow depths (<20 m CSF). At Site C0007, however, sulfate reduction is relatively rapid in the upper ~20 m but sulfate never reaches depletion in Hole C0007C (Fig. **F41B**) and headspace CH_4 concentration remains low (see **"Organic geochemistry"**). Sulfate decreases monotonically from 26.73 mM at 1.5 m CSF to 10.57 mM at 17.0 m CSF and then decreases gradually to 8.11 mM at 33.0 m CSF. Below this depth, SO_4 gradually increases to 13.71 mM at 129.9 m CSF and then increases sharply to 28.07 mM at the base of Hole C0007C (149.1 m CSF).

At the top of Hole C0007D, dissolved SO_4 is almost depleted (1.55 mM at 191.6 m CSF). This depletion constitutes a 95% decrease in sulfate over an interval of only 20 m from the base of Hole C0007C to the top of Hole C0007D. This is not entirely surprising, as the two holes are separated by ~185 m. Sulfate is relatively low throughout Hole C0007D, ranging from 0 to 8 mM. The slightly elevated sulfate likely indicates varying degrees of drill water contamination. This inference is corroborated by elevated methane between ~180 and 300 m CSF (see **"Organic geochemistry"**). However, because we did not recover the SMT at this site, it is difficult to discern between elevated SO_4 caused by drilling contamination and that reflecting in situ pore fluid concentrations. Thus, to be conservative we did not correct the elemental concentrations for drilling contamination based on sulfate concentration at this site, but it can be assumed that the dissolved SO_4 is low to negligible in Hole C0007D.

The alkalinity profile in Hole C0007C is a mirror image of the sulfate profile (Fig. **F41C**). Pore fluid alkalinity increases monotonically from 4.5 mM at 1.5 m CSF to 16.20 mM at 17.0 m CSF. Alkalinity then increases more gradually to a maximum of 18.34 mM at 33.0 m CSF. Below this depth, alkalinity decreases to 11.81 mM at 129.9 m CSF and then decreases sharply to 4.40 mM at 149.1 m CSF, which is near modern seawater value (2.325 mM). In Hole C0007D, alkalinity jumps to 15.35 mM at 191.6 m CSF, which is ~3.5 times the alkalinity measured at the base of Hole C0007C. Alkalinity steadily decreases from 191.6 m CSF to 6.47 mM at 431.6 m CSF.

Ammonium, phosphate, and bromide

Ammonium increases rapidly with depth in lithologic Unit I and reaches a maximum at 55.3 m CSF. From 55.3 to 129.9 m CSF, NH_4 remains relatively constant and then decreases sharply to 1289 µM at 149.1 m CSF (Fig. **F42A**). Ammonium increases abruptly between the base of Hole C0007C and the top of Hole C0007D, where NH_4 is 3867 µM at 191.6 m CSF (Fig. **F42D**). Below this depth, ammonium gradually decreases with depth, reaching 1403 µM at the base of Hole C0007D (437.0 m CSF). The initial rapid increase in ammonium is the result of microbially mediated decomposition of organic matter. The decline with depth in Hole C0007D likely reflects decreasing metabolic rates and thus declining ammonium production, as well as sorption on clay minerals.

Phosphate increases sharply in the upper part of the sediment section and peaks at a shallower depth than ammonium, reaching a maximum of 78 µM at 31.6 m CSF (Fig. **F42B**). Below this depth, phosphate decreases until 149.0 m CSF. From the base of Hole C0007C to Hole C0007D, phosphate increases to 24 µM at 191.6 m CSF. Below this depth, PO_4 varies slightly and remains close to the detection limit. The phosphate increase in the upper 30 m reflects active organic matter decomposition in the zone of most active sulfate reduction. Below this depth, dissolved PO_4 is controlled by the solubility of apatite, which is a major sink for phosphate.

Bromide in marine interstitial waters is sensitive to organic matter diagenesis, with concentration higher than seawater reflecting marine organic matter decomposition. Br initially increases from 0.83 mM at 1.5 m CSF to 0.88 mM at 55.3 m CSF. Below this depth, Br remains relatively constant to 129.7 m CSF and then drops sharply to 0.83 mM at 149.1 m CSF. Br increases abruptly from 0.83 mM at the base of Hole C0007C to 0.90 mM at the top of Hole C0007D. Below this depth, the Br profile varies with a maximum of 0.96 mM at 257.3 m CSF and a minimum of 0.82 mM occurring at 325.5 m CSF. This minimum is coincident with minima in Cl and Na and reflects gas hydrate dissociation during core recovery. Br in Hole C0007D is lower than the equivalent depths at Sites C0004 and C0006, suggesting that organic matter degradation is less intense at this site.

Major cations (Ca, Mg, and K)

Calcium decreases rapidly from 9.90 mM at 1.5 m CSF to a minimum of 4.77 mM at 31.6 m CSF (Fig. **F43A**), reflecting Ca consumption during authigenic carbonate formation in the zone of most intense sulfate reduction (Fig. **F41B**). Below this depth, Ca gradually increases to 6.41 mM at 129.9 m CSF and then increases rapidly toward modern seawater value at 149.1 m CSF. Calcium decreases abruptly from near-

seawater value at the base of Hole C0007C to 5.48 mM at 191.6 m CSF in Hole C0007D. Below this depth, Ca increases gradually to the base of Unit II (Fig. **F43E**) and then increases in Unit III to a maximum of 13.57 mM at 402.1 m CSF. This zone of Ca increase is coincident with a fault zone extending from ~400 to 420 m CSF (see **"Structural geology"**). Below this depth, Ca decreases to 8.61 mM at 437.0 m CSF. The relatively sharp increase in Ca suggests that the fluid sampled in the fault zone is unique from the fluids above and below.

The magnesium profile in Hole C0007C is very similar to the Ca profile (Fig. **F43A, F43B**). Mg decreases gradually from 48.1 mM at 1.5 m CSF to 37.0 mM at 31.6 m CSF, reflecting the incorporation of Mg in authigenic carbonates precipitating in the zone of sulfate reduction and alkalinity production and Mg uptake during the alteration of volcanic ash. Below 31.6 m CSF, Mg remains constant to ~100 m CSF and then increases to near-seawater value (45.48 mM) at 149.1 m CSF. Mg drops abruptly from 45.48 mM at the base of Hole C0007C to 27.18 mM at 191.6 m CSF in Hole C0007D. Below this depth, Mg gradually decreases and varies to 417.9 m CSF, likely reflecting Mg uptake in authigenic clay minerals formed during the alteration of volcanic ash with depth. Below 417.9 m CSF, Mg increases slightly to higher values.

Dissolved potassium is above modern seawater value between 1.5 and 17.0 m CSF, reflecting either ion exchange with NH_4 in the interval of most intense organic matter degradation and ammonium production or a sampling artifact caused by pressure changes during core recovery (Figs. **F43C, F42A**). Below 17.0 m CSF, K is slightly lower than seawater value with several local minima. Potassium decreases sharply from the base of Hole C0007C to 8.5 mM at 191.6 m CSF in Hole C0007D. Below this depth, K gradually decreases to 6.7 mM at 408.2 m CSF. This gradual decline in K likely reflects the uptake of dissolved potassium in authigenic zeolites forming during the alteration of volcanic ash and feldspar in Units II and III.

Minor elements (B, Li, H_4SiO_4, Sr, Ba, Mn, and Fe)

Boron is slightly elevated with respect to modern seawater from 1.5 to 10.0 m CSF and then decreases sharply to 265 µM at 86.6 m CSF. At this depth, B increases to 407 µM at 149.1 m CSF. B is very low in Hole C0007D, ranging from 146 to 292 µM. The overall low boron at Site C0007 is likely controlled by low-temperature alteration of volcanic ash and the subsequent formation of authigenic clay minerals, as well as by B uptake by adsorption on clay minerals. It is interesting to note that B increases abruptly at 417.9 m CSF to 292 µM at total depth (TD), which is directly below a fault zone; this increase is coincident with changes in the other major and minor elements analyzed at this site.

Dissolved Li decreases sharply from seawater value at 1.5 m CSF to 7.9 µM at 14.2 m CSF. Below this depth, Li gradually increases to seawater value toward the base of Hole C0007C, reaching 23.0 µM at 149.1 m CSF. Unlike the Ca, Mg, K, and B profiles, Li does not change much between the base of Hole C0007C and the top of Hole C0007D (Fig. **F44A, F44D**). Lithium remains relatively constant from 191.0 to 314.0 m CSF, ranging from 15.3 to 25.4 µM. At 314.0 m CSF, Li increases steadily to 107.0 µM at 417.0 m CSF, which is coincident with chemical anomalies in other pore fluid constituents, as well as a prominent fault zone extending from 400.0 to 420.0 m CSF (see **"Structural geology"**). From 417.0 to 437.0 m CSF, the Li profile reverses, and Li reaches concentration observed above the fault zone at ~380 m CSF.

Dissolved silica is higher than modern seawater throughout Holes C0007C and C0007D, and values are scattered with local minima at 17, 149, 249, 305 and 352 m CSF and local maxima at 32, 92, 222, 333 and 408 m CSF.

Dissolved Sr decreases from 79 µM at 1.5 m CSF to 57 µM at 55.3 m CSF, which is consistent with the incorporation of Sr in authigenic carbonates formed in the zone of most intense sulfate reduction and alkalinity production. Below 55.3 m CSF, Sr increases sharply to a near-seawater value of 83 µM at 129.9 m CSF and remains constant to the base of Hole C0007C. This quick return to near-seawater value suggests a source of Sr below the zone of authigenic carbonate precipitation. Sr decreases sharply from 83 µM at the base of Hole C0007C to 74 µM at 191.6 m CSF in Hole C0007D and then increases linearly to 104 µM at 257.3 m CSF. Below this depth, Sr remains fairly constant to the base of the hole with a minimum of 97 µM at 325.5 m CSF and a maximum of 119 µM at 351.7 m CSF. The Sr minimum at 325.5 m CSF is coincident with sharp decreases in Cl, Na, and Br and is the result of gas hydrate dissociation during core recovery. Calcite in the sediment column at Site C0007 is low, in general less than ~8 wt% (see **"Lithology"** and **"Organic geochemistry"**); thus, variations in Sr below ~30 m CSF are not controlled by carbonate diagenesis. Variations in the Sr profile are likely the result of volcanic ash alteration.

Dissolved Ba is depleted in the upper ~10 m of Unit I. Ba then increases to 1.3 µM at 17.0 m CSF, below which Ba remains relatively constant to the base of Hole C0007C. One of the primary solid phases hosting Ba in marine sediments is the mineral barite ($BaSO_4$). Barite is stable under oxic conditions but be-

comes undersaturated and dissolves when pore fluid sulfate is depleted, releasing dissolved Ba to the pore fluids. The low Ba in Hole C0007C is the manifestation of the elevated sulfate, and thus the fluids are supersaturated with respect to barite. The slight Ba mobilization within Hole C0007C is likely the result of the dissolution of Fe and Mn oxyhydroxides during organic matter diagenesis. Ba increases sharply from the base of Hole C0007C to 11.9 µM at 191.6 m CSF in Hole C0007D, where SO_4 is depleted. Ba remains fairly constant to 325.5 m CSF (Fig. **F41H**) and then increases sharply at the Unit II/III boundary. Ba decreases sharply from 141.5 µM at 383.2 m CSF to 23.5 µM at 408.0 m CSF and then increases to values similar to those observed at the top of Unit III at the bottom of the geochemical profile at 437.0 m CSF. The minimum in dissolved Ba between 400 and 410 m CSF is coincident with increases in Ca and Li as well as a fault zone. The overall elevated Ba in Hole C0007D is consistent with sulfate depletion and the dissolution of barite with depth. Localized elevated Ba to values as high as ~140 µM occur at a change in lithology in the bottom of Unit II and in Unit III from more sand-dominated sediments above to more mud-rich sediments below (see **"Lithology"**). This interval is interpreted to represent a hemipelagic setting with thin turbidite sequences; biogenic phases, such as marine barite, would therefore be less diluted by terrigenous material. Thus, barite was likely higher at these depths, and the elevated Ba simply reflects the dissolution of barite because of sulfate depletion within this interval.

Dissolved Mn decreases sharply from 12.21 µM at 1.5 m CSF to 1.38 µM at 5.8 m CSF. The elevated Mn in the upper ~6 m at this site reflects MnO_2 reduction within a depth interval where MnO_2 is a favorable and important electron acceptor for microbially mediated organic matter decomposition. Below this depth, Mn is relatively constant to the base of Hole C0007C, ranging from 1.75 to 5.1 µM. Mn is scattered and variable in Hole C0007D, ranging from 1.4 to 7.3 µM. In Unit III, Mn displays considerable mobility and reaches a maximum of 17.2 µM at 402.1 m CSF, coinciding with the occurrence of a fault zone extending from 400 to 420 m CSF. Below this depth, the Mn profile reverses, approaching the same values as those above the fault zone. Dissolved Fe is more variable in Hole C0007C than in Hole C0007D. Fe is slightly elevated with respect to modern seawater value in the upper 6 m, reflecting Fe oxyhydroxide reduction during microbially mediated decomposition of organic matter. Below this depth, Fe varies from 0.55 to 16.84 µM. Dissolved Fe is elevated at the top of Hole C0007D, 4.28 µM at 191.6 m CSF, and then decreases and remains constant at ~1 µM to TD.

Trace elements (Rb, Cs, V, Cu, Zn, Mo, Pb, U, and Y)

Rb concentration decreases with depth in Hole C0007C from 1.52 µM at 1.5 m CSF to 1.10 µM at 149.0 m CSF (Fig. **F43B**). Rb decreases between Hole C0007C and Hole C0007D to 0.92 µM. In general, Rb decreases with depth in Hole C0007D, reaching a minimum of 0.53 µM (~62% less than seawater value) at 417.9 m CSF. Cs increases from 2.9 nM at 1.5 m CSF to 7.3 nM at 102.9 m CSF (Fig. **F43B**). Cs then decreases to 4.1 nM at the base of Hole C0007C. Cs generally decreases in Hole C0007D, reaching a minimum of 1.9 nM between ~402 and 418 m CSF, coincident with maxima and minima in the major and minor elements, as well as a fault/fracture zone. Below this depth to the base of the hole, there is a minor increase in Cs concentration.

Molybdenum is variable and generally above seawater value in Hole C0007C, ranging from 68 to 418 nM (Fig. **F45A**). Mo decreases sharply from the base of Hole C0007C to the top of Hole C0007D from 418 µM at 149.1 m CSF to 57 µM at 191.8 m CSF. Mo then increases to 444 µM at 314.2 m CSF. Below this depth, Mo is variable with concentration minima at 351.9 and 402.1 m CSF and maxima at 393.0 and 437.0 m CSF.

Copper decreases with depth in Hole C0007C from 8600 nM at 1.5 m CSF to 534 nM at 149.2 m CSF with a peak of 12,122 nM at 92.1 m CSF. Copper is more variable in Hole C0007D, ranging from 1947 to 32,983 nM. The zinc concentration profile is very similar to the copper profile, except that concentration does not decrease in Hole C0007C. Vanadium concentration decreases in Hole C0007C from 122.2 nM at 5.8 m CSF to 14.6 nM at 149.1 m CSF. V concentration increases to 27.9 nM at 304.5 m CSF, below which V decreases to 8.8 nM at TD.

Uranium decreases from 6.4 nM at 1.5 m CSF to 0.6 nM at 9.9 m CSF (Fig. **F45B**). Uranium is much more soluble under oxidizing conditions than reducing conditions; thus, the rapid decline in U is the manifestation of the rapid depletion of oxygen and other complexes in the upper part of the sediment section. From 9.9 to 129.9 m CSF, U remains relatively constant and then increases to near-seawater values at 149.1 m CSF. In Hole C0007D, U increases from 1.4 to 5.4 nM at 325.5 m CSF. Below this depth, U is variable, ranging from 2.7 to 4.6 nM. Lead is variable in Hole C0007C, ranging from 0.3 to 2.1 nM. Pb is relatively constant in Unit II in Hole C0007D with an average concentration of ~1.5 nM. Pb is variable in Unit III with a prominent peak of 52.6 nM at 431.6 m CSF. Yttrium decreases with depth in Hole C0007C from 1.4 pM at 1.5 m CSF to

0.63 pM at 149.1 m CSF. Y increases from the base of Hole C0007C to the top of Hole C0007D to 2.0 pM. Y concentration then decreases with depth, reaching 0.46 pM at TD.

$\delta^{18}O$

$\delta^{18}O$ is variable but near-seawater value (0‰) in Hole C0007C with a minimum value of –1.78‰ and a maximum of 0.11‰ occurring near the seafloor at 1.5 m CSF. $\delta^{18}O$ decreases abruptly between Hole C0007C and Hole C0007D to –1.63 ‰. $\delta^{18}O$ continues to decrease to a minimum of –3.70‰ at 351.7 m CSF and then progressively increases to –1.16‰ at 437.0 m CSF.

Organic geochemistry

Hydrocarbon gas composition

Headspace gas composition was rapidly analyzed for safety monitoring (Table **T15**) and by using a more time consuming extraction procedure for scientific interpretation (Table **T16;** Fig. **F47**). Methane was detected in all samples at Site C0007. Concentration peaks at ~5.3 mM at ~230 m CSF. Below this peak, methane decreases with depth. Throughout Hole C0007C methane concentration is very low (<60 µM) and sulfate concentration is high (see **"Inorganic geochemistry"**). At the bottom of Hole C0007C, methane concentration is still very low, whereas at the top of Hole C0007D, concentration increases sharply. Based on these data, the SMT zone is likely above 190 m CSF in Hole C0007D and below 150 m CSF in Hole C0007C, although it was not cored. However, the depth of the assumed SMT at Site C0007 would differ strongly from the depths observed at Sites C0004 and C0006 (16–20 and 8–12 m CSF, respectively).

Ethane was the only other light hydrocarbon detected and was only measured at ~94 m CSF in Holes C0007C and C0007D. The methane/ethane (C_1/C_2) ratio is constantly high, indicating biogenic origin of the hydrocarbon gases.

Sediment carbon, nitrogen, and sulfur composition

Calcium carbonate ($CaCO_3$) content calculated from inorganic carbon concentration is generally very low and ranges from 6.99 to 0.21 wt% (Table **T17;** Fig. **F48**). In Hole C0007D, $CaCO_3$ concentration is higher below 300 m CSF.

Total organic carbon (TOC) content remains low throughout the sediment column (average = 0.39 wt%). The highest TOC content (~0.7 wt%) was measured at 82 m CSF. Similar to TOC concentration, total nitrogen (TN) content is rather low in the sediments (average = ~0.055 wt%). TN concentration slightly increases at the top of lithologic Unit II in Hole C0007C. In Hole C0007D, the TN concentration profile generally correlates with the profile of total clay minerals (see **"Lithology"**). This trend is also reflected in the ratio of TOC and TN (C/N), which has a mean value of ~7, indicating that the organic matter in the sediments from Site C0007 is mainly of marine origin.

The highest concentration of total sulfur (TS) was measured in Unit I, where it reaches a maximum of 1.14 wt%. This indicates the precipitation of authigenic iron sulfides related to the remineralization of organic matter by microbial sulfate reduction (see **"Inorganic geochemistry"**). At the top of Hole C0007D, an enrichment of TS indicates the presence of iron sulfides. These iron sulfides could be related to the alteration of iron oxides and oxyhydroxides by hydrogen sulfide, which was produced by AOM near the SMT. This relationship will be further investigated on shore. The highest amounts of TS are in Unit III. These enrichments of TS are related to the occurrence of pyrite nodules and pyrite filled burrows (see Fig. **F12**).

Microbiology and biogeochemistry

Sample processing

To study microbiological and biogeochemical characteristics in sediments at Site C0007, samples were obtained from 120 different depth locations (Table **T18**). For high-resolution enumeration of cell abundance, 3 cm^3 of sediment was collected from core section ends on deck. All whole-round core sample processing was carried out after X-ray CT scanning and was completed within 1 h after core recovery on deck.

Cell abundance

Cell abundance in sediments at Site C0007 was enumerated by microscopic direct count of SYBR Green I–stained cells. The vertical profile of cell abundances showed that 10^8 cells/cm^3 was consistently observed in core sediments to 484 m CSF (Fig. **F49**). Most observed cells were small coccoids, and some short rods were also observed as minor components. The fluorescent intensity of SYBR Green I–stained cells in upper sediment layers (0–159 m CSF) was observed to be brighter than those in other layers. At 102.7 m CSF (Section 316-C0007C-11X-2), a significant decrease of cell abundance was observed (6.57×10^7

cells/cm^3; see Fig. F49). Despite the cell abundance decrease at this horizon, the observed coccoid cells were relatively large with bright fluorescent signals. Large coccoids were also observed in the gravel layer (Section 316-C0007D-17H-1; see Fig. F50). Cell abundance in the gravel layer was estimated to be 7.45×10^8 cells/cm^3, which was the most abundant microbial population in samples from Site C0007. These upper sedimentary layers consist of permeable sands and silt, in which nutrient flux (e.g., organic matter and sulfate) via fluid circulation may support microbial activity (see "Inorganic geochemistry"). In sediments below 200 m CSF, some small proliferations of microbial population were observed at thrust fault-associated layers. For example, 5.83×10^8 cells/cm^3 were present in fault zone materials at 417.9 m CSF (Section 316-C0007D-27X-1) (Fig. F49). Similar to the sand and gravel layers described above, the cell abundance proliferations suggested that the flux of nutrient energy that supports the population of microbial community is high at the fault zone. The average cell abundance enumerated by onboard microscopic direct count of SYBR Green I–stained cells was $3.67 \times 10^8 \pm 1.86 \times 10^8$ cells/cm^3 (N = 27).

Physical properties

At Site C0007, physical property measurements were made to provide basic information characterizing lithologic units, states of consolidation, deformation, and strain and to correlate coring results with downhole logging data. After capturing X-ray CT images and the core reached thermal equilibrium with ambient temperature at ~20°C, gamma ray attenuation (GRA) density, magnetic susceptibility, natural gamma radiation, *P*-wave velocity, and noncontact electrical resistivity were measured using a multisensor core logger (MSCL) system on whole-round core sections (MSCL-W). Thermal conductivity was measured using either a full-space needle probe method or a half-space line source method on split working halves. The half-space method was used on lithified sediments deeper in the hole that were impenetrable with the needle probe. Cores were split in two longitudinally, one half for archiving and one half for sampling and analysis. A photo image capture logger (MSCL-I) and a color spectrophotometer (MSCL-C) were used to collect images of the split surfaces of the archive halves. Moisture and density (MAD) were measured on discrete subsamples collected from the working halves as well as from "clusters" adjacent to whole-round samples removed before splitting. Vane shear and penetration experiments were performed on the working halves to 150 m CSF. Additional discrete subsamples from working halves were used to perform electrical conductivity measurements, *P*-wave velocity measurements, and anisotropy calculations.

Density and porosity

Bulk density values at Site C0007 were determined from both GRA measurements on whole cores and MAD measurements on discrete samples from the working halves of split cores (see "Physical properties" in the "Expedition 316 methods" chapter). A total of 225 discrete samples were analyzed for MAD (100 from Holes C0007A, C0007B, and C0007C and 125 from Hole C0007D).

Holes C0007A, C0007B, and C0007C

MAD wet bulk density increases markedly to ~20 m CSF from ~1.55 to ~1.90 g/cm^3, followed by a much more gradual increase with depth to ~150 m CSF (Fig. F51A). The maximum MSCL bulk density values also show similar trends. GRA bulk density is in very good agreement with MAD bulk density for depths less than ~100 m CSF. At depths >100 m CSF, GRA density is generally smaller than MAD bulk density and reveals a larger degree of scatter compared to MAD density. The scatter in MAD bulk density is likely due to lithologic variations among the interbedded sand, silt, and mud at this site. Grain density was also determined via MAD measurements on discrete samples. Grain density decreases slightly from ~2.7 to ~2.68 g/cm^3 from 0 to ~34 m CSF (Fig. F51B). Between ~34 and ~110 m CSF, grain density is approximately constant with depth (average = ~2.7 g/cm^3).

Porosity was estimated from whole-round core MSCL scan data and calculated from MAD measurements on discrete samples. These porosity values (see "Physical properties" in the "Expedition 316 methods" chapter) generally decrease with depth (Fig. F51C) and vary inversely with MAD bulk density.

Hole C0007D

MAD wet bulk density increases slightly with depth (~1.93 to 2.07) from ~175 to ~320 m CSF (Fig. F51D). Bulk density decreases from ~2.07 g/cm^3 at ~320 m CSF to ~1.87 g/cm^3 at ~400 m CSF. Maximum MSCL bulk density values at various depths within this range are similar to the MAD bulk density versus depth trend. The scatter in MAD bulk density is likely due to lithologic variations at this site. Grain density values were approximately constant with depth (average = ~2.7 g/cm^3) (Fig. F51E).

MAD porosity decreases slightly (from ~42% to ~39%) from ~175 to ~320 m CSF (Fig. F51F) and var-

ies inversely with bulk density (from which porosity data are derived) over that range. At ~320 m CSF, porosity increases with depth (from ~39% to ~50%) from ~320 to ~400 m CSF (Fig. F51F).

Because of the greater scatter in MSCL density and porosity, we focus our description on bulk density and porosity calculated from discrete MAD measurements.

Density and porosity of lithologic units

At Site C0007, a Pleistocene package of muds with interbedded sand and volcanic ash comprises Unit I (see "Lithology"). Bulk density increases markedly with depth in the uppermost 20 m at this site from ~1.55 to ~1.90 g/cm³ (Fig. F51A). Porosity varies inversely with density over this depth range (Fig. F51C).

Unit II is composed of Pleistocene interbedded sand and mud (see "Lithology"). Within Unit II from ~34 m CSF in Hole C0007C to ~320 m CSF in Hole C0007D, bulk density gradually increases from ~1.90 to ~2.07 g/cm³ (Fig. F51A, F51D). This trend is mirrored by a slight decrease in porosity with depth from ~48% at 34 m CSF to ~39% near the bottom of Subunit IIC in Hole C0007D (Fig. F51C, F51F).

In the bottom two-thirds of Unit II (from ~320 to ~400 m CSF), bulk density decreases markedly from ~2.07 to 1.87 g/cm³ (Fig. F51D), whereas porosity increases from ~39% to ~50% (Fig. F51F). At ~400 m CSF, however, bulk density and porosity resume normal trends, increasing and decreasing, respectively, with increasing depth (Fig. F51D, F51F).

Relationships of density and porosity changes to lithologic unit and structural boundaries

In addition to the unit boundaries described above, the structural geology group identified the following zones of concentrated shear deformation as fault zones (see "Structural geology"):

Fault Zone 1 = ~238 to ~259 m CSF,
Fault Zone 2 = ~342 to ~362 m CSF, and
Fault Zone 3 = ~399 to ~446 m CSF.

As indicated above, MAD-derived bulk density and porosity values increase and decrease, respectively, from 0 to ~320 m CSF and reveal no clear discontinuities at depths corresponding to possible faults or at the Unit I/II and Unit II/III lithologic boundaries within that depth range. A discontinuity in the porosity versus depth trend at ~320 m CSF occurs within Unit II.

The zone of highest porosity (~50%) between ~360 and ~400 m CSF may be bounded by fault Zones 2 and 3 (Fig. F51F). This zone of elevated porosity likely results from higher density of fluid-filled microcracks and other fault-related damage. Alternatively, elevated porosity in this zone could indicate that these sediments are underconsolidated because of elevated fluid pressures, which may have localized shear deformation in this region. We note that although mud and silt samples from these zones of elevated porosity appear to be well-indurated chunks of material, they are actually quite friable in hand samples. This observation suggests that these are possible zones of fault-related damage. We also note that the interval of elevated porosity appears to correlate with the lithologic transition from lowermost Unit II to Unit III. Finally, we note that lithologic analyses reveal that Unit III exhibits an overall increase in clay content and decrease in plagioclase content compared to the lowermost portion of Unit II (see "Lithology"). Clays may lead to spuriously high porosity values, if the drying process during MAD analyses removes interlayer water from smectite. Clays may also decrease permeability of the sediments and rocks in this interval, allowing elevated pore fluid pressures to develop more readily.

P-wave velocity and electrical conductivity in discrete samples

At Site C0007, *P*-wave velocity and electrical conductivity were acquired from discrete samples from ~300 to 450 m CSF. This limited depth range encompasses the Unit II/III boundary, and data show interesting trends that seem to correlate fairly well with findings at nearby Site C0006.

Figure F52 shows the variations of *P*-wave velocity, electrical conductivity, and their respective in-plane and transverse anisotropies (see "Physical properties" in the "Expedition 316 methods" chapter). *P*-wave velocity varies between 1800 and 2000 m/s and increases slightly with depth but then decreases between 360 and ~440 m CSF (Fig. F52A). The trend changes sign at the Unit II/III boundary. The scarcity of data makes interpretation difficult. It is possible that the apparent decrease below 360 m CSF is the combination of a *P*-wave velocity offset (approximately –100 m/s) at the Unit II/III boundary and a velocity reduction associated with thrust faults observed at ~430–440 m CSF. The Unit II/III boundary is associated with a higher transverse velocity anisotropy (Fig. F52B), which could be indicative of horizontal compaction or vertical stress relief, causing hardening parallel to σ_1 or microcracking along the bedding plane.

Electrical conductivity (Fig. F52C) trends are inversely correlated to those observed in *P*-wave velocity. Electrical conductivity increases slightly to the Unit II/III boundary and then decreases. As with *P*-wave velocity, the lack of electrical conductivity data

hinders interpretation. However, comparisons with data from nearby Site C0006 indicate that the results obtained in the trench-basin transition are consistent and make inferences possible. These comparisons suggest that electrical conductivity may be decreasing to ~330 m CSF and that there may be an offset at the Unit II/III boundary (see **"Lithology"**) followed by a more normal conductivity decrease trend with depth in Unit III. The progressive offset takes place. Transverse anisotropy (Fig. **F52D**) is significantly reduced at the Unit II/III boundary, possibly indicating horizontal compaction. This interpretation suggests that Site C0007 results between ~330 and ~370 m CSF represent intervals that were not recovered at Site C0006.

The offset observed in the electrical conductivity signal fits very well with trends observed in MAD porosity values. Below the Unit II/III boundary, higher electrical conductivity and lower *P*-wave velocity are consistent with the higher porosity discussed above.

Thermal conductivity

Thermal conductivity measurements were conducted on whole-round HPCS and ESCS cores (<316 m CSF) and on split core samples from RCB cores at depths >340 m CSF. Thermal conductivity ranges from 0.94 to 1.58 W/(m·K) (Table **T19;** Fig. **F53A**). Thermal conductivity from the seafloor to ~50 m CSF increases rapidly, likely reflecting the decrease in porosity with depth and relatively high sand content. A negative trend in thermal conductivity between ~50 and 75 m CSF likely reflects a decrease in sand content. Between ~190 and 410 m CSF, thermal conductivity values fall in a restricted range between 1.21 and 1.32 W/(m·K).

In situ temperature

In situ temperature was measured using both the advanced piston coring temperature tool (APCT3) and sediment temperature (SET) tool. All measurements were made in calm to moderate seas and were successful (Table **T20**). Temperature-time series for each temperature measurement are shown in Figure **F54.** The temperature tool was stopped at the mudline for as long as 10 min prior to each penetration. The average apparent bottom water temperature is 1.65°C (Table **T20**). Significant frictional heating occurred on all penetrations, and the temperature versus time records exhibit the characteristic probe penetration heating pulse and subsequent decay (Fig. **F54**). Equilibrium temperature estimates are based on a 1/time approximation from the temperature-time series while the tool is at the bottom. The effective origin time of the thermal pulse associated with tool penetration was estimated by varying the assumed origin time until the thermal pulse decay followed the theoretical curve. A delay of 4–81 s from the initial penetration heating time was required to give a linear 1/time plot. The temperature measurement at 52.6 m CSF shows multiple temperature spikes consistent with tool movement while in the formation (Fig. **F54D**). As a result, the equilibrium temperature is based on a shorter time series than the other measurements. However, in spite of the short period over which this equilibrium temperature is estimated, it falls close to the thermal gradient defined with the other temperature-depth measurements, giving confidence in this temperature determination (Fig. **F53C**). Additionally, it is important to note that temperatures derived from the APCT3 and SET tools give consistent results. Equilibrium temperatures as a function of depth are quite linear. The best-fit thermal gradient through the first six measurements is 42°C/km (Fig. **F53C**).

Heat flow

If heat transfer is by conduction and heat flow is constant, the thermal gradient will be inversely proportional to thermal conductivity according to Fourier's law. This relationship can be linearized by plotting temperature as a function of summed thermal resistance (Bullard, 1939) (see the **"Expedition 316 methods"** chapter) (Fig. **F53D**). The least-squares fit to the temperature and thermal resistance data indicates a heat flow of 53 mW/m^2 and a bottom water temperature of 2.0°C. The estimated bottom water temperature is 0.4°C different than the measured apparent bottom water temperature (Table **T19**). Predicted temperature deviates from those measured by <0.2°C. A constant conductive heat flow appears to describe the overall thermal structure quite well. The computed heat flow is anomalously low with respect to other heat flow values in the Kii region (Yamano et al., 2003) but higher than estimated for Site C0006.

Shear strength

Shear strength measurements were conducted using a semiautomated miniature vane shear device and a pocket penetrometer. Measurements were made at discrete locations on the working halves of split cores at a frequency of approximately three measurements per core (generally in sections 2, 5, and 7). Tests were conducted on relatively intact and homogeneous parts of these sections, generally between 50 and 100 cm below the top of the section. To minimize error induced by disturbance of the core by the measurement technique, vane shear tests were conducted first, followed by penetrometer tests 1–2 cm from the site of the vane shear penetration. No vane

shear measurements were conducted on whole cores. Both instruments were inserted orthogonally to the surface of the working halves. The rotation rate of the semiautomated vane shear apparatus on board the *Chikyu* is 71°/min.

Three distinct intervals of increasing shear strength with depth were observed (Fig. F55). The intervals are offset from each other by decreases in shear strength. The first interval extends from the seafloor to ~35 m CSF (the Unit I/II boundary). Shear strength through this interval increases at a much faster rate than at similar depths at Sites C0004 and C0006. At 35 m CSF, shear strength drops by a factor of 2 and increases to 55 m CSF, at which point it decreases to the lower limit of our ability to measure it. Shear strength then increases to 91 m CSF. At depths below this point, the consolidation state of the cores makes further interpretation difficult. As with Site C0006, low shear strength values for lower depths do not necessarily represent in situ shear strength at these depths. Both vane shear and penetrometer measurements are designed for use in clay and thus may underestimate the shear strength of sand.

Color spectrometry

Results from the measurement of color reflectance are presented in Figure F56. The L* values range from ~20 to 50. The a* values range from –2 to 2 and the b* values range from 0 to 4. There are no significant anomalies.

Magnetic susceptibility

Volumetric magnetic susceptibilities were measured using whole-round core MSCL in all recovered cores from Site C0007 (Fig. F57). Uncorrected magnetic susceptibility values are presented in this chapter. Magnetic susceptibility varies between ~0 and 600 × 10^{-3} SI with a mean of ~137 × 10^{-3} SI. Magnetic susceptibility values in Unit I generally increase with depth. Within Unit II, values reach a maximum and then generally decrease with depth. Values within Unit III are low, possibly reflecting lithologic variation.

Natural gamma ray

Natural gamma ray (NGR) results are reported in counts per second (cps). The background scatter, produced by Compton scattering, photoelectric absorption, and pair production was measured at the beginning and subtracted from measured gamma ray values. In general, NGR counts are low and consequently may be affected by the short counting interval and porosity variations. The average and standard deviation of NGR results are 34 and 8 cps, respectively (Fig. F58). NGR values generally decrease from the seafloor to ~150 m CSF. Between ~150 m CSF and TD, NGR values remain relatively constant.

Integration with seismic data

There are no logging-while-drilling (LWD) data at this site, and core-seismic integration between these holes is primarily based on prestack depth-migrated seismic profiles. The distance between Holes C0007A, C0007B, C0007C, and C0007D is 185 m (Fig. F1), and these holes are ~700 m from Holes C0006E and C0006F. Seismic profile Inline 2437 from the CDEX 3-D seismic survey (Fig. F2) passes through Hole C0007D and is ~10 m from Holes C0007A, C0007B, and C0007C. Holes C0006E and C0006F are 50–60 m from this seismic profile and are projected onto it.

The accuracy of core-seismic integration is degraded by both the lack of LWD data in general and low to poor core recovery in some sections of the holes. Nevertheless, NGR and MSCL-W data from core logs are superimposed over the seismic data (Fig. F59) and some key reflections match well with core data, likely imaging key sedimentary facies and faults. The Unit II/III boundary at 362 m CSF corresponds to a high-amplitude reflection with no depth shift. Preliminary interpretations suggest the Unit III/IV boundary at 475 m CSF may tie to the reflector at 450 m CSF, indicating a depth difference of 25 m. Furthermore, the lithology of Core 316-C0007D-25R is sand, consistent with seismic interpretations. However, poor core recovery of this section makes seismic-core integration difficult.

References

Ashi, J., Kuramoto, S., Morita, S., Tsunogai, U., Goto, S., Kojima, S., Okamoto, T., Ishimura, T., Ijiri, A., Toki, T., Kudo, S., Asai, S., and Utsumi, M., 2002. Structure and cold seep of the Nankai accretionary prism off Kumano—outline of the off Kumano survey during YK01-04 Leg 2 cruise. *JAMSTEC J. Deep Sea Res.,* 20:1–8. (in Japanese, with abstract in English)

Bullard, E.C., 1939. Heat flow in South Africa. *Proc. R. Soc. London, Ser. A,* 173:474–502.

Chester, F.M., and Logan, J.M., 1987. Composite planar fabric of gouge from the Punchbowl Fault, California. *J. Struct. Geol.,* 9(5–6):621–634. **doi:10.1016/0191-8141(87)90147-7**

Gradstein, F.M., Ogg, J.G., and Smith, A. (Eds.), 2004. *A Geologic Time Scale 2004:* Cambridge (Cambridge Univ. Press). **http://www.stratigraphy.org/**

Hanamura, Y., and Ogawa, Y., 1993. Layer-parallel faults, duplexes, imbricate thrusts and vein structures of the Miura group: keys to understanding the Izu fore-arc sediment accretion to the Honshu fore arc. *Isl. Arc,*

2(3):126–141. doi:10.1111/j.1440-1738.1993.tb00081.x

Kimura, G., Screaton, E.J., and Curewitz, D., 2007. NanTroSEIZE Stage 1: NanTroSEIZE shallow megasplay and frontal thrusts. *IODP Sci. Prosp.,* 316. doi:10.2204/iodp.sp.316.2007

Moore, G.F., Bangs, N.L., Taira, A., Kuramoto, S., Pangborn, E., and Tobin, H.J., 2007. Three-dimensional splay fault geometry and implications for tsunami generation. *Science,* 318(5853):1128–1131. doi:10.1126/science.1147195

Moore, G.F., Taira, A., Klaus, A., Becker, L., Boeckel, B., Cragg, B.A., Dean, A., Fergusson, C.L., Henry, P., Hirano, S., Hisamitsu, T., Hunze, S., Kastner, M., Maltman, A.J., Morgan, J.K., Murakami, Y., Saffer, D.M., Sánchez-Gómez, M., Screaton, E.J., Smith, D.C., Spivack, A.J., Steurer, J., Tobin, H.J., Ujiie, K., Underwood, M.B., and Wilson, M., 2001. New insights into deformation and fluid flow processes in the Nankai Trough accretionary prism: results of Ocean Drilling Program Leg 190. *Geochem., Geophys., Geosyst.,* 2(10):1058. doi:10.1029/2001GC000166

Moore, G.F., Taira, A., Klaus, A., et al., 2001. *Proc. ODP, Init. Repts.,* 190: College Station, TX (Ocean Drilling Program). doi:10.2973/odp.proc.ir.190.2001

Shipboard Scientific Party, 2001a. Site 1173. *In* Moore, G.F., Taira, A., Klaus, A., et al., *Proc. ODP, Init. Repts.,* 190: College Station, TX (Ocean Drilling Program), 1–147. doi:10.2973/odp.proc.ir.190.104.2001

Shipboard Scientific Party, 2001b. Site 1174. *In* Moore, G., Taira, A., Klaus, A., et al., *Proc. ODP, Init. Repts.,* 190: College Station, TX (Ocean Drilling Program), 1–149. doi:10.2973/odp.proc.ir.190.105.2001

Ujiie, K., Maltman, A.J., and Sánchez-Gómez, M., 2004. Origin of deformation bands in argillaceous sediments at the toe of the Nankai accretionary prism, southwest Japan. *J. Struct. Geol.,* 26(2):221–231. doi:10.1016/j.jsg.2003.06.001

Yamano, M., Kinoshita, M., Goto, S., and Matsubayashi, O., 2003. Extremely high heat flow anomaly in the middle part of the Nankai Trough. *Phys. Chem. Earth,* 28(9–11):487–497. doi:10.1016/S1474-7065(03)00068-8

Publication: 11 March 2009
MS 314315316-135

Figure F1. Hole locations, Sites C0006 and C0007. Solid lines = seismic profile coverage.

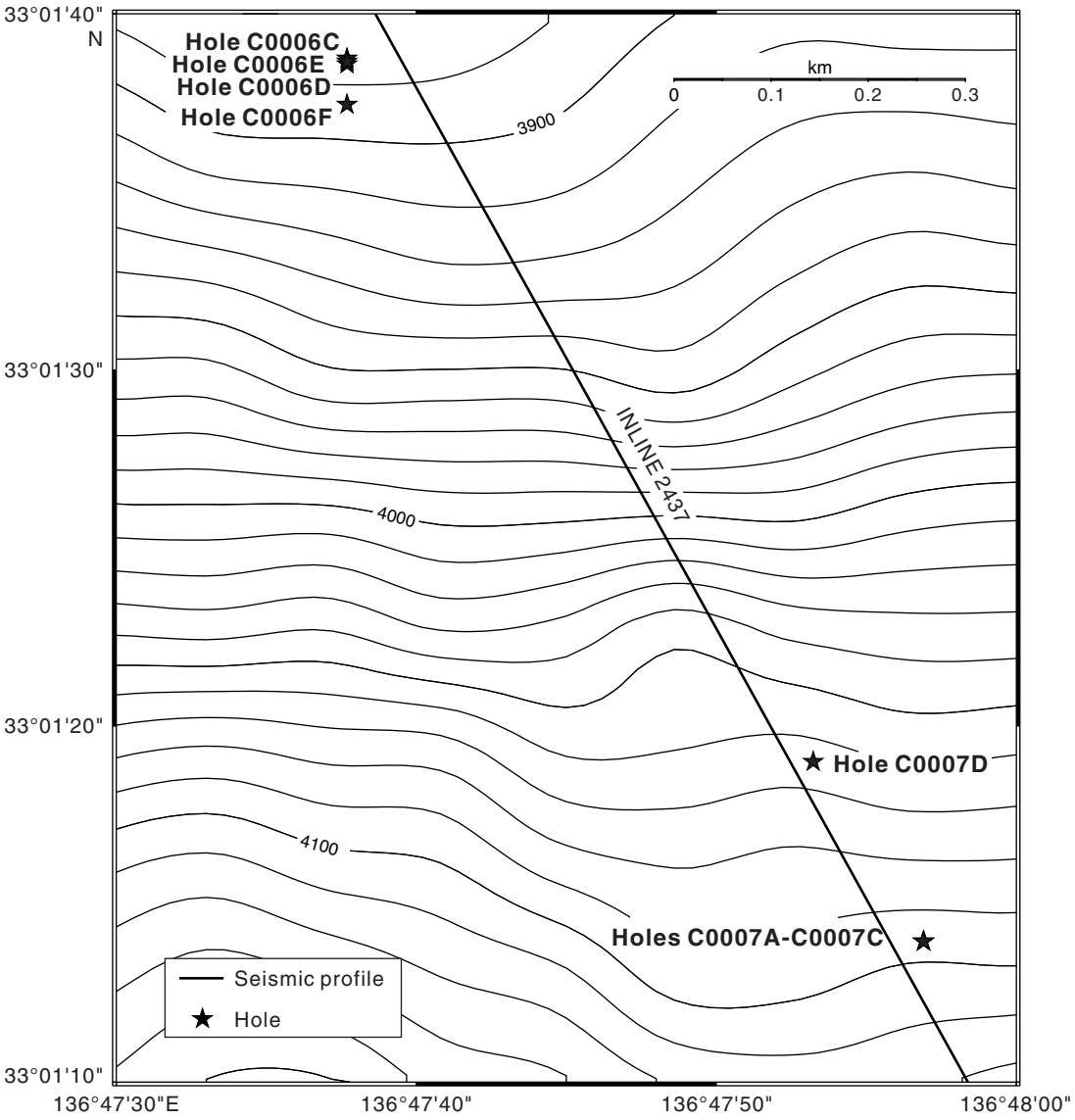

Figure F2. 3-D seismic profile through Sites C0006 and C0007 (Moore et al., 2007; see **Moore et al.**). VE = vertical exaggeration.

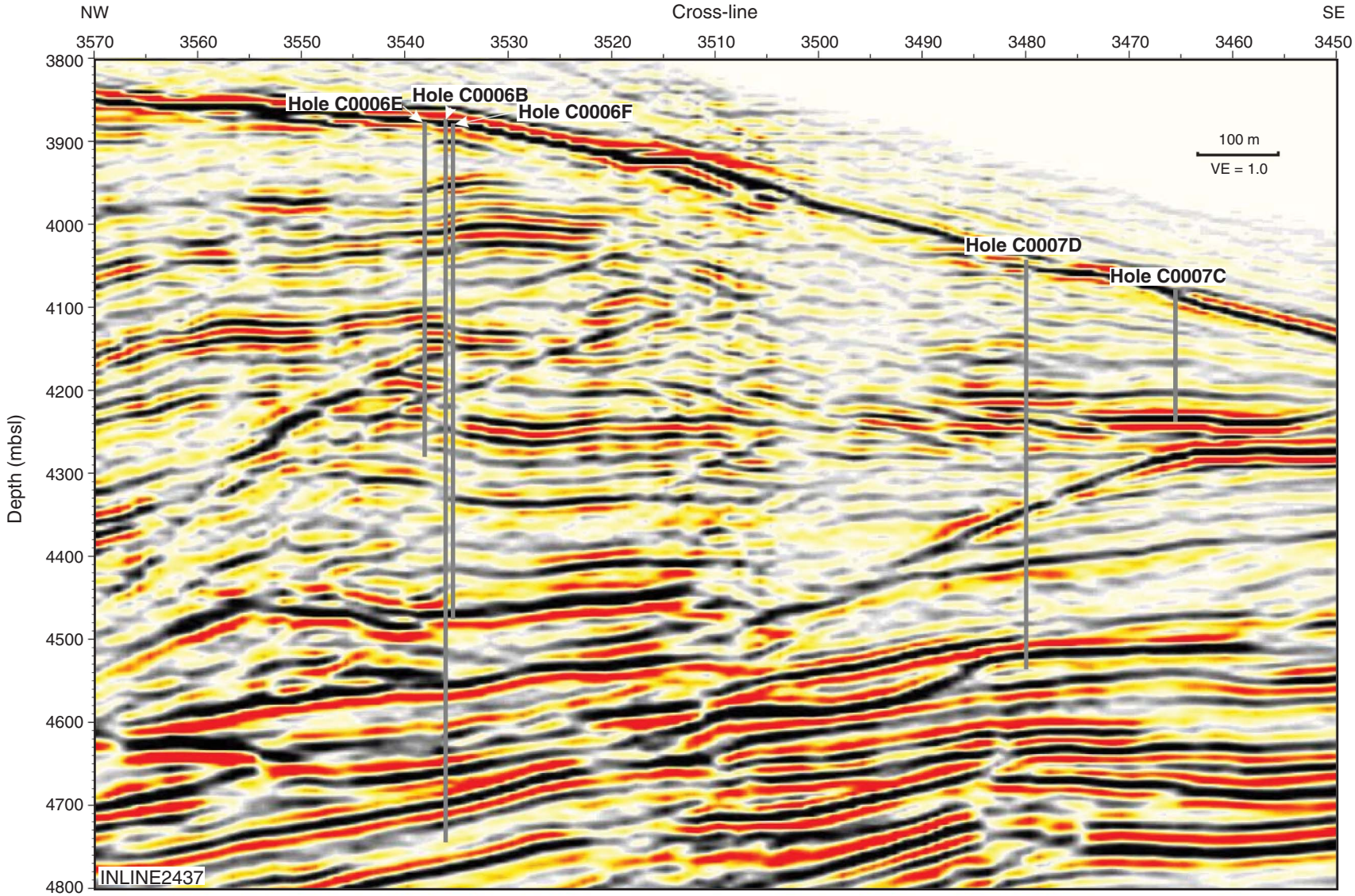

Figure F3. Core recovery and sand and silt distribution. **A.** Core recovery and lithologic units, Holes C0007A–C0007C. CSF = core depth below seafloor. (**Continued on next two pages.**)

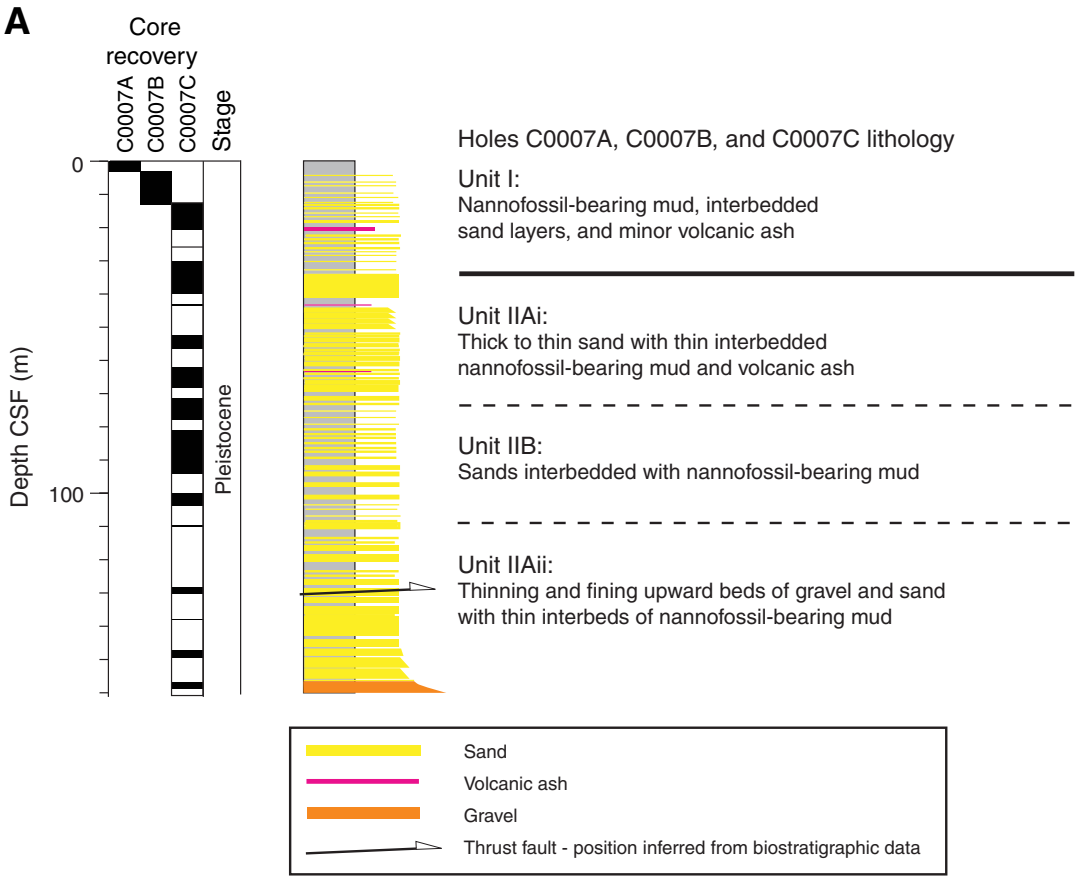

Figure F3 (continued). B. Core recovery and lithologic units, Hole C0007D. (Continued on next page.)

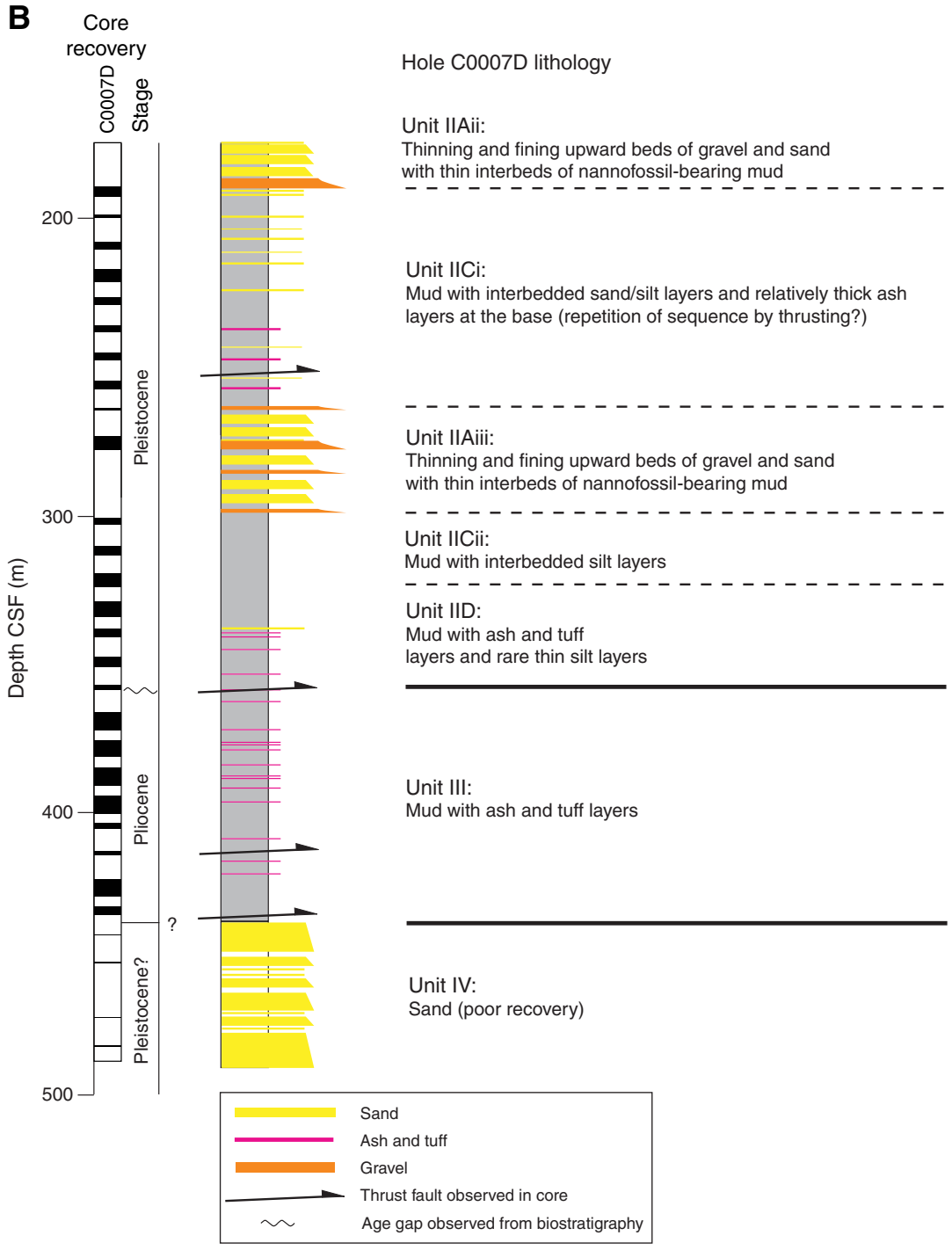

Figure F3 (continued). C. Distribution of sand and silt layers, Site C0007.

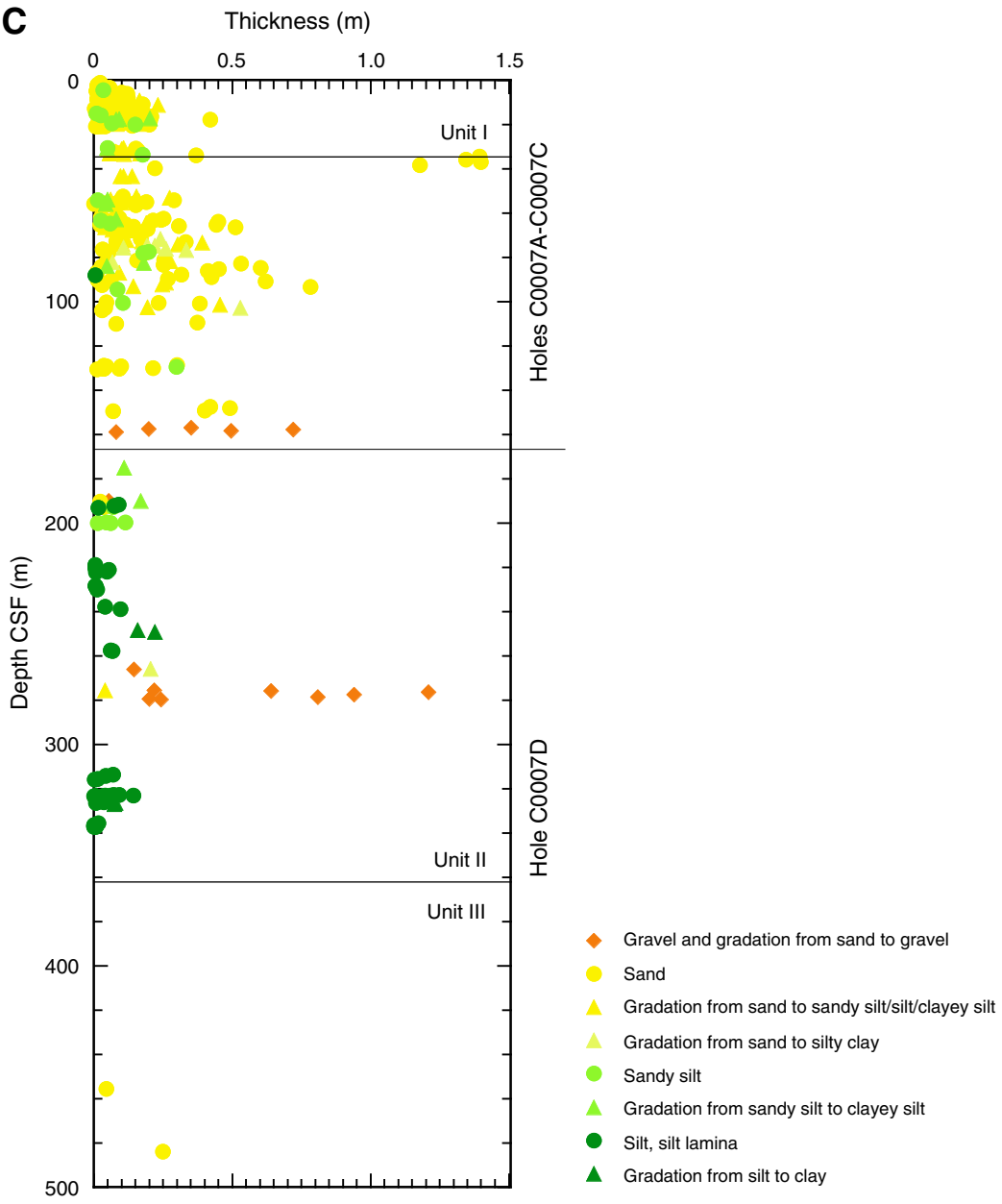

Figure F4. Photographs of core examples, Unit I. **A.** Graded sand to mud intervals (typical turbidite sequences) (interval 316-C0007B-1H-6, 40–89 cm). **B.** Reverse faults (white dashed lines) cutting graded beds of sand and mud (interval 316-C0007C-1H-1, 17–45 cm). **C.** Mafic ash (interval 316-C0007B-1H-4, 0–17 cm).

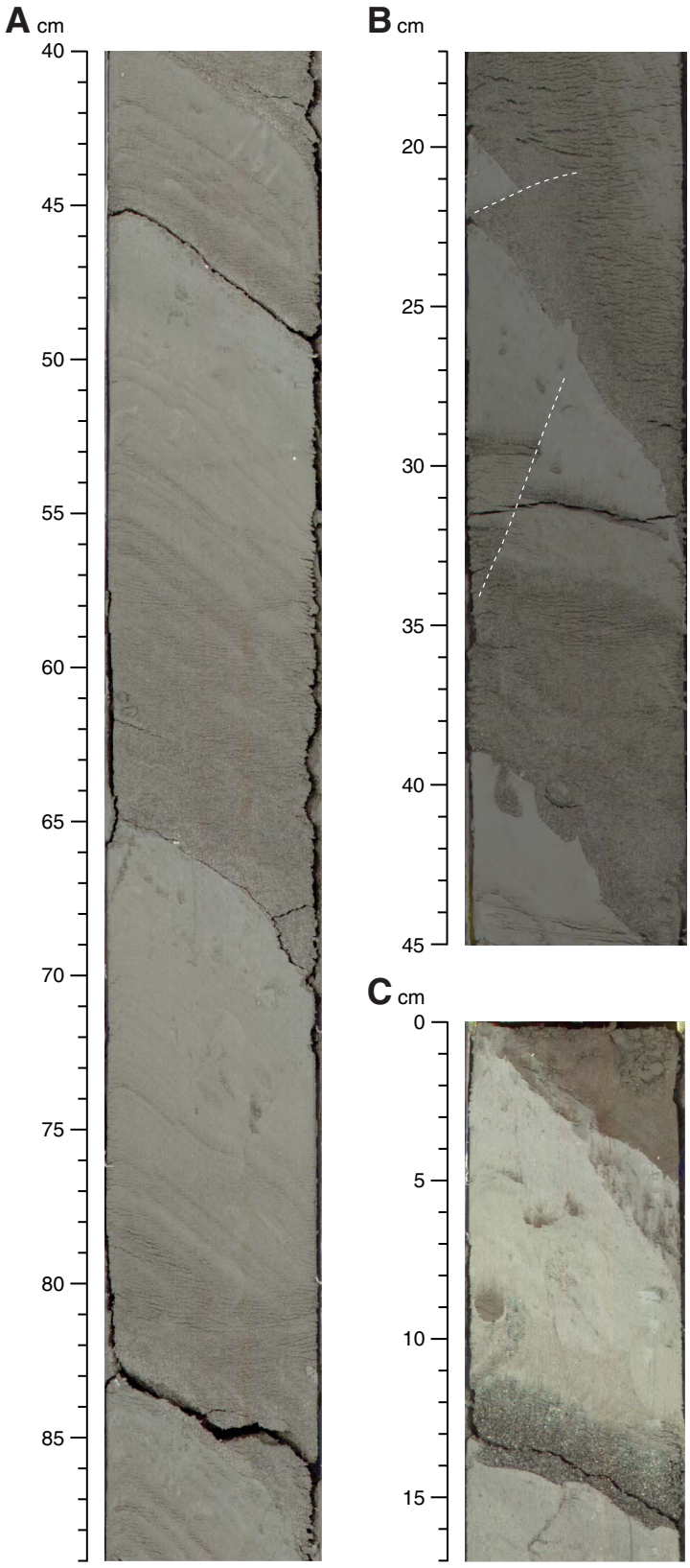

Figure F5. XRD data. **A.** Holes C0007A, C0007B, and C0007C. **B.** Hole C0007D. CSF = core depth below seafloor.

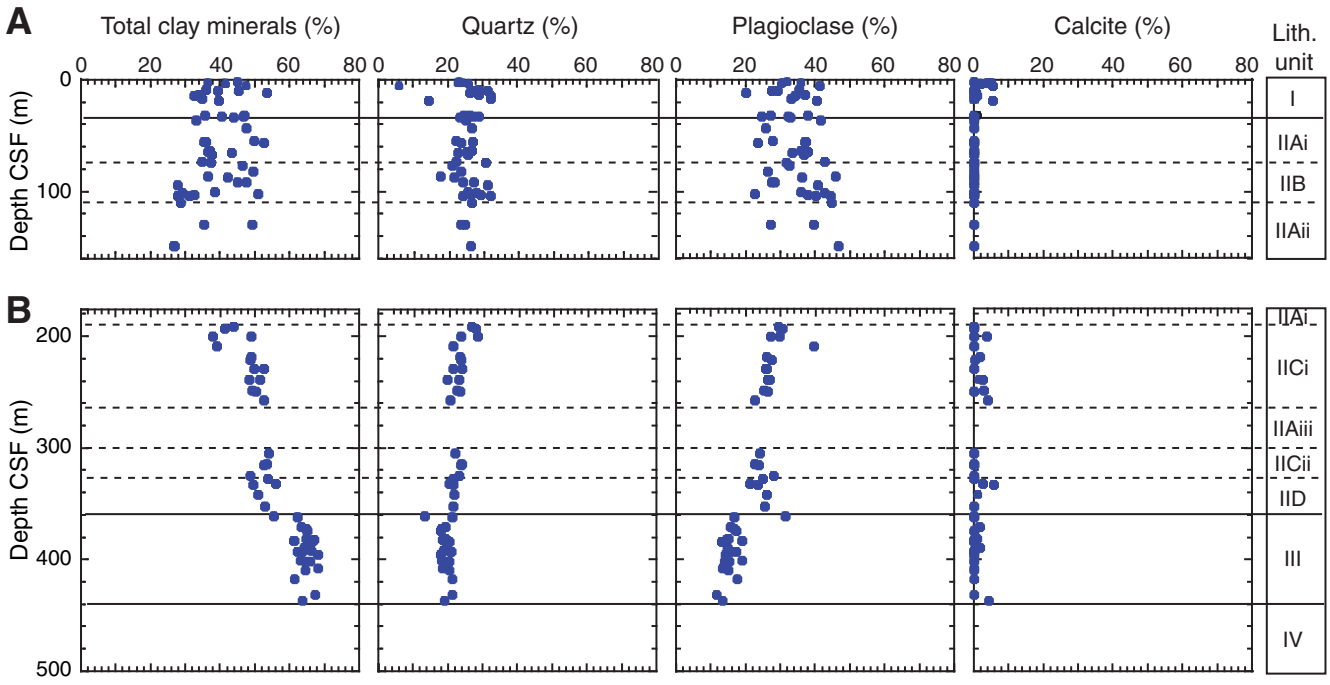

Figure F6. Photographs of pumice, Subunit IIA. **A.** Pumice-bearing massive sand (interval 316-C0007C-3H-5, 72–110 cm). Inverse grading may reflect low density of pumice clasts. **B.** Diverse pumice particles (Sample 316-C0007C-1H-6, 115 cm). **C.** Highly elongate pumice clast (Sample 316-C0007C-1H-6, 115 cm).

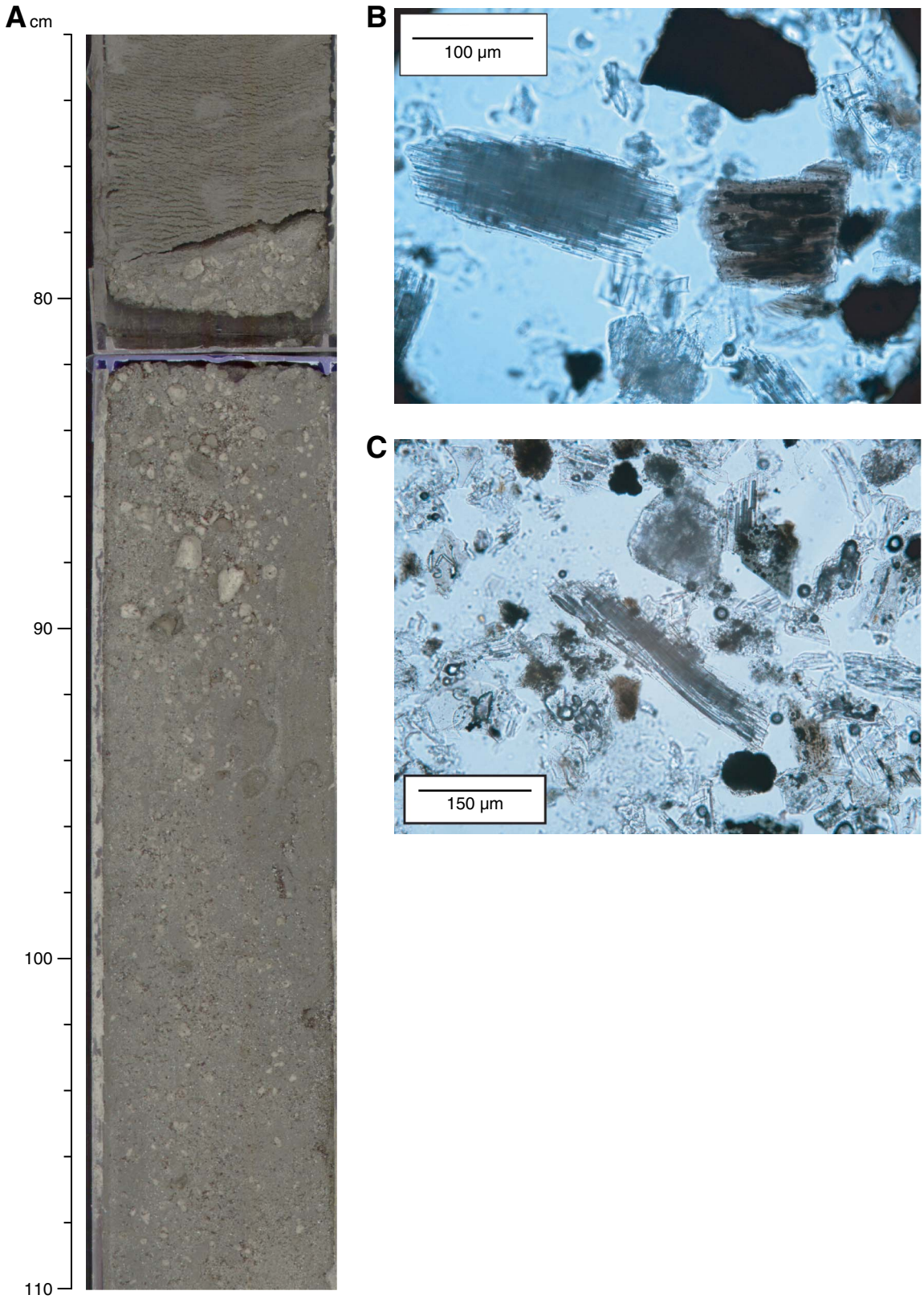

Figure F7. Photographs of gravel and sand, Subunit IIC. **A.** Graded sand to mud (interval 316-C0007C-16H-1, 32–84 cm). **B.** Graded interval from gravel to sand (interval 316-C0007C-17H-1, 2–56 cm). **C.** Gravel (interval 316-C0007C-17H-2, 3–26 cm). **D.** Pyrite-coated clast (Section 316-C0007C-17H-2).

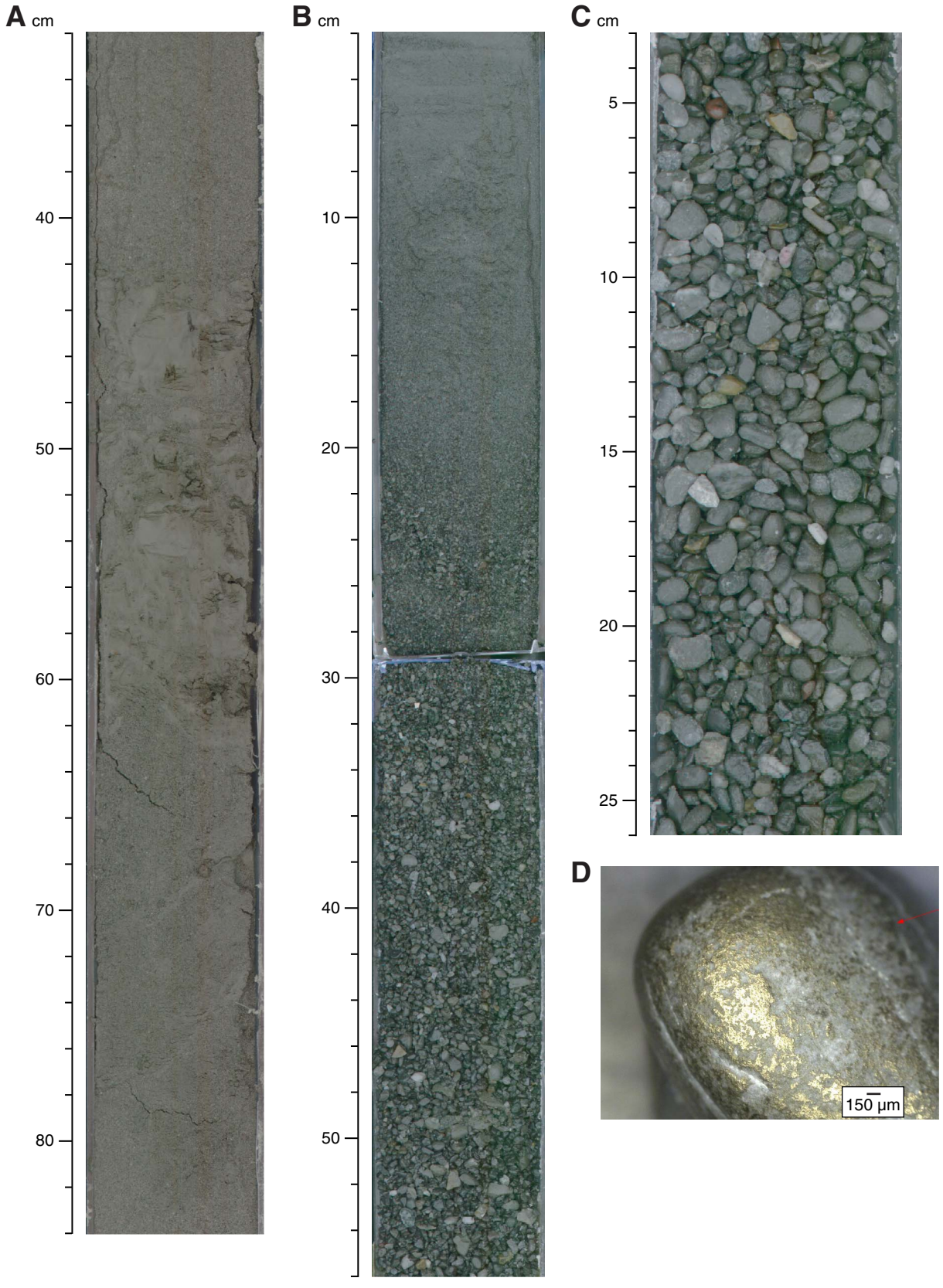

Figure F8. Photomicrographs of common clast types in gravel. **A.** Lithic sandstone, highly compacted. **B.** Calcitic mudstone. **C.** Foliated quartzite (mylonite). **D.** Chlorite schist. **E.** Basalt (plane-polarized light). **F.** Same as E (cross-polarized light). **G.** Plutonic rock (granite or gneiss) (plane-polarized light). **H.** Same as G (cross-polarized light).

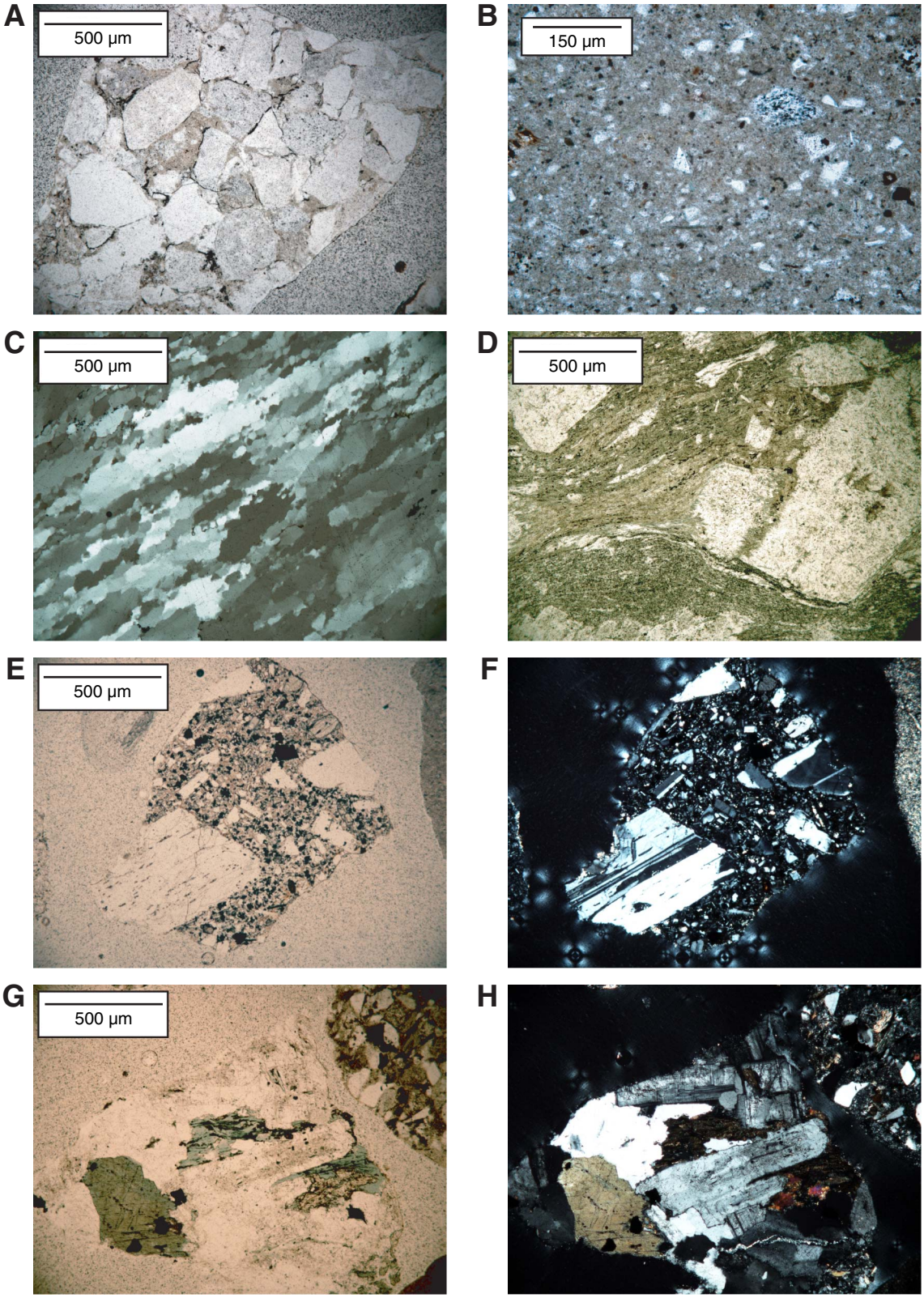

Figure F9. Photomicrographs of chert clasts. **A.** Structureless microcrystalline quartz. **B.** Radiolarian chert (plane-polarized light). **C.** Same as B (cross-polarized light). **D.** Spiculite (plane-polarized light). **E.** Same as D (cross-polarized light). **F.** Veined chert (plane-polarized light). **G.** Same as F (cross-polarized light).

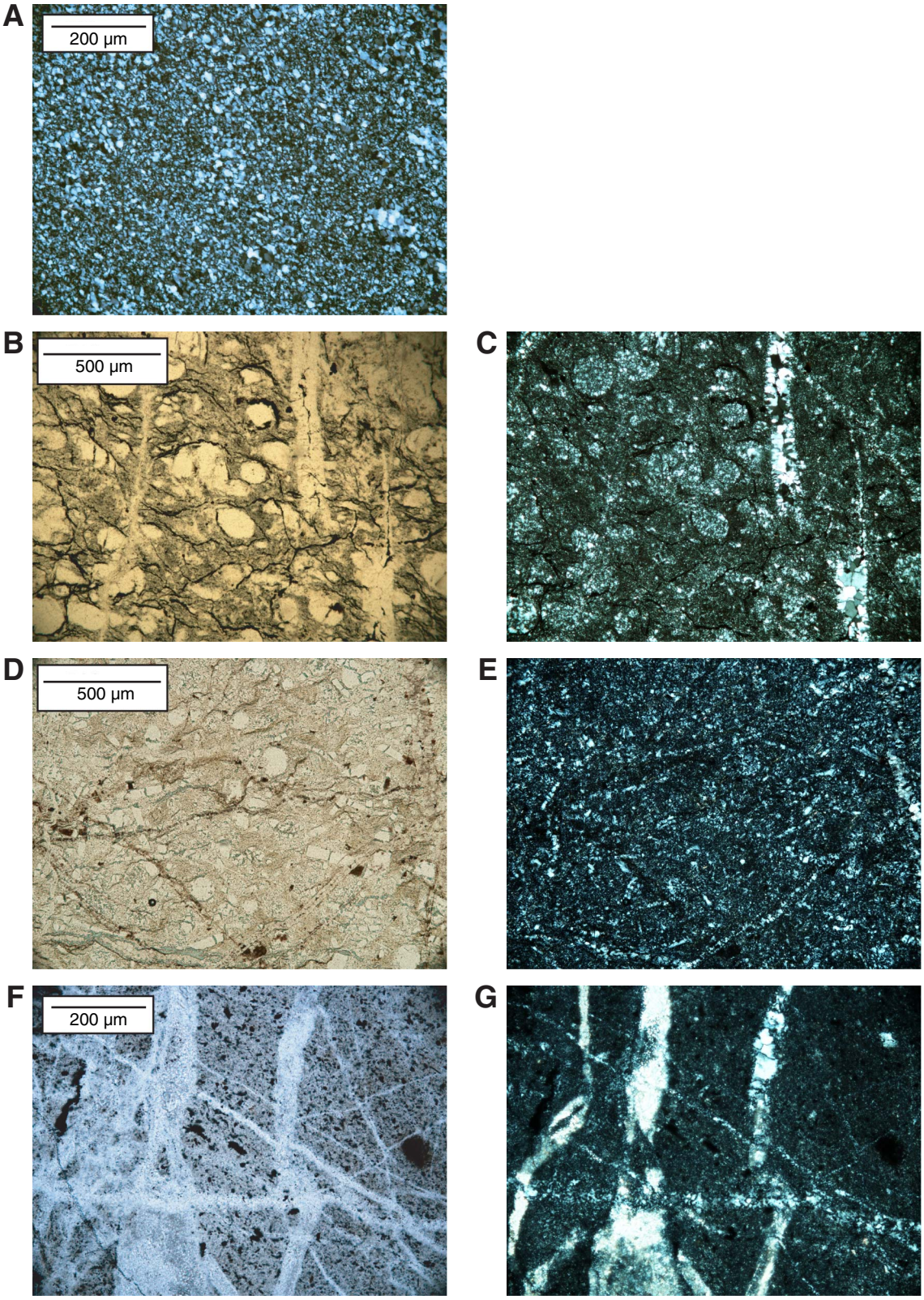

Figure F10. Photograph of gravel, Subunit IIE (interval 316-C0007C-12R-3, 37–70 cm).

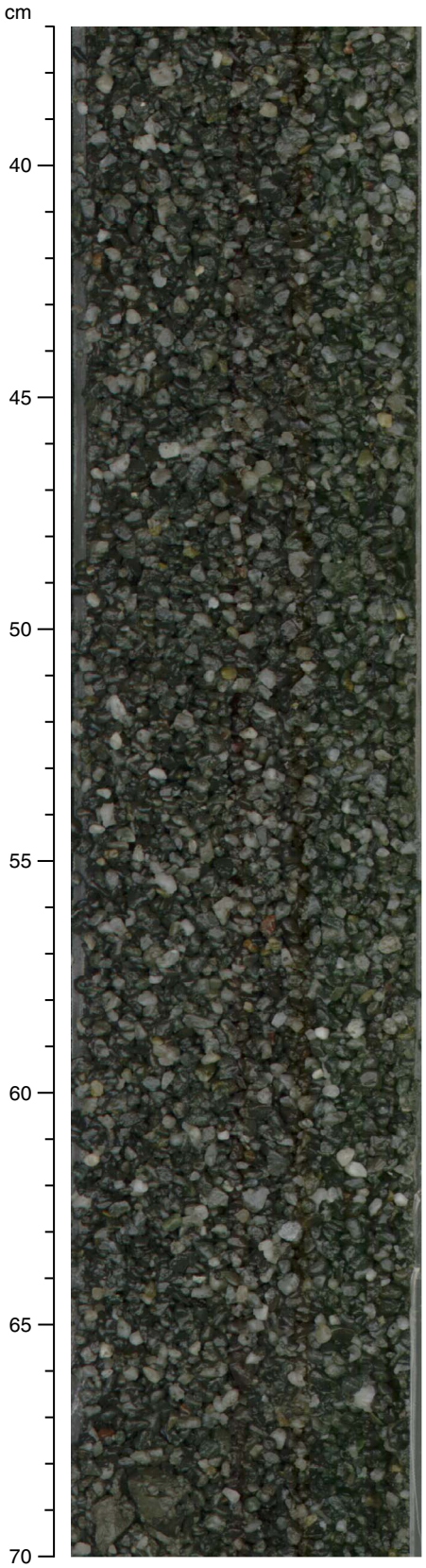

Figure F11. Ash layers and ash, Site C0007. **A.** Distribution and thickness of volcanic ash layers, Holes C0007A–C0007C. **B.** Distribution and thickness of volcanic ash layers, Hole C0007D. **C.** Typical light gray ash layer (interval 316-C0007D-9R-2, 10–23 cm). **D.** Carbonate-cemented ashstone (interval 316-C0007D-25R-2, 46–56 cm). **E.** Brown glass with microlites (Sample 316-C0007B-1H-4, 2 cm). CSF = core depth below seafloor.

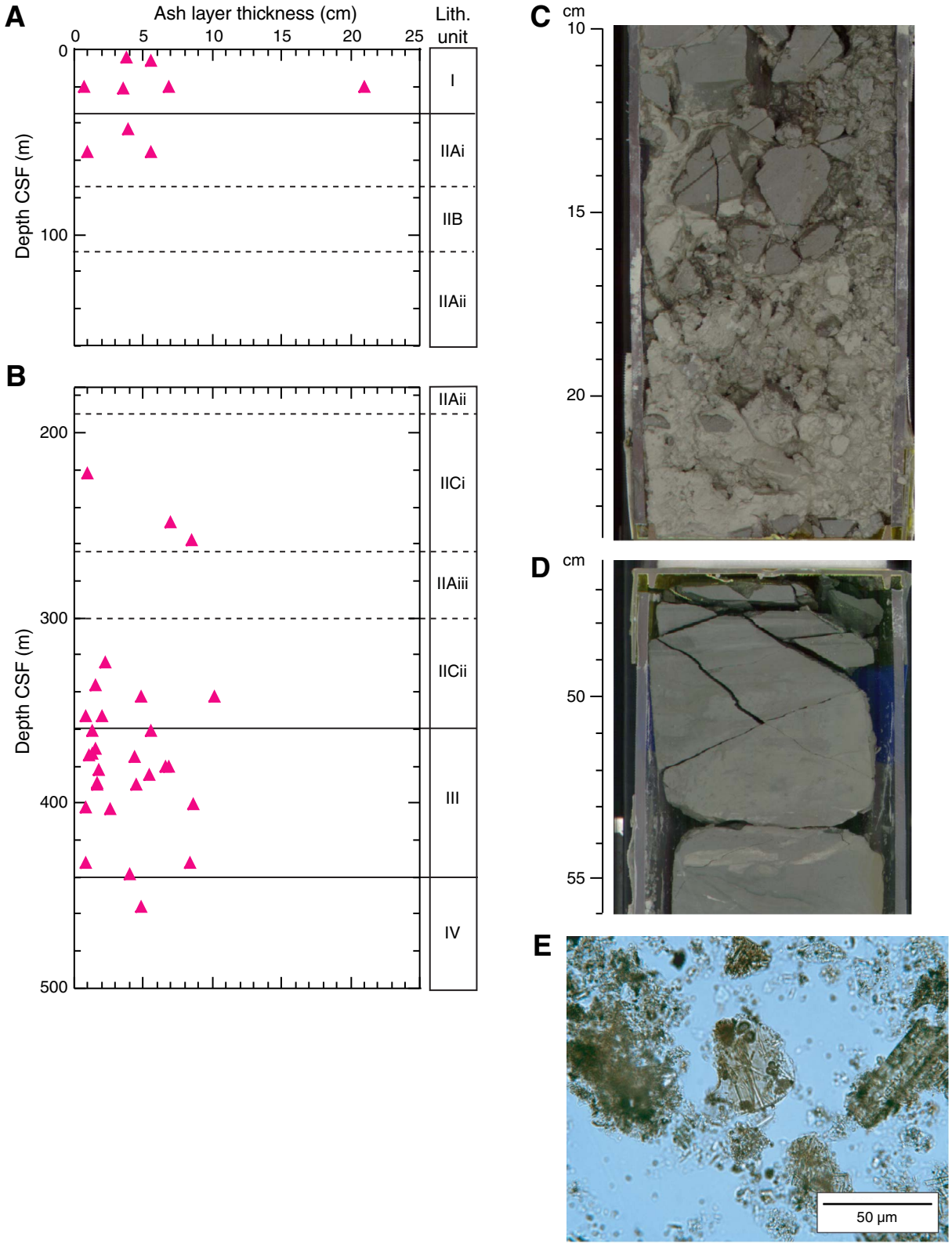

Figure F12. Photomicrographs of pyritized and ash-filled burrows, Subunit IIA and Unit III. **A.** Vertical pyritized burrow, Subunit IIA (interval 316-C0007D-19R-2, 72–73 cm). **B.** Pyritized *Chondrites,* Unit III (Section 316-C0007D-25R-1, 84 cm). **C.** Ash-filled *Chondrites,* Unit III (interval 316-C0007D-25R-3, 106–109 cm).

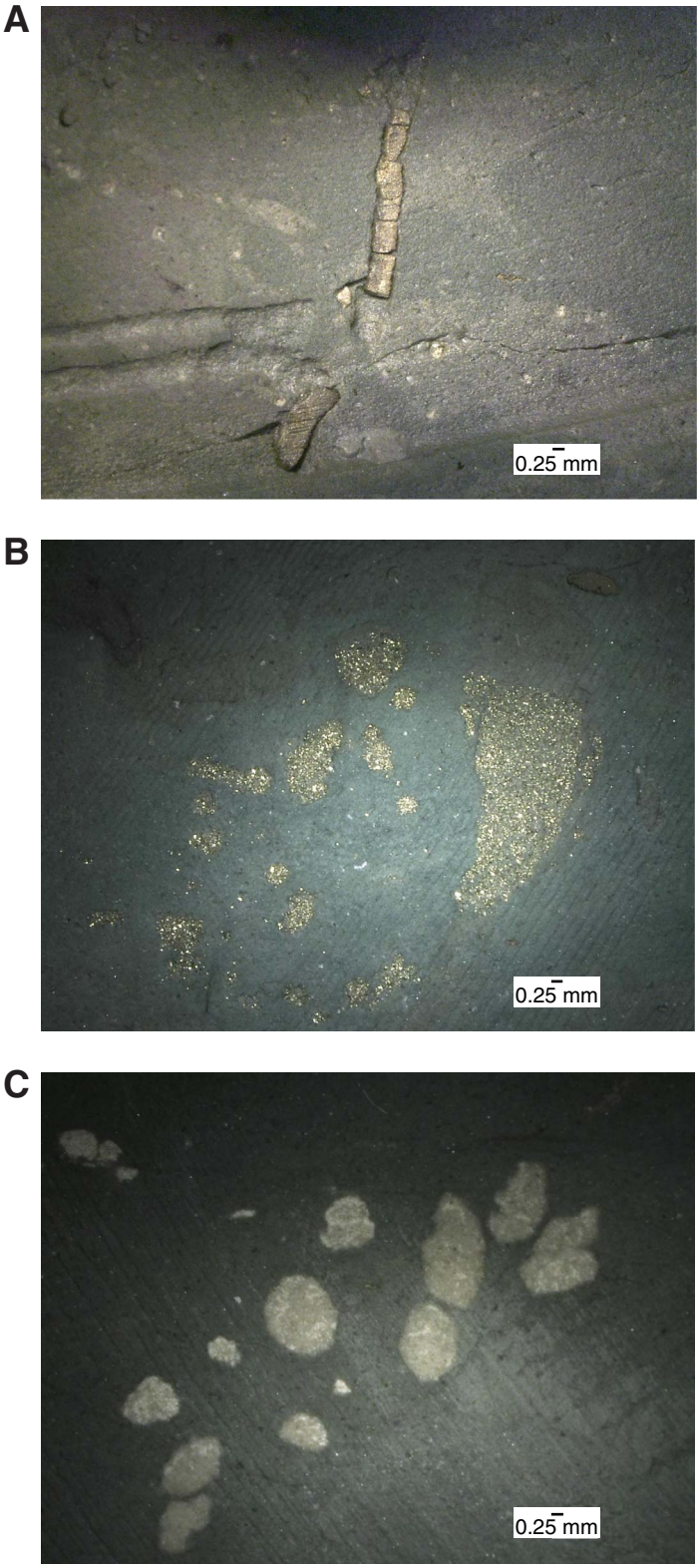

Figure F13. Core photograph of dark gray to black sand of inferred Pleistocene age, Unit IV (interval 316-C0007D-35R-1, 0–25 cm).

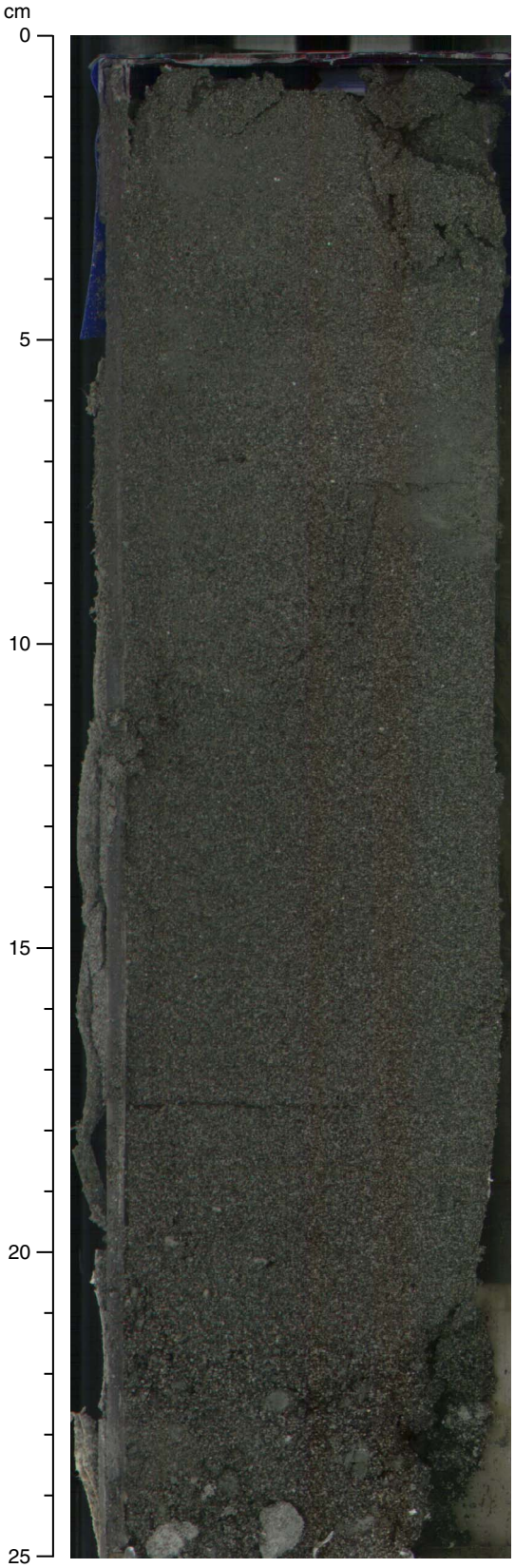

Figure F14. Photomicrographs of silt grains with isopachous rims of oriented clay. **A.** Cross-polarized light. Arrows = birefringent clay rims, circles = smaller silt particles with clay rims that are slightly out of the plane of focus. **B.** Gypsum plate (cross-polarized light). Strong orientation of the grain-rimming clays is indicated by blue and yellow regions of the rims.

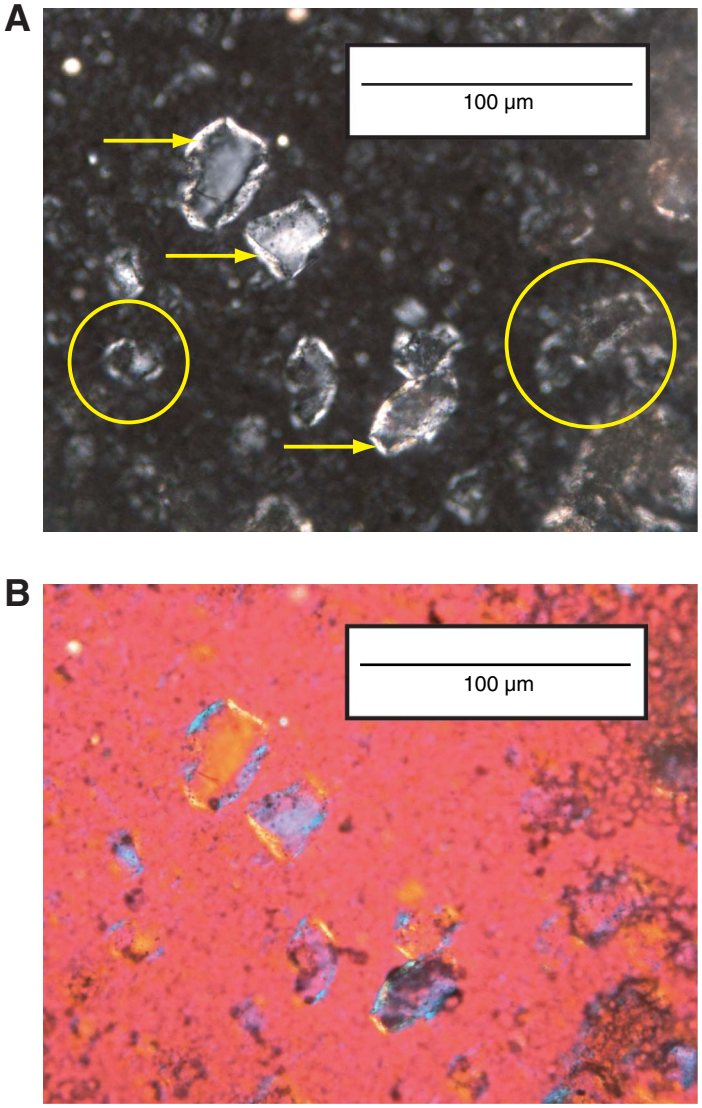

Figure F15. Computed tomography (CT) number vs. depth. **A.** Holes C0007A–C0007C. **B.** Hole C0007D. Average value for each core obtained from ~70 measurements with a 4–10 cm interval. CSF = core depth below seafloor.

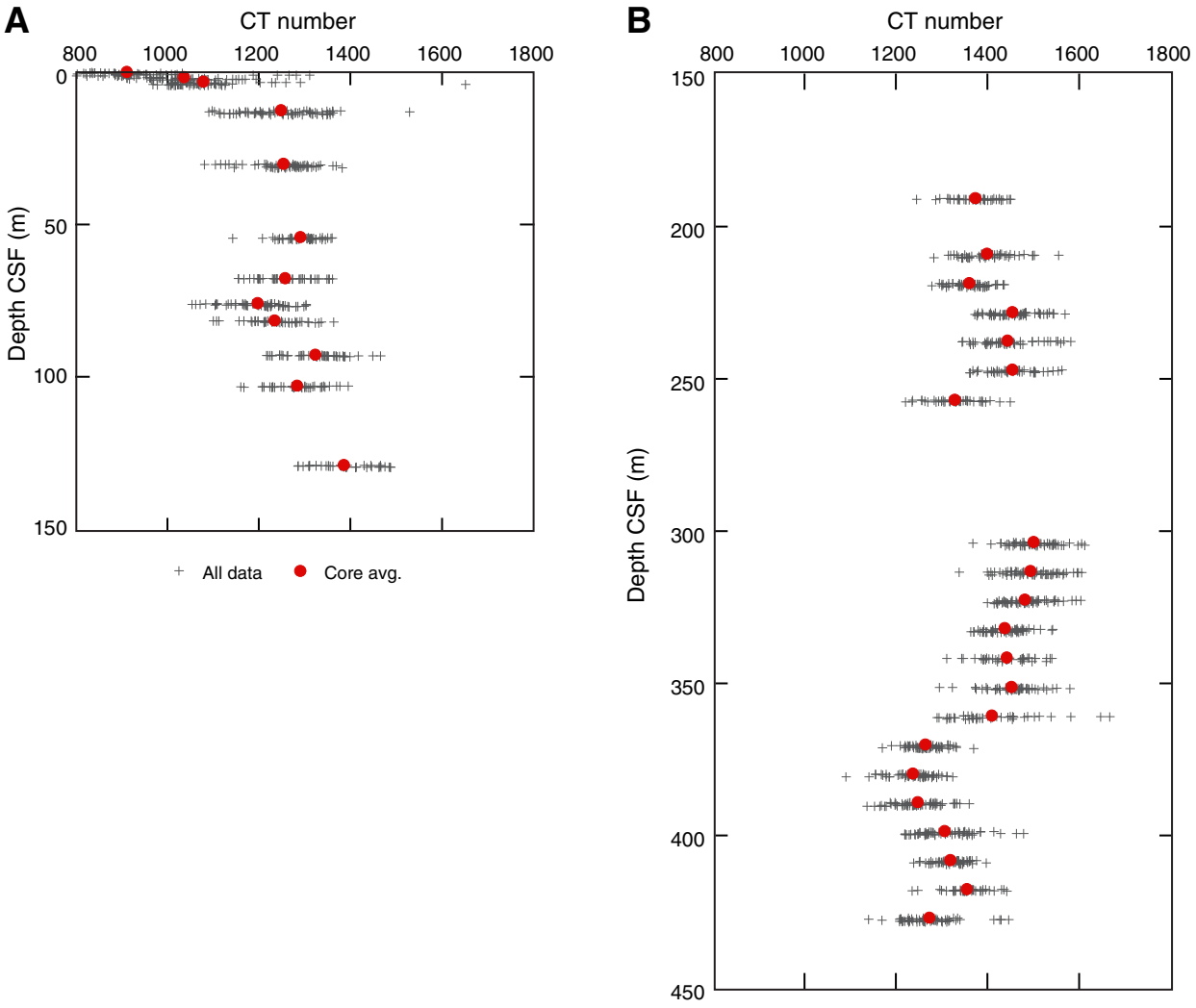

Figure F16. Distribution of planar structures with depth. Lithologic divisions and core recovery with depth are shown at right. **A.** Holes C0007A, C0007B, and C0007C. Note that deformation bands are concentrated between 230 and 248 m core depth below seafloor (CSF) but most of their orientations cannot be measured because of poor core quality (e.g., drilling-induced brecciation). Shaded bands = three fault zones recognized in the prism. Blacks lines in shaded bands = zones of concentrated deformation in fault zones (see text for further explanation). (**Continued on next page.**)

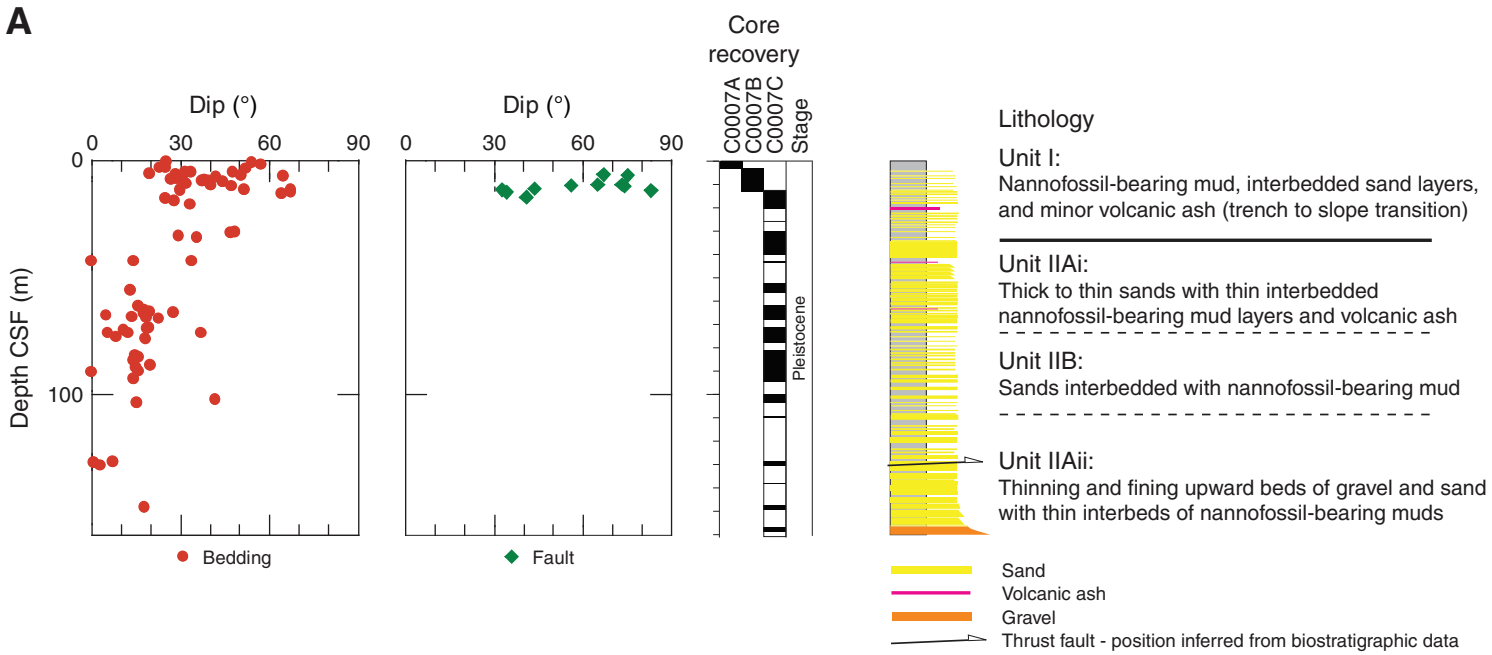

Figure F16 (continued). B. Hole C0007D.

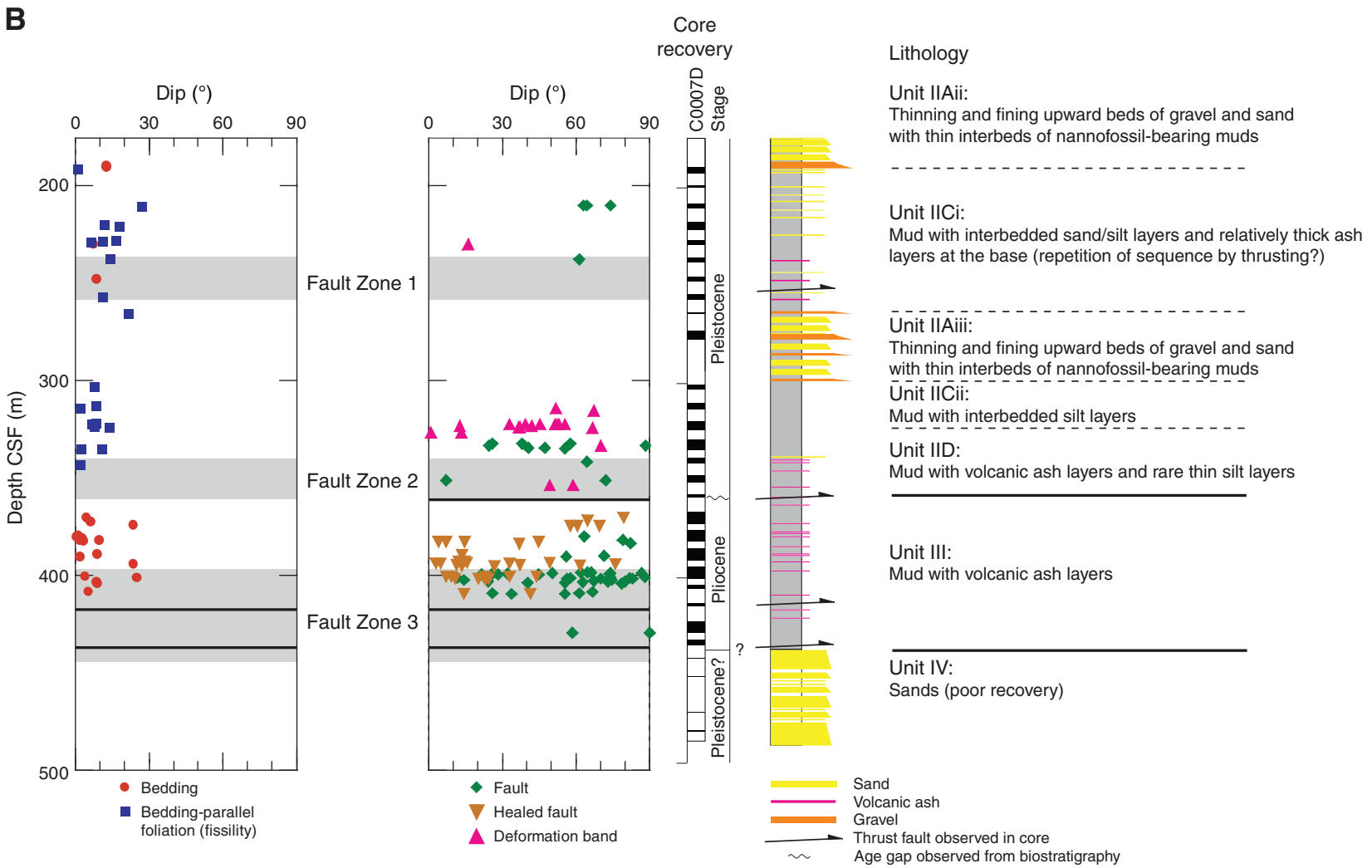

Figure F17. Lower-hemisphere equal-area projections of planar structures in lithologic Unit I. **A.** Poles to bedding surfaces. **B.** Poles to fault planes.

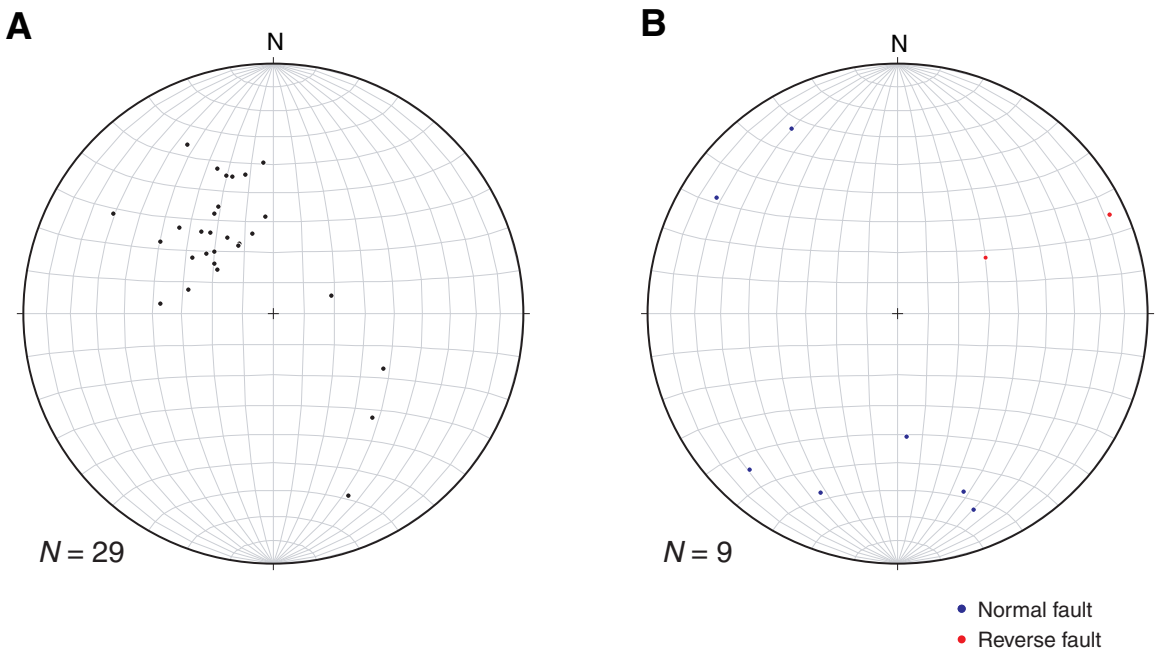

Figure F18. Core photographs of deformation in lithologic Unit I. **A.** Interval 316-C0007C-1H-1, 12–44 cm. **B.** Interval 316-C0007C-1H-3, 12–44 cm. Half arrows = shear sense of fault.

Figure F19. Lower-hemisphere equal-area projections of planar structures in the prism. **A.** Bedding. **B.** Fissility.

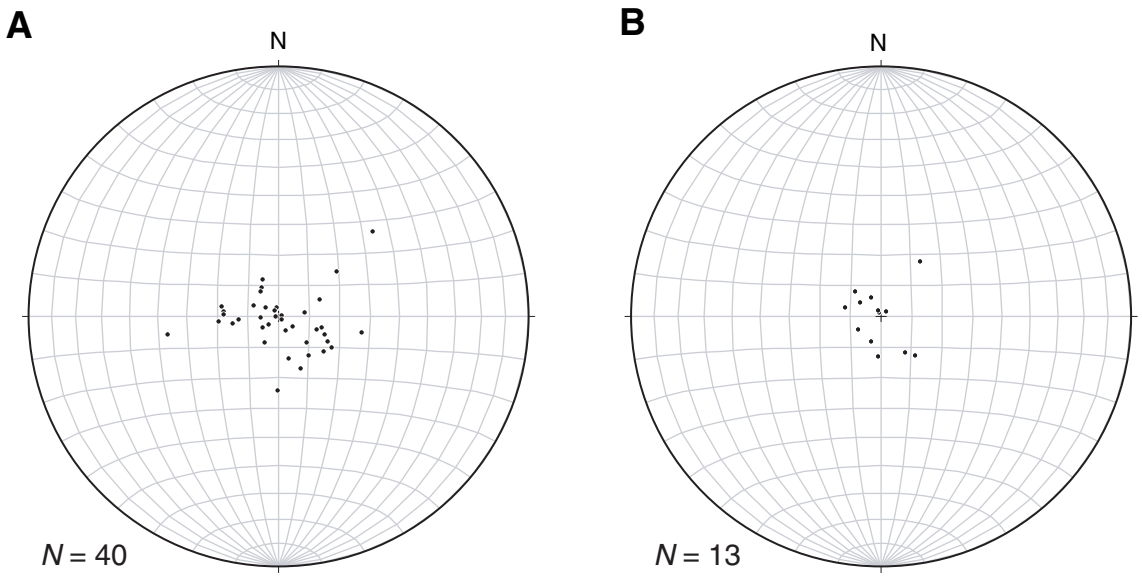

Figure F20. Deformation bands in the prism. **A.** Typical appearance of deformation bands showing a conjugate geometry of reverse slip (interval 316-C0007D-8R-2, 27–31 cm). **B.** Sketch of A. Half arrows = sense of shear of deformation bands. **C.** Computed tomography (CT) image slice of deformation band cut perpendicular to core axis (interval 316-C0007D-17R-1, 67.75 cm).

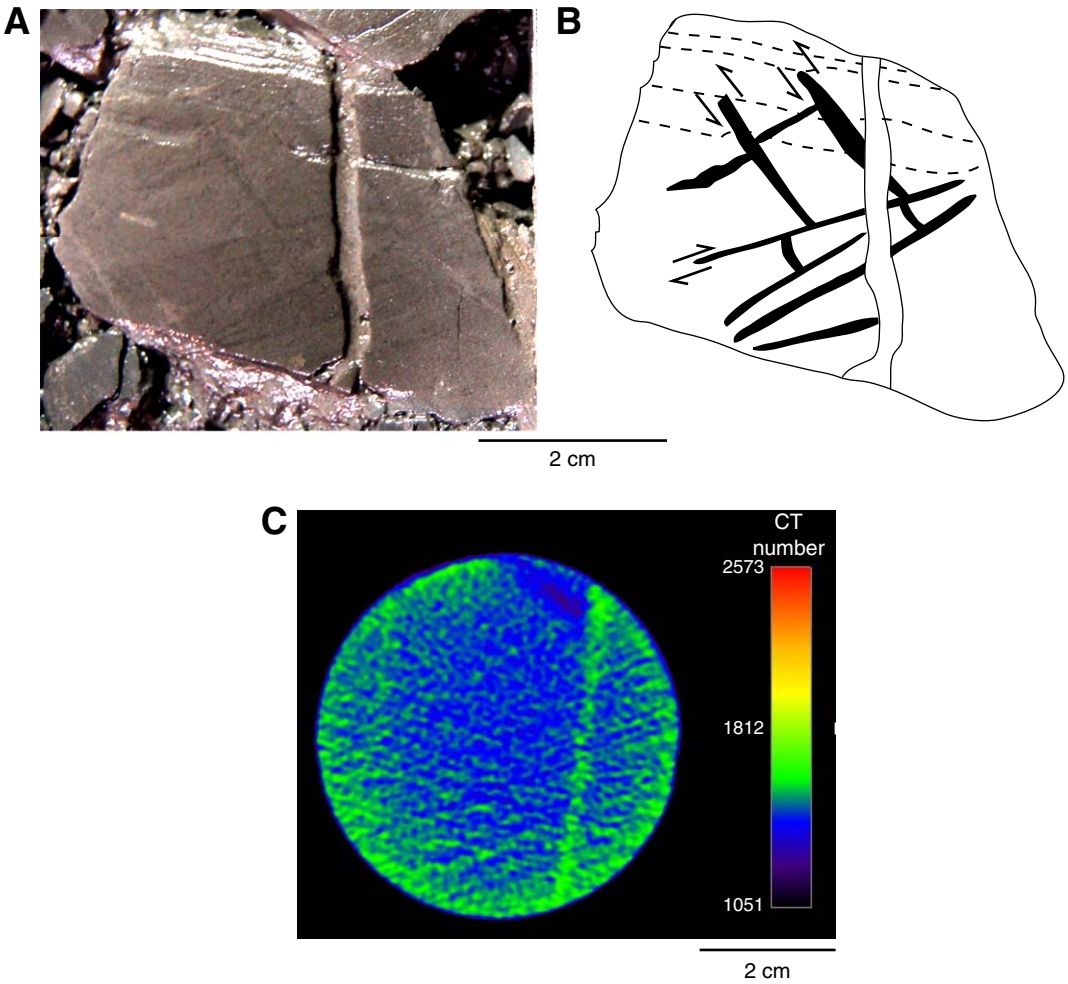

Figure F21. Lower-hemisphere equal-area projections of deformation bands.

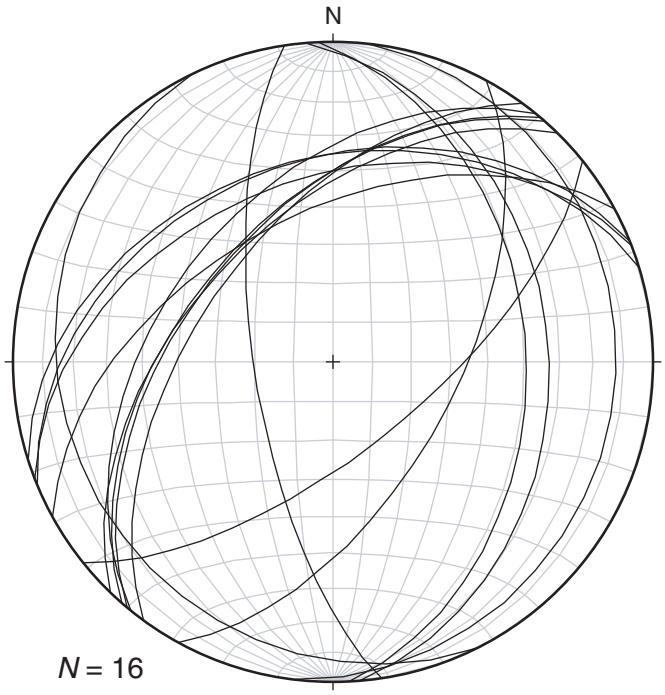

Figure F22. Healed faults in bioturbated hemipelagic mudstone. **A.** Photograph of healed fault showing normal slip (interval 316-C0007D-22R-2, 31–39 cm). Half arrows = sense of shear. **B.** Lower-hemisphere equal-area projections of healed faults that dip between 30° and 90°. **C.** Lower-hemisphere equal-area projections of healed faults that dip <30°.

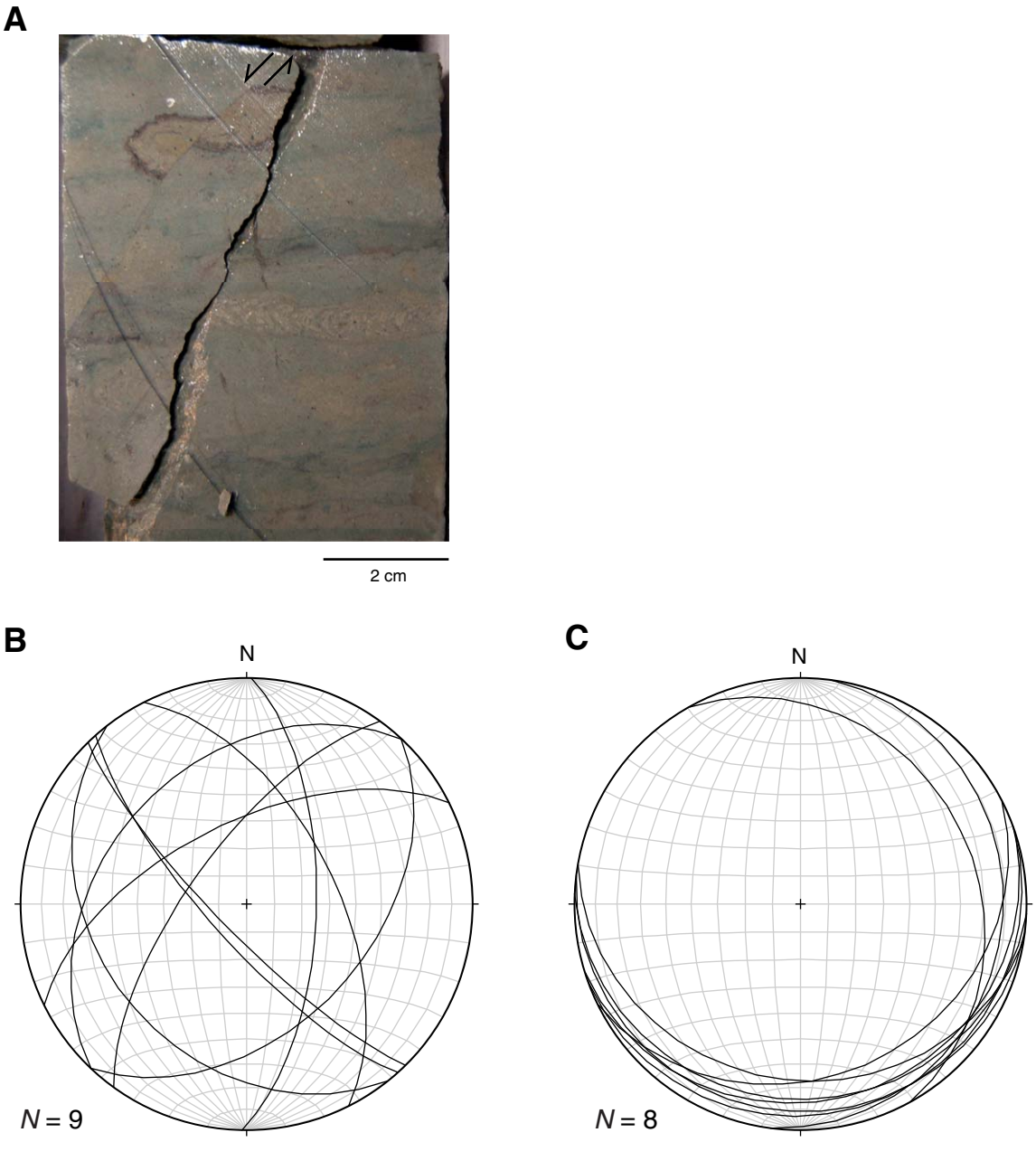

Figure F23. Photograph showing typical appearance of sediment-filled veins (interval 316-C0007D-22R-3, 127–133 cm).

Figure F24. Distribution of structural elements in fault Zone 1. CT images of three similar looking ash layers in the fault zone, which may record duplication by faults in the zone. CSF = core depth below seafloor. Solid lines with half arrows = locations of possible reverse faults.

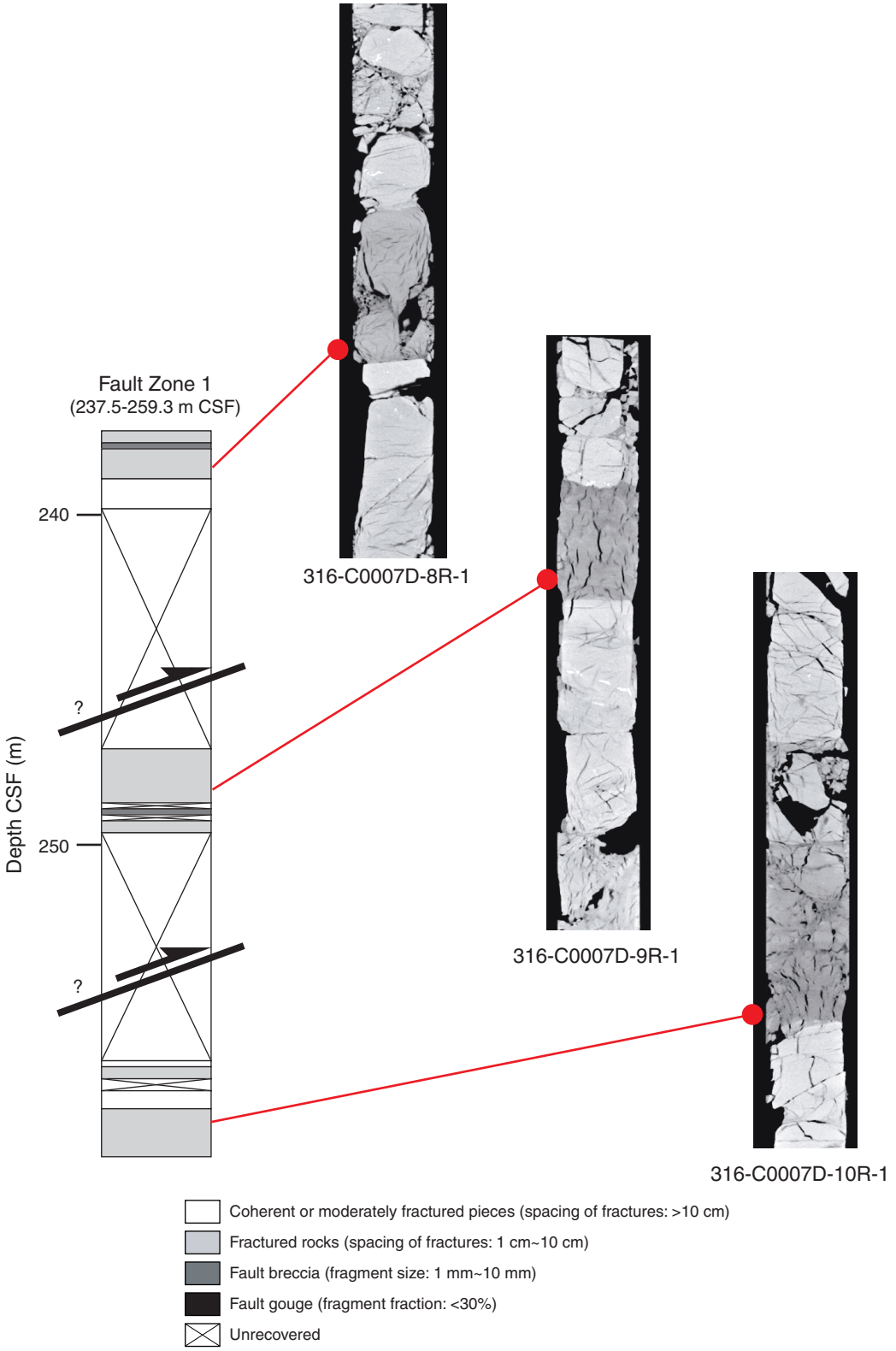

Figure F25. Core photograph showing appearance of brecciated mudstone in fault Zone 1 (interval 316-C0007D-8R-1, 22–35 cm).

Figure F26. Distribution of structural elements in fault Zone 2. CSF = core depth below seafloor.

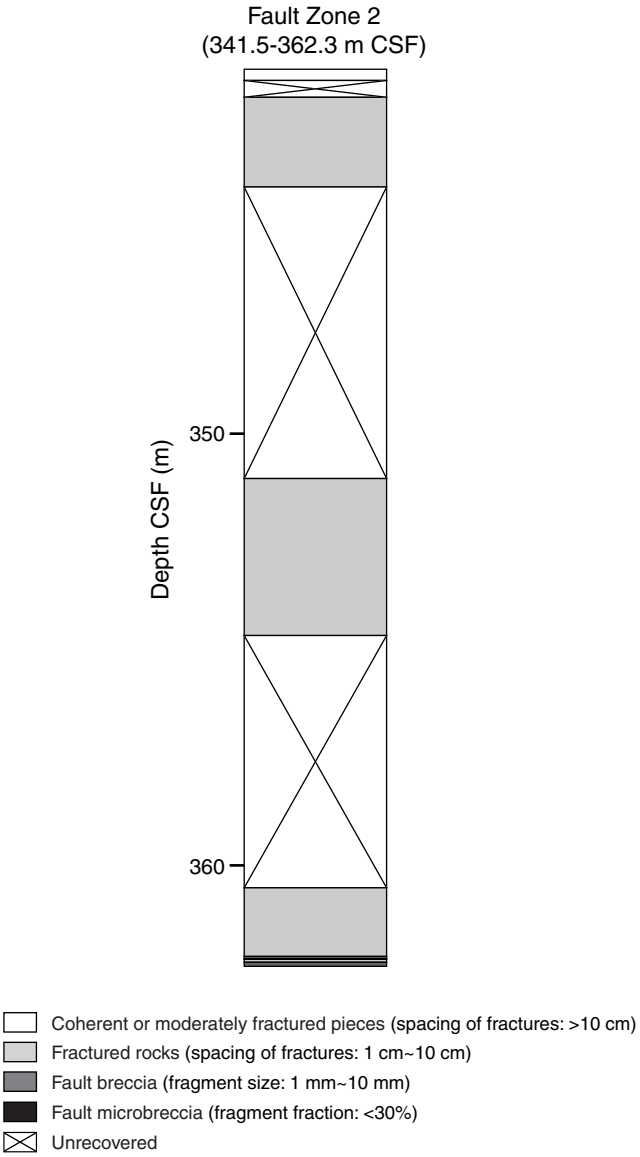

Figure F27. Core photographs of structures in fault Zone 2. **A.** Fractured mudstone (interval 316-C0007D-20R-1, 14–41 cm). **B.** Fault breccia and fault gouge (double arrow) (interval C0007D-21R-CC, 16–30 cm).

Figure F28. Distribution of structural elements in fault Zone 3. CSF = core depth below seafloor.

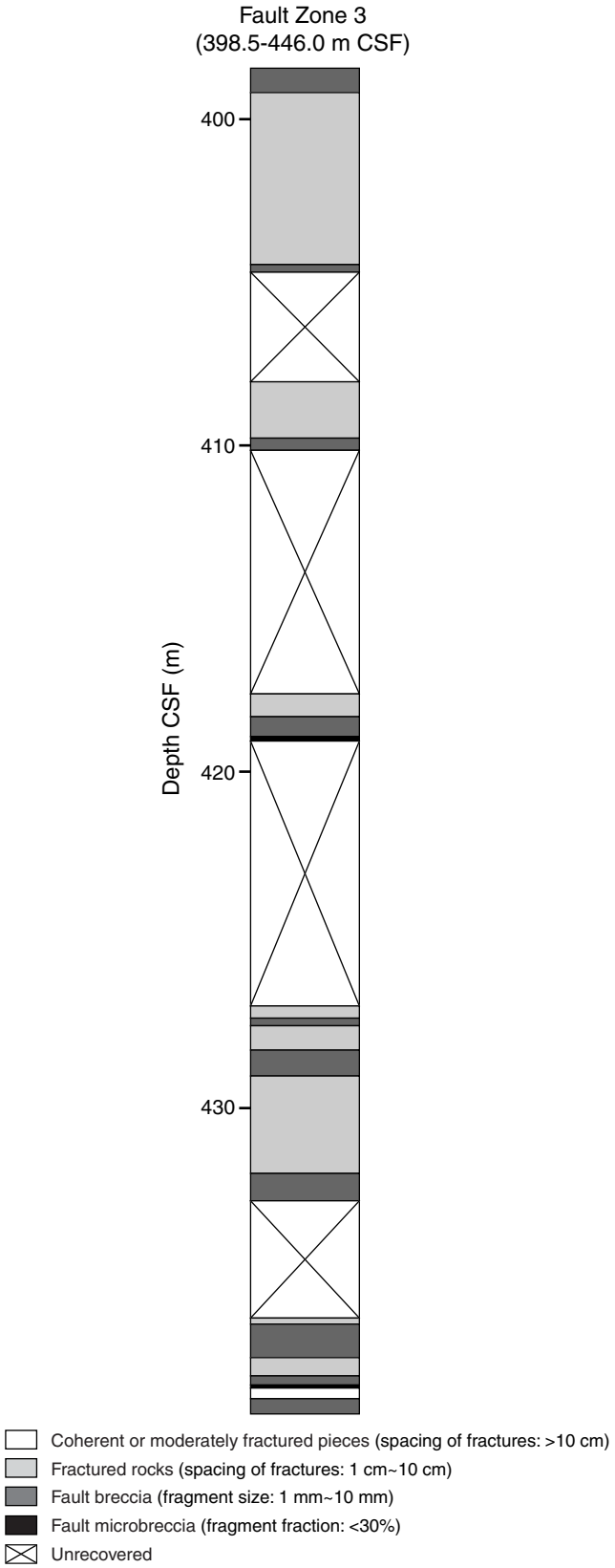

Figure F29. Core photographs of structures in fault Zone 3. **A.** Fractured hemipelagic mudstone (interval 316-C0007D-25R-1, 61–81 cm). **B.** Brecciated hemipelagic mudstone (interval C0007D-28R-2, 30–50 cm).

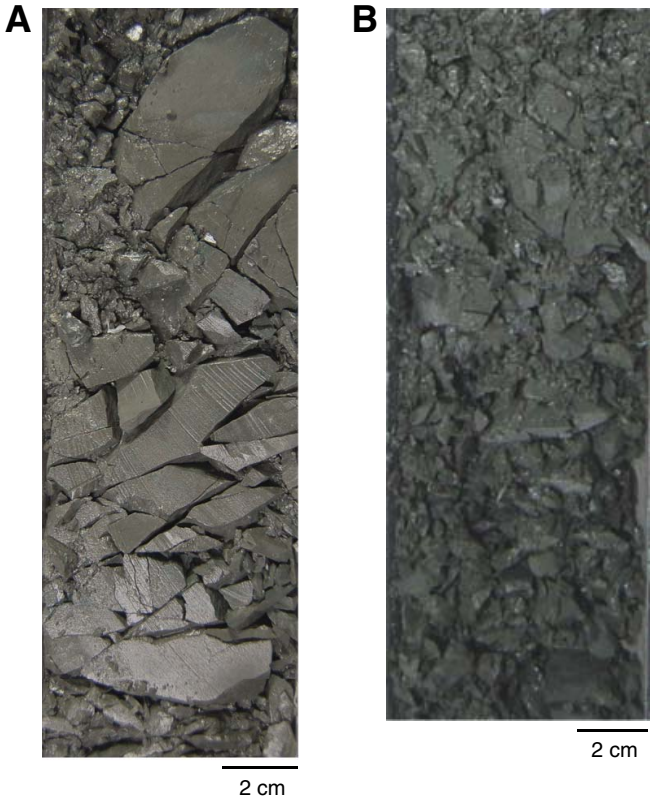

Figure F30. Lower-hemisphere equal-area projections of fracture surfaces. Fracture surfaces (great circles) with striae (dots) and slip vectors (arrows) showing displacement of hanging wall relative to footwall.

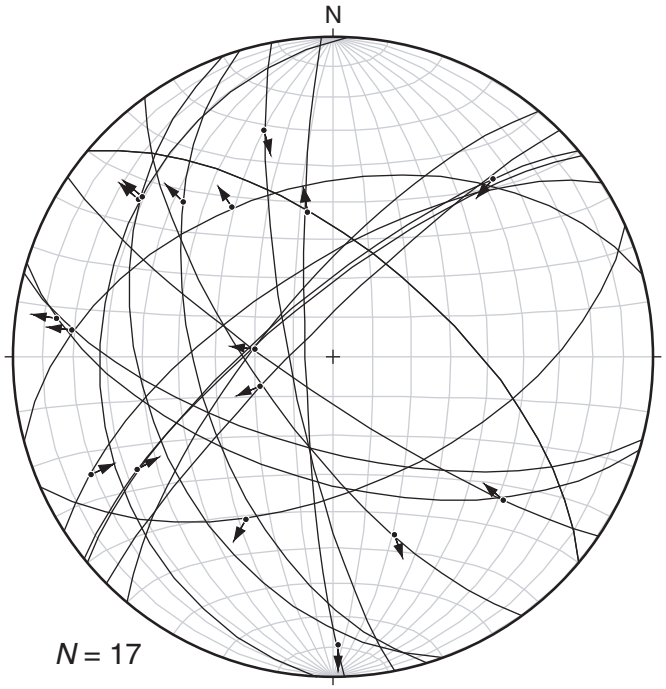

Figure F31. Core photograph of foliated fault gouge in fault Zone 3 (interval 316-C0007D-27R-CC, 6–24 cm).

Figure F32. Appearance of concentrated deformation in lower portion of fault Zone 3. (**A**) CT image and (**B**) core photograph of finely brecciated hemipelagic mudstone (interval 316-C0007D-29R-2, 37–73 cm). **C.** Close up of finely brecciated interval. **D.** Thin (2 mm thick) dark layer (arrow) developed at base of finely brecciated interval.

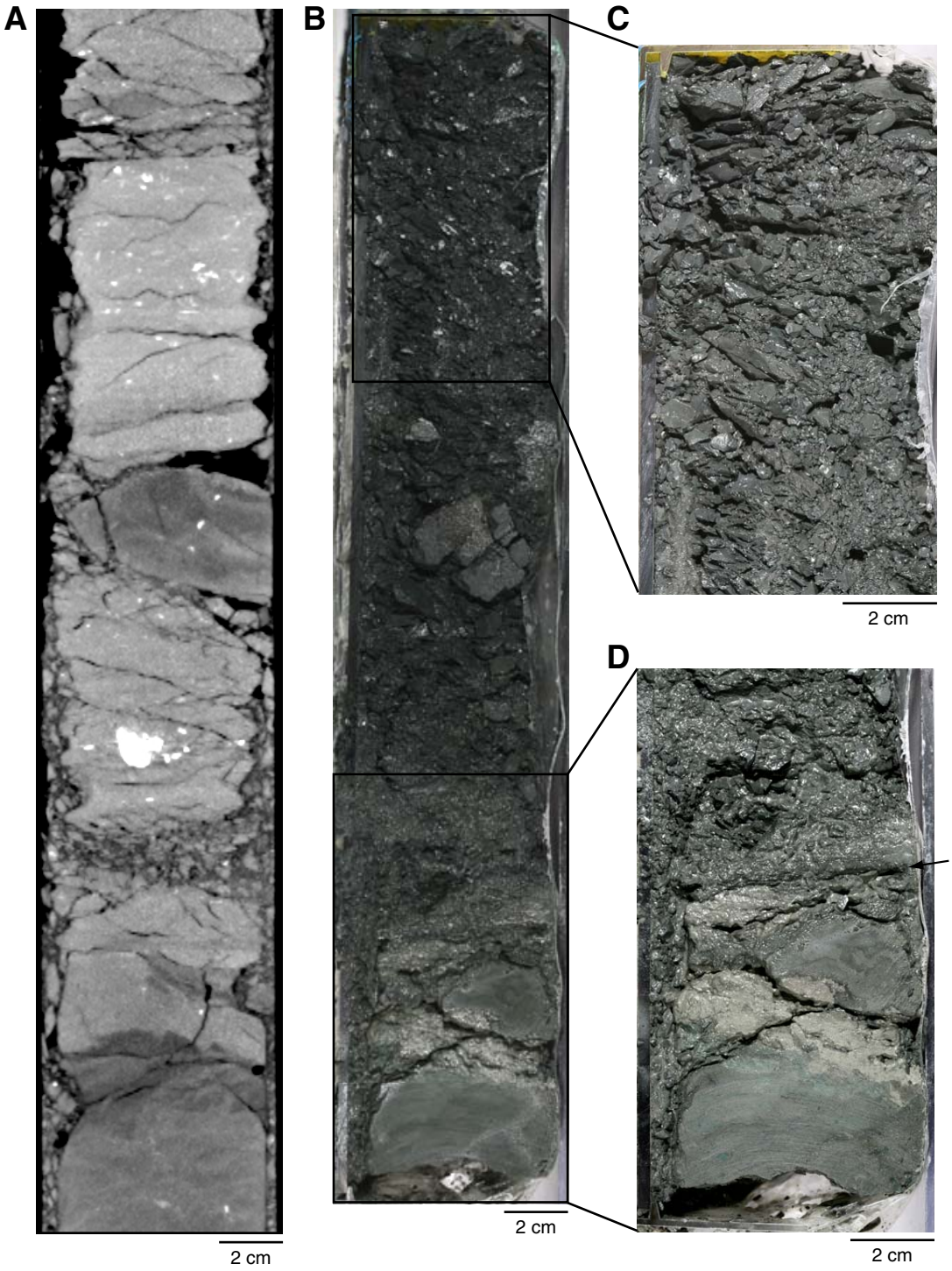

Figure F33. Age and depth based on nannofossil events and magnetostratigraphic data in the same hole. **A.** Hole C0007C. **B.** Hole C0007D. CSF = core depth below seafloor. LO = last occurrence, RE = reentrance. Shaded band = fault zone.

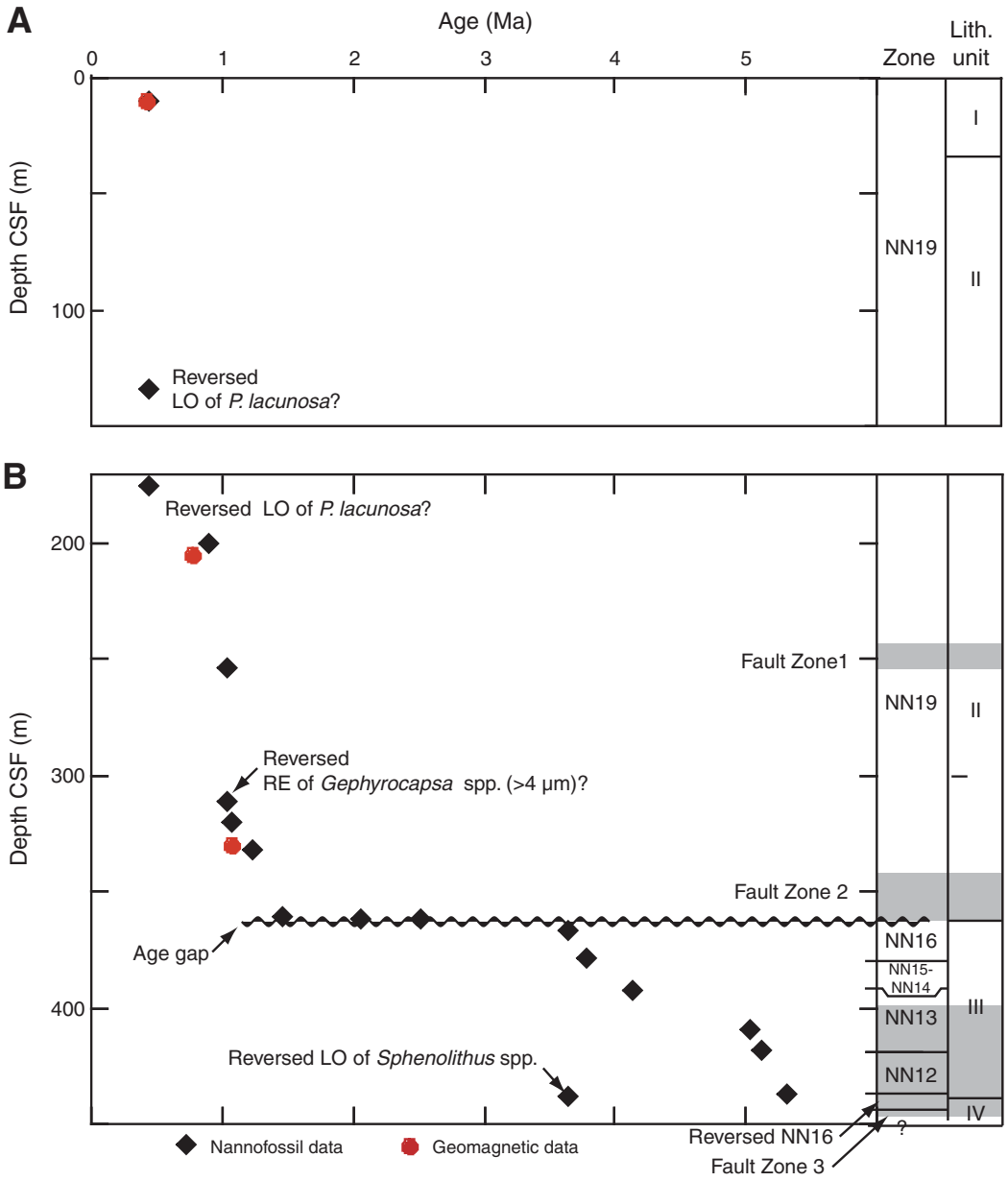

Figure F34. Nannofossil record of age reversal from Zones NN12 to NN16 between 438.24 and 438.61 m CSF in Core 316-C0007D-29R.

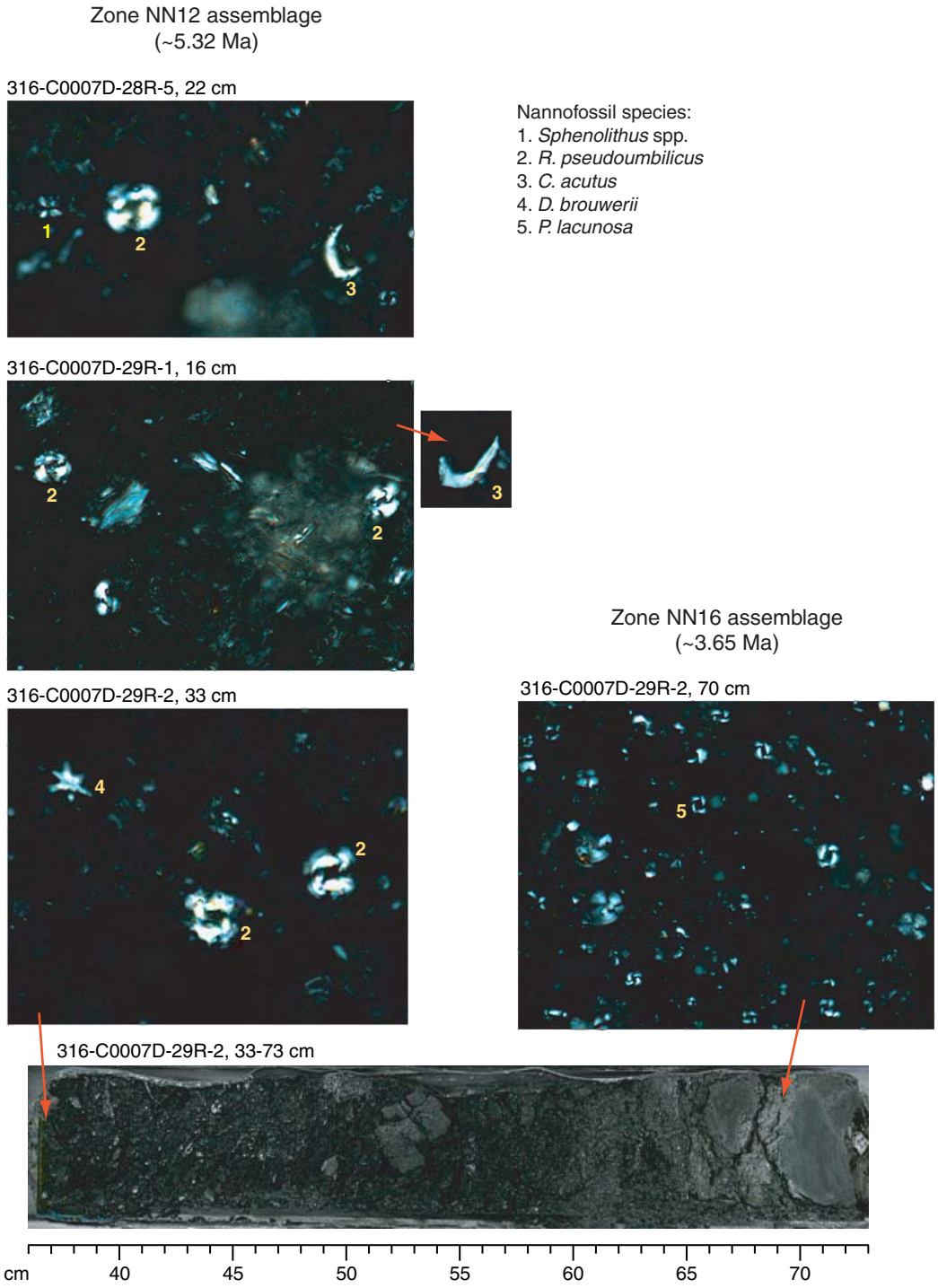

Figure F35. Magnetic susceptibility and remanent magnetization before (green) and after (purple, red, and blue) 40 mT alternating-field (AF) demagnetization. (**A**) Magnetic susceptibility, (**B**) intensity, (**C**) inclination, and (**D**) declination of archive halves, Holes C0007A–C0007C. NRM inclinations are biased toward high positive inclinations, suggesting that drilling-induced magnetization is present. AF demagnetization to 40 mT can effectively remove drilling-induced magnetization, as indicated by changes in inclination and intensity. CSF = core depth below seafloor. Black dots in C = AF or thermal demagnetization data of discrete samples.

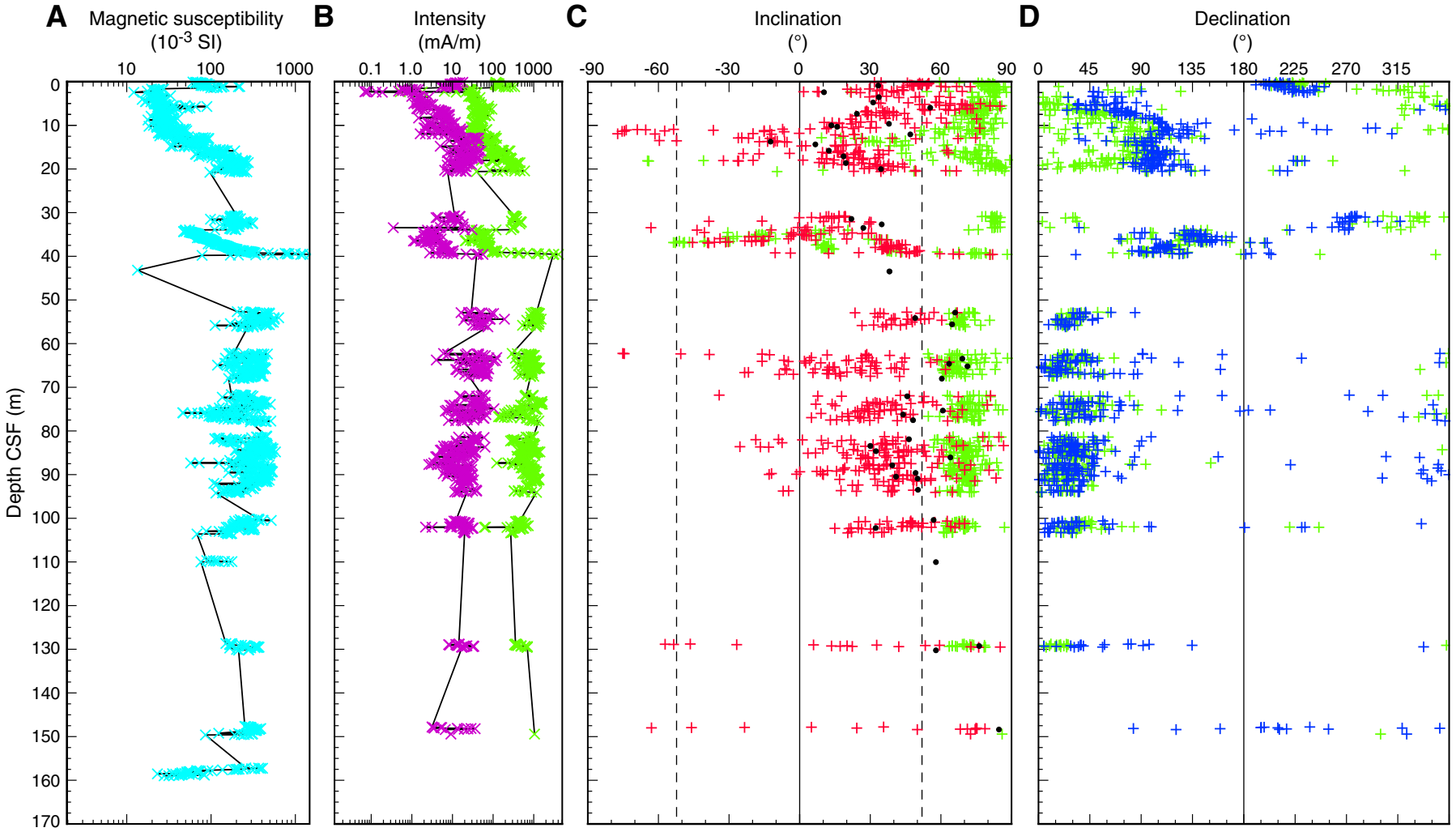

Figure F36. Magnetic susceptibility and remanent magnetization before (green) and after (purple, red, and blue) 40 mT alternating-field (AF) demagnetization. (**A**) Magnetic susceptibility, (**B**) intensity, (**C**) inclination, and (**D**) declination of archive halves, Hole C0007D. NRM inclinations are biased toward high positive inclinations, suggesting that drilling-induced magnetization is present. AF demagnetization to 40 mT can effectively remove drilling-induced magnetization, as indicated by changes in inclination and intensity. CSF = core depth below seafloor. Black dots in C = AF or thermal demagnetization data of discrete samples, black squares in D = thermal demagnetization data of discrete samples.

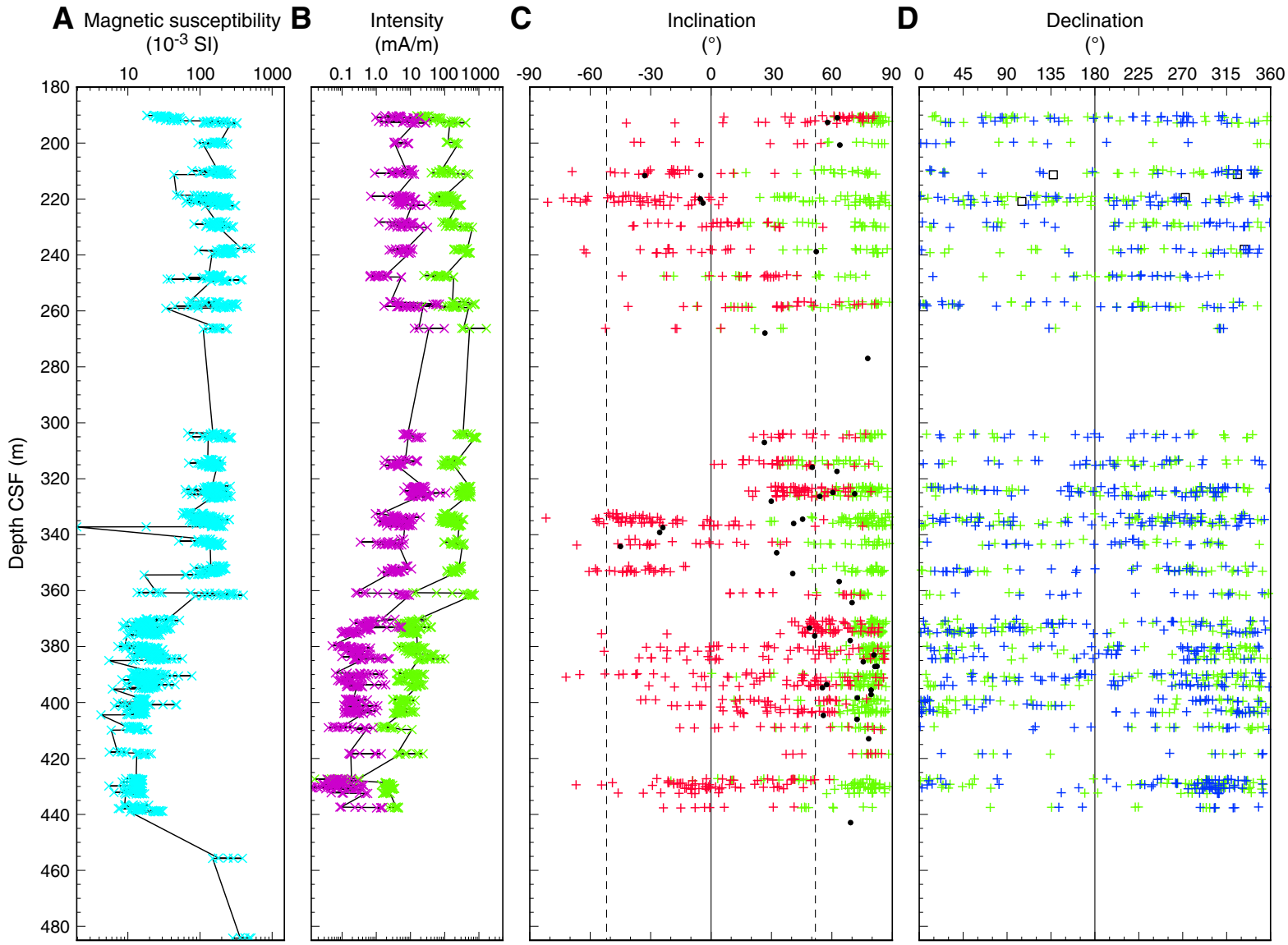

Figure F37. Vector endpoint and stereonet magnetization directions showing the results of (**A**) alternating-field (AF) demagnetization of Sample 316-C0007C-11X-1, 14–16 cm, (**B**) thermal demagnetization of Sample 316-C0007D-5R-CC, 5–7 cm, and (**C**) thermal demagnetization of Sample 316-C0007D-22R-1, 31–33 cm. Black and white squares = projection of magnetization vector endpoint on the horizontal and vertical planes, respectively. NRM = natural remanent magnetization.

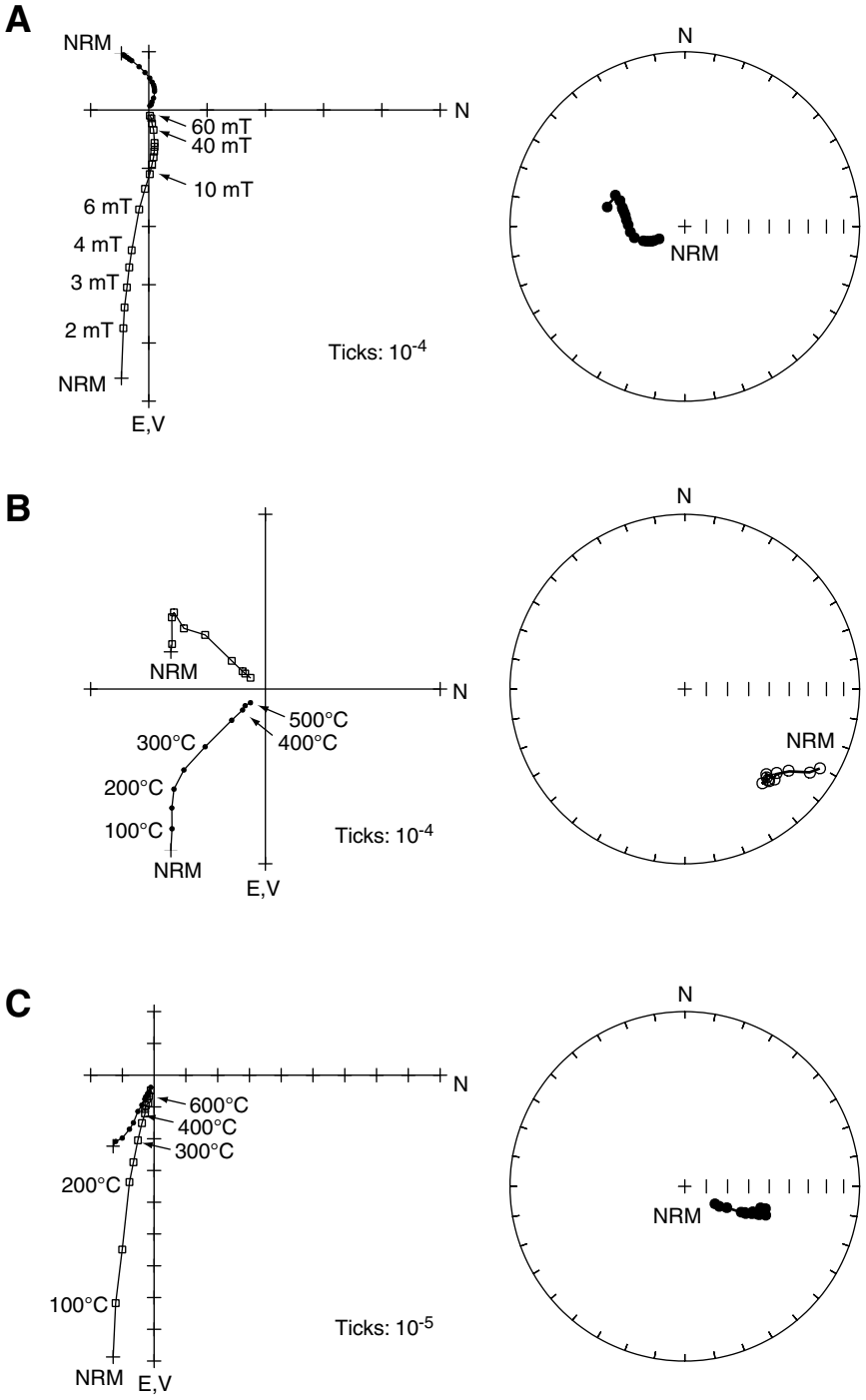

Figure F38. Histogram of inclinations isolated from discrete samples, Site C0007.

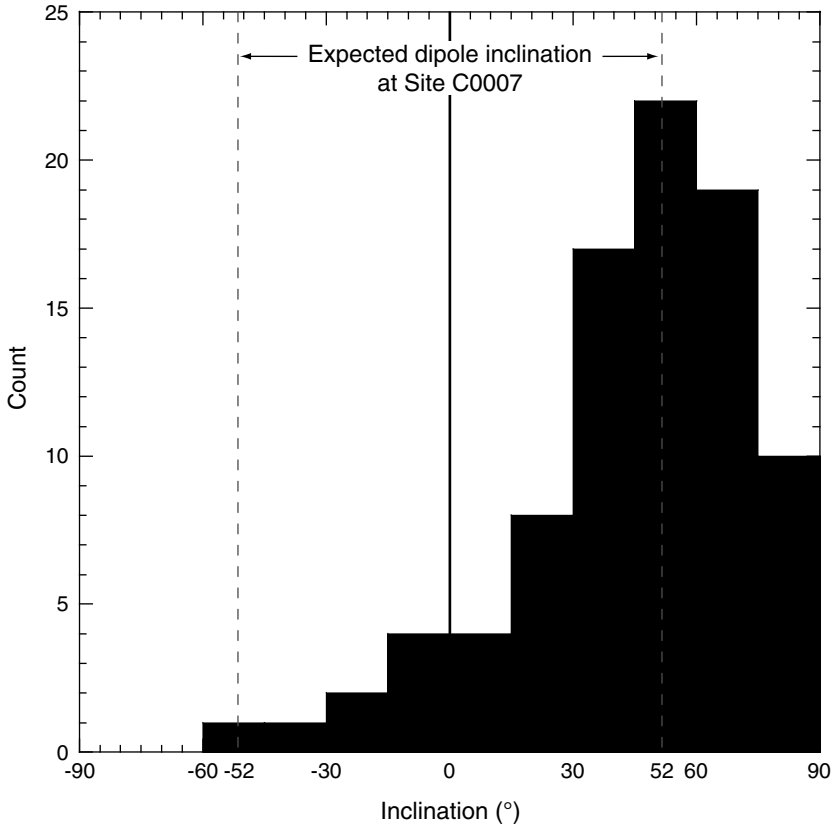

Figure F39. Downhole variation in stable magnetic inclination, inferred polarity, and biostratigraphic zones for sediments, Site C0007. **A.** Holes C0007A–C0007C. **B.** Hole C0007D. CSF = core depth below seafloor. Black areas = normal polarity, white areas = reversed polarity, hatched area = mixed polarity. Arrows = thrust faults observed in core.

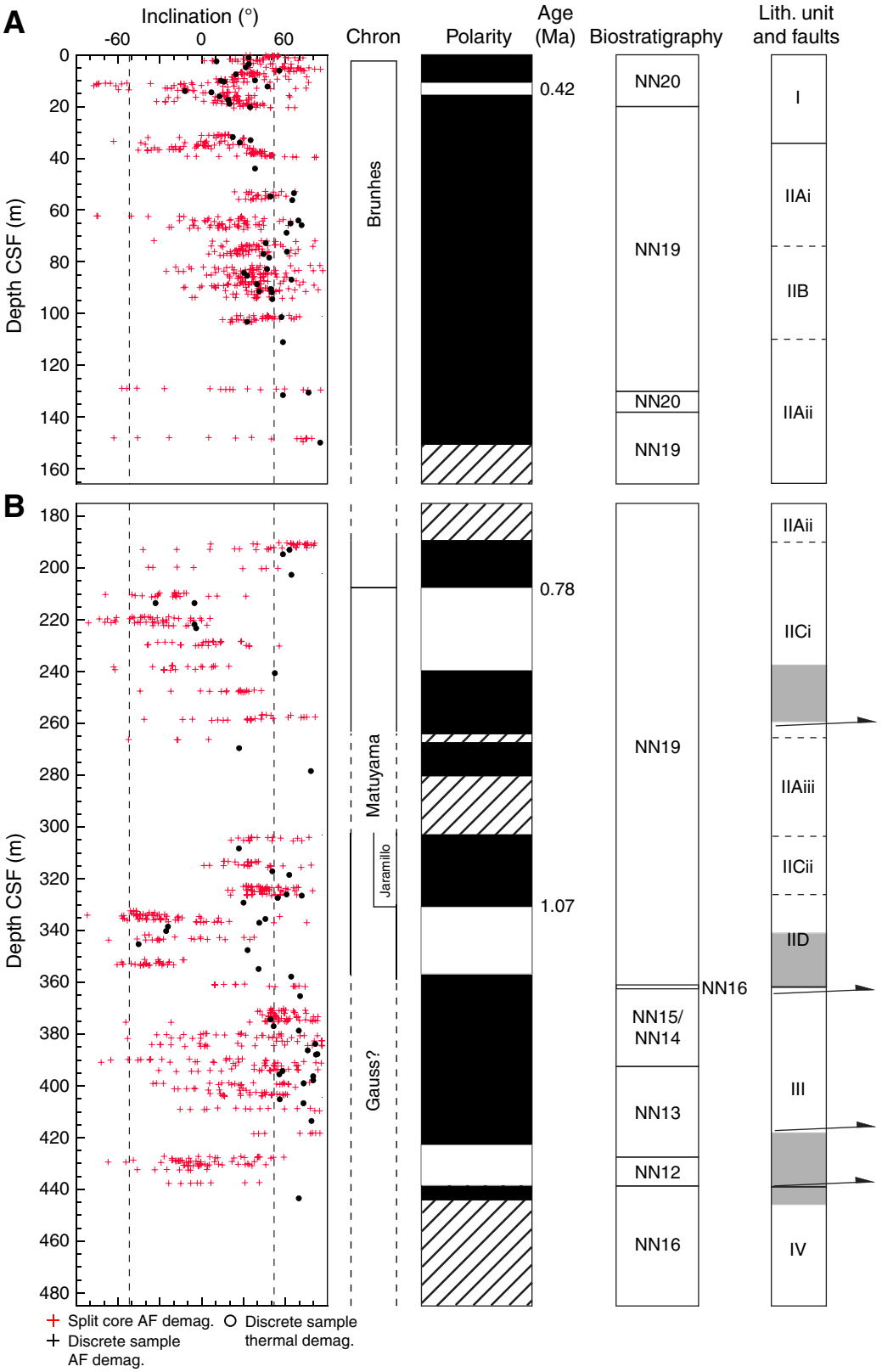

Figure F40. Concentrations of (**A**) salinity, (**B**) chloride, (**C**) sodium, and (**D**) Na/Cl in interstitial water samples, Hole C0007C; and (**E**) salinity, (**F**) chloride, (**G**) sodium, and (**H**) Na/Cl in interstitial water samples, Hole C0007D. Salinity is calculated from refractive index, and sodium by charge balance. CSF = core depth below seafloor. SW = seawater values.

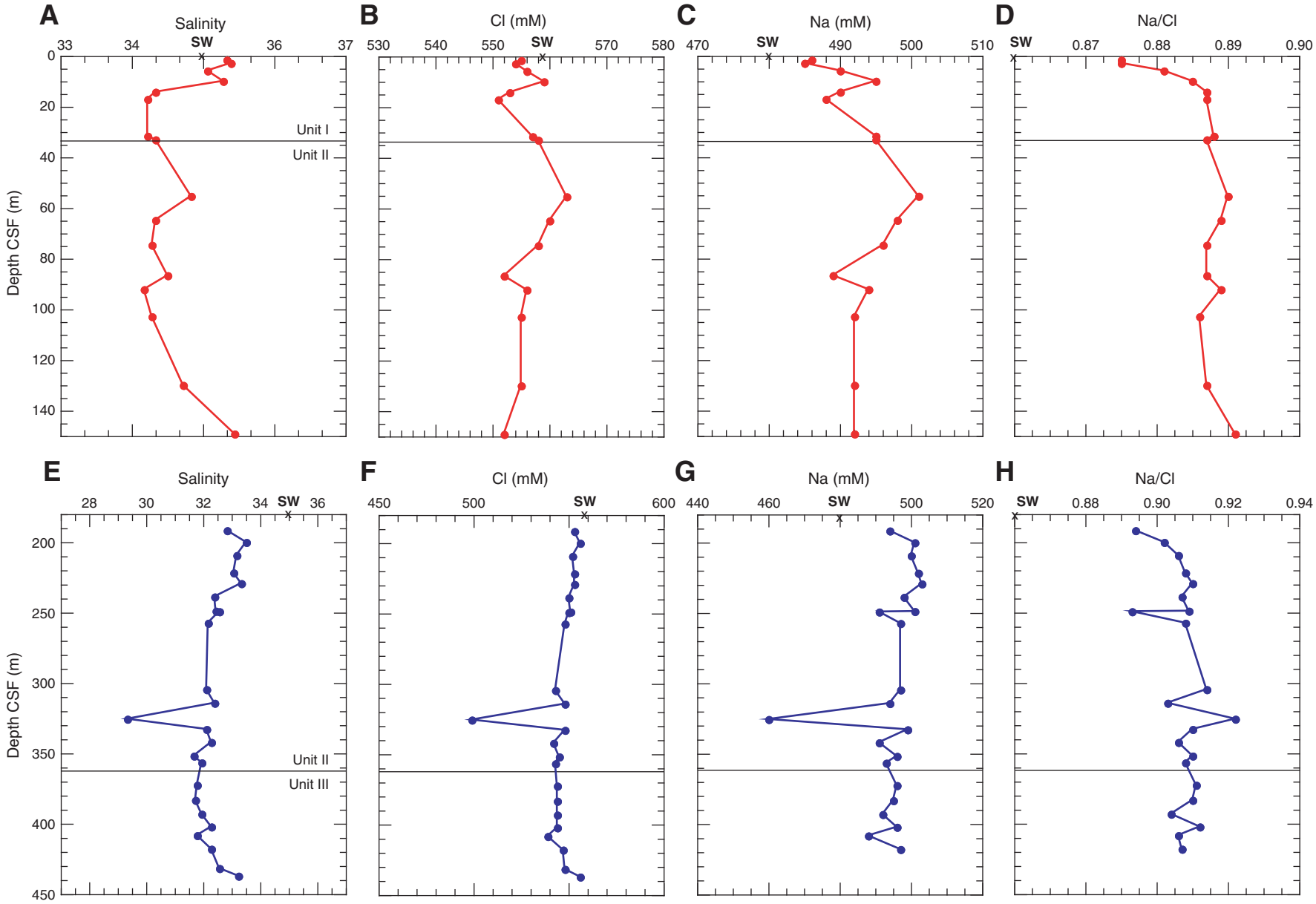

Figure F41. Concentrations of (**A**) pH, (**B**) sulfate, (**C**) alkalinity, and (**D**) barium, Hole C0007C; and (**E**) pH, (**F**) sulfate, (**G**) alkalinity, and (**H**) barium, Hole C0007D. SW = seawater values.

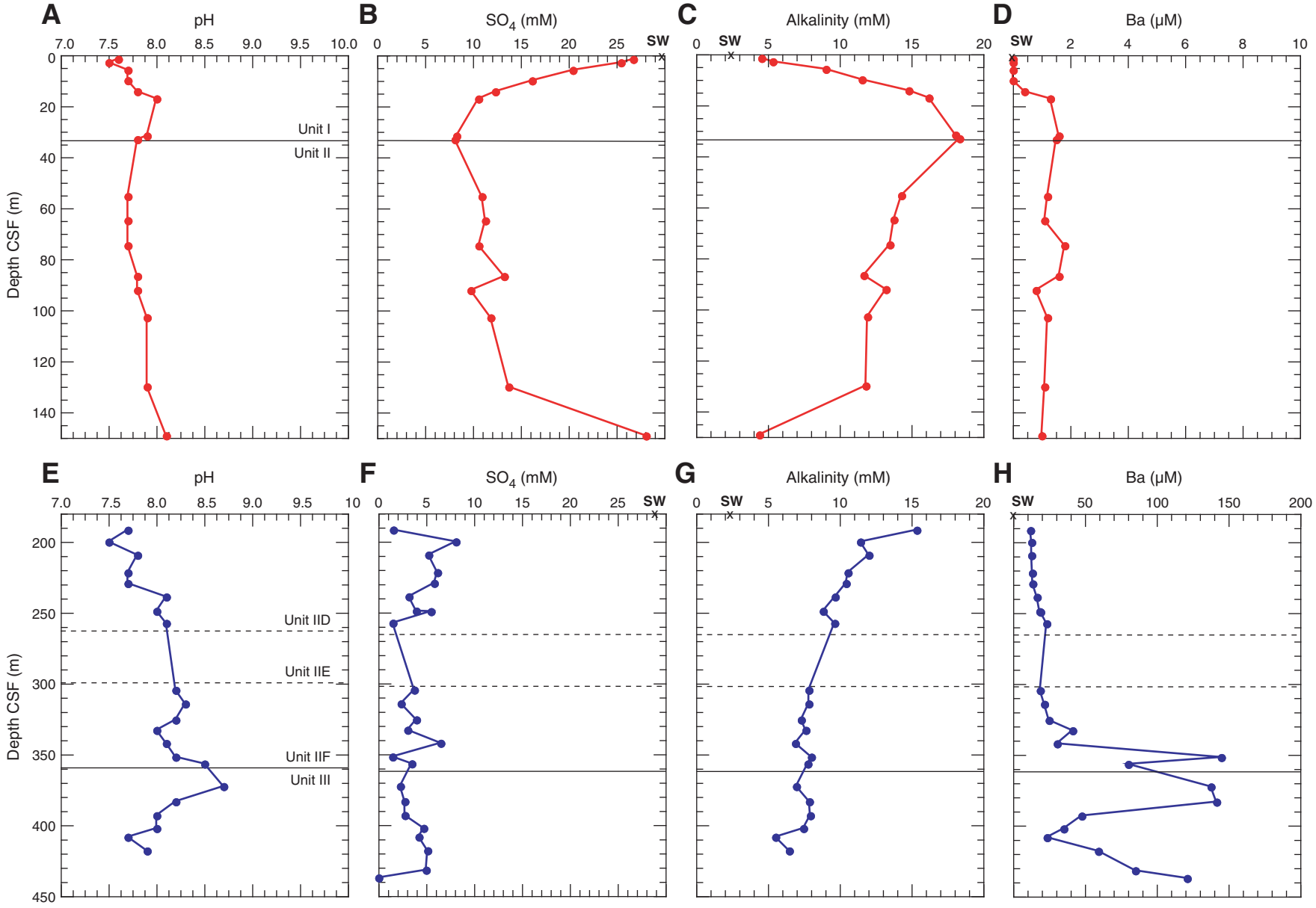

Figure F42. Concentrations of (**A**) ammonium, (**B**) phosphate, and (**C**) bromide from interstitial water samples, Hole C0007C; and (**D**) ammonium, (**E**) phosphate, and (**F**) bromide from interstitial water samples, Hole C0007D. CSF = core depth below seafloor. SW = seawater values.

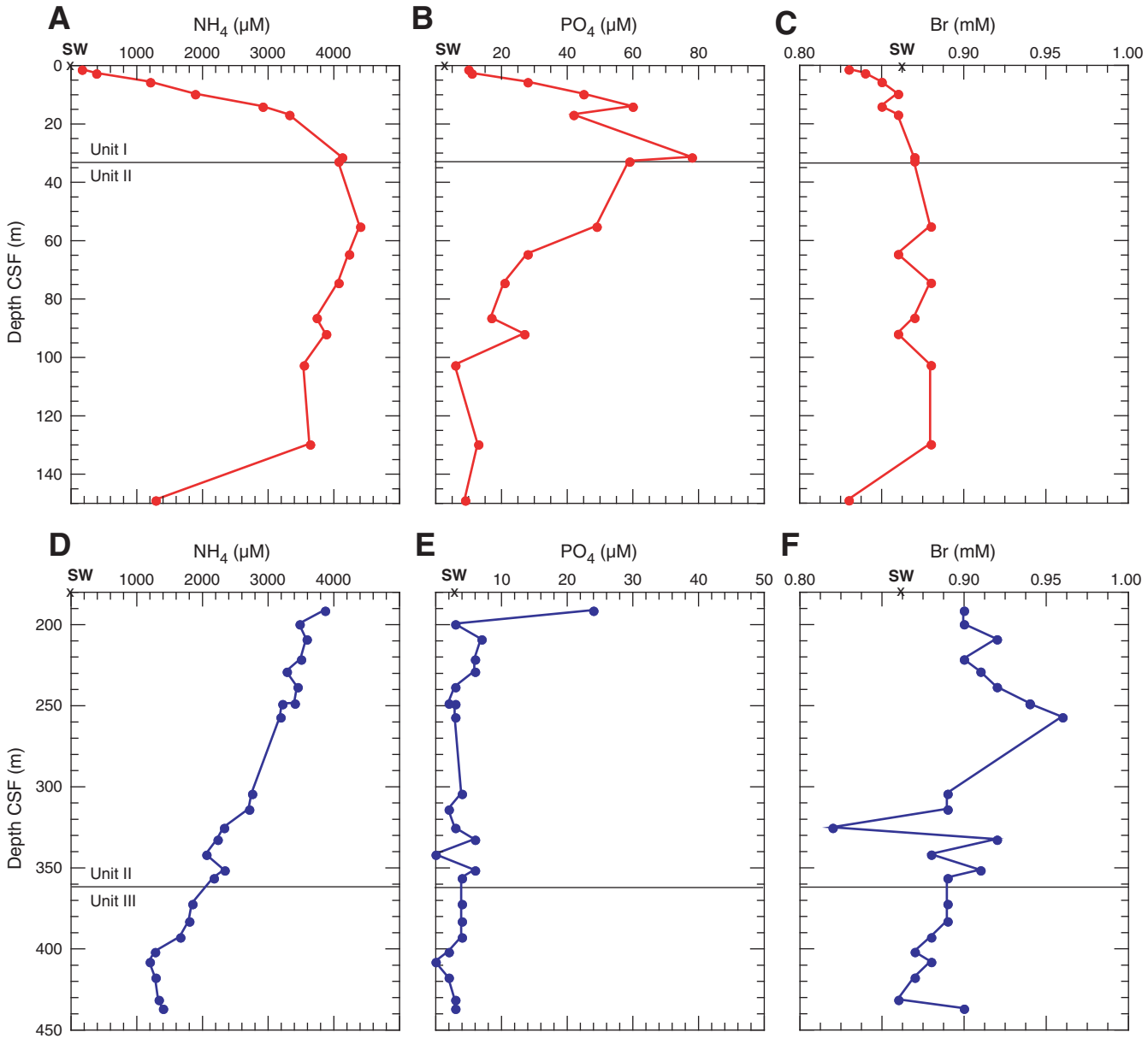

Figure F43. Concentrations of (**A**) calcium, (**B**) magnesium, (**C**) potassium, and (**D**) silica in interstitial waters, Hole C0007C; and (**E**) calcium, (**F**) magnesium, (**G**) potassium, and (**H**) silica in interstitial waters, Hole C0007D. CSF = core depth below seafloor. SW = seawater values. (**Continued on next page.**)

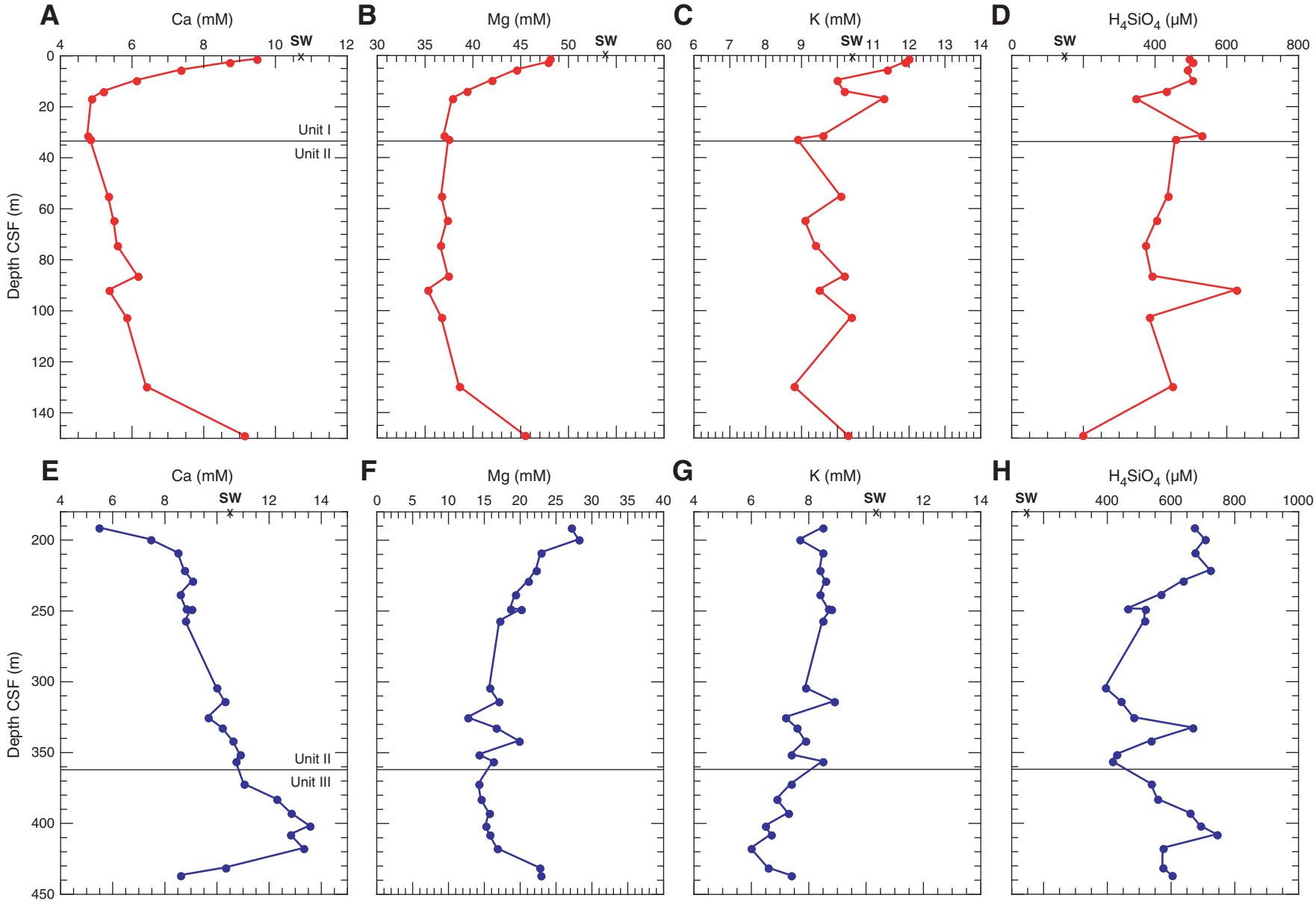

Figure F43 (continued). Concentrations of (**I**) rubidium and (**J**) cesium in interstitial waters, Hole C0007C; and (**K**) rubidium and (**L**) cesium in interstitial waters, Hole C0007D.

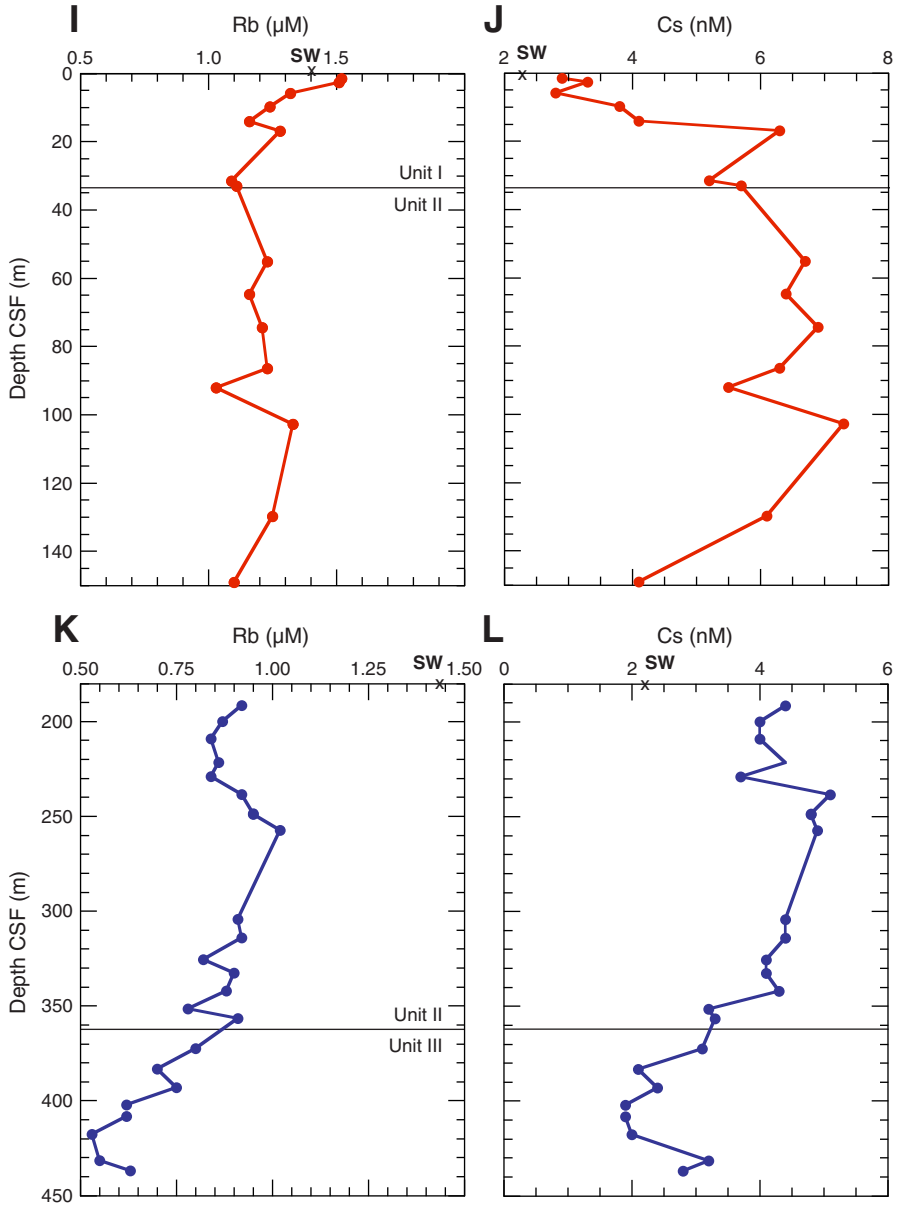

Figure F44. Concentrations of (**A**) lithium, (**B**) boron, and (**C**) strontium from interstitial waters, Hole C0007C; and (**D**) lithium, (**E**) boron, and (**F**) strontium from interstitial waters, Hole C0007D. CSF = core depth below seafloor. SW = seawater values. (**Continued on next page.**)

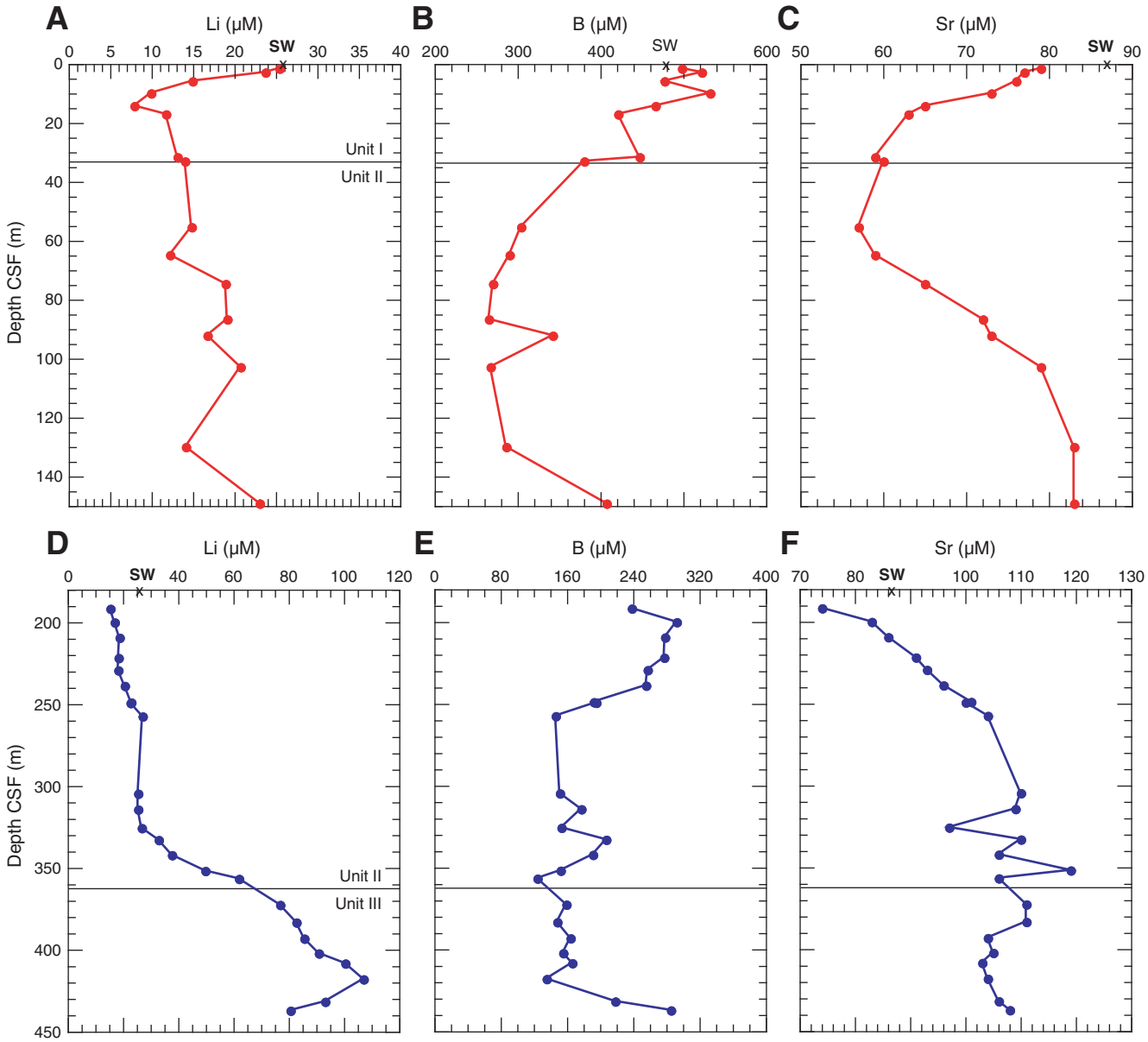

Figure F44 (continued). Concentrations of (**G**) manganese, (**H**) iron, and (**I**) molybdenum from interstitial waters, Hole C0007C; and (**J**) manganese, (**K**) iron, and (**L**) molybdenum from interstitial waters, Hole C0007D.

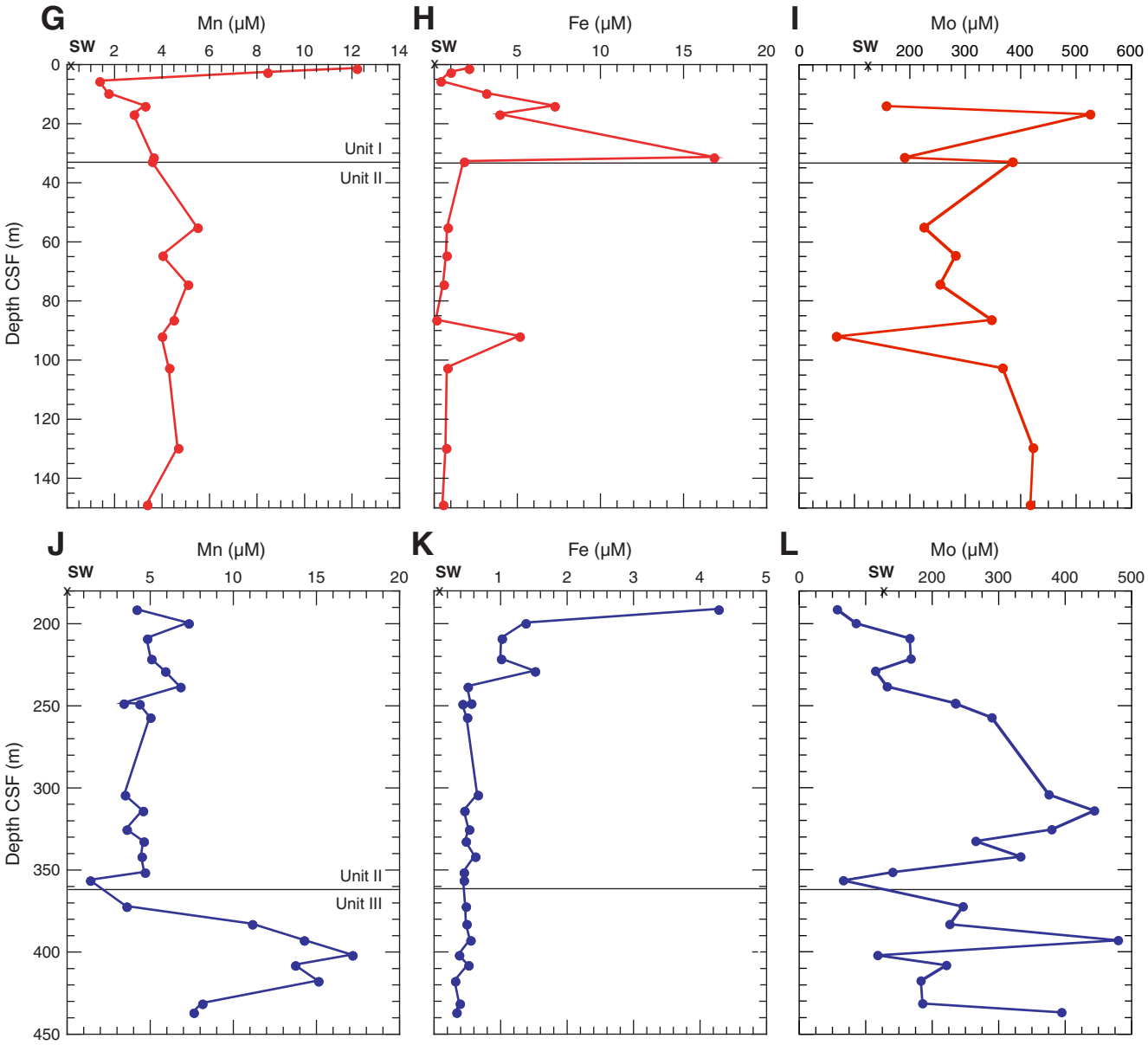

Figure F45. Concentrations of (**A**) copper, (**B**) zinc, and (**C**) vanadium in interstitial waters, Hole C0007C; and (**D**) copper, (**E**) zinc, and (**F**) vanadium in interstitial waters, Hole C0007D. CSF = core depth below seafloor. SW = seawater values. (**Continued on next page.**)

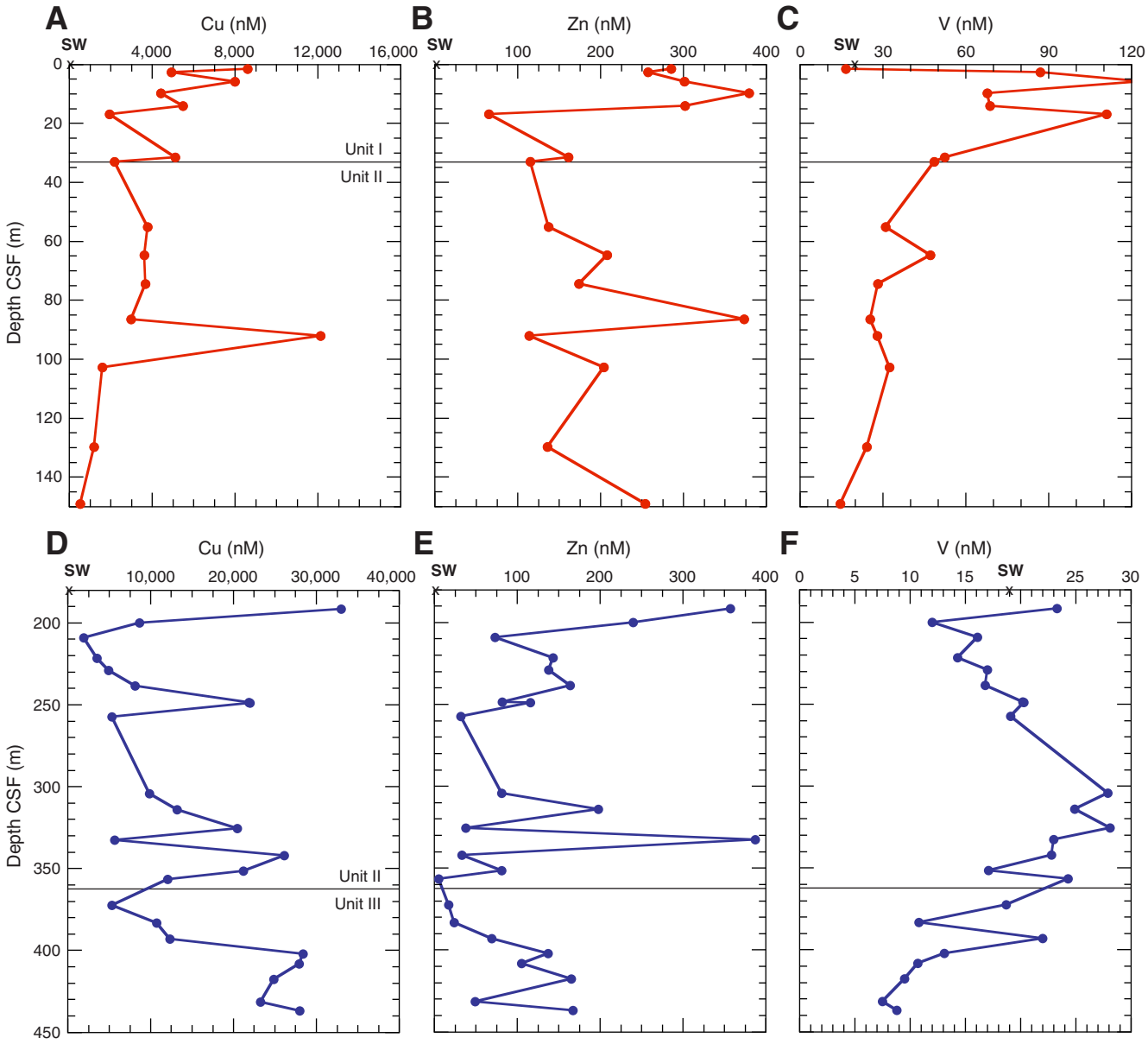

Figure F45 (continued). Concentrations of (**G**) lead, (**H**) uranium, and (**I**) yttrium in interstitial waters, Hole C0007C; and (**J**) lead, (**K**) uranium, and (**L**) yttrium in interstitial waters, Hole C0007D.

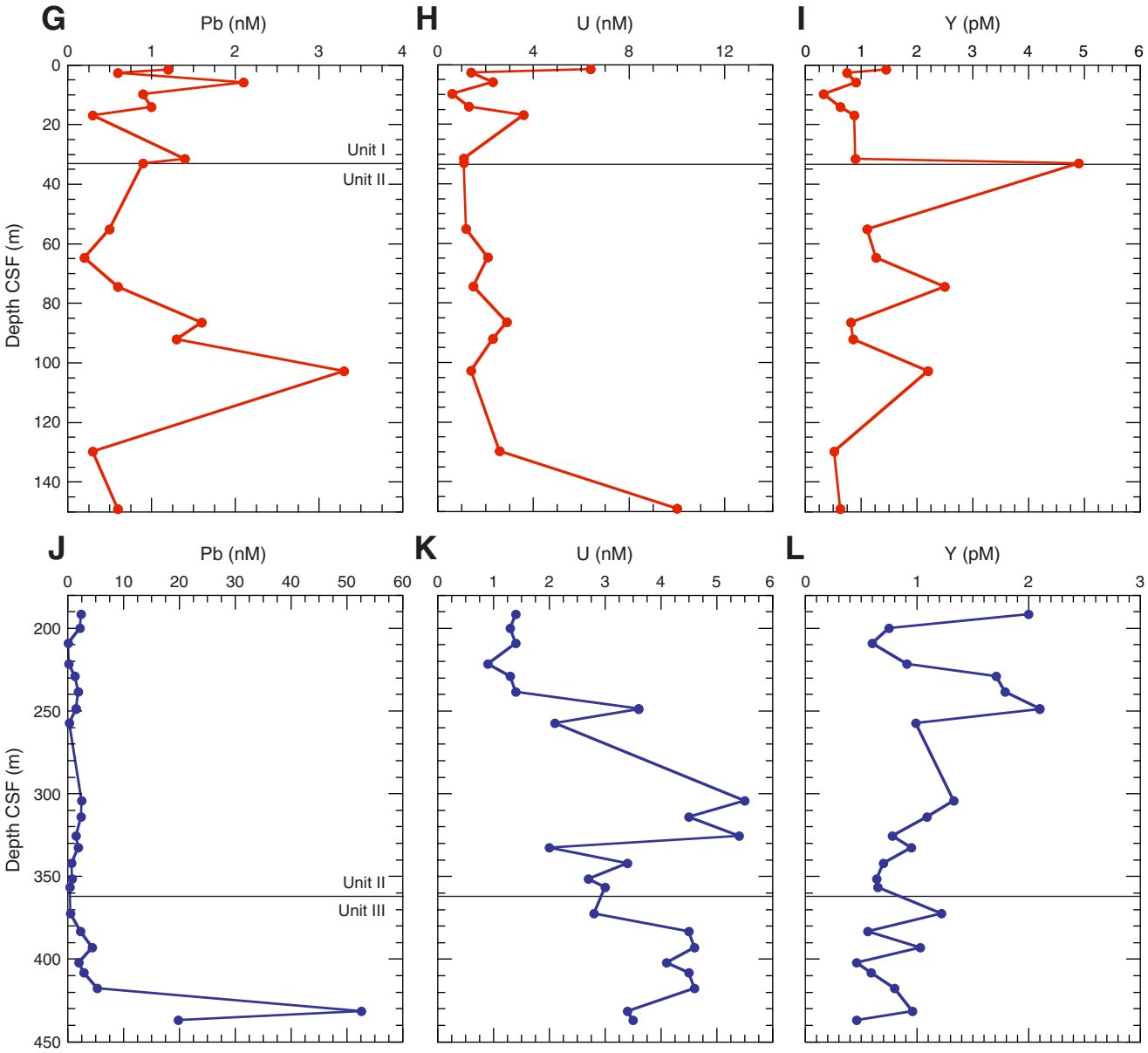

Figure F46. Pore fluid $\delta^{18}O$ isotopic ratios, Site C0007. CSF = core depth below seafloor. SW = seawater value.

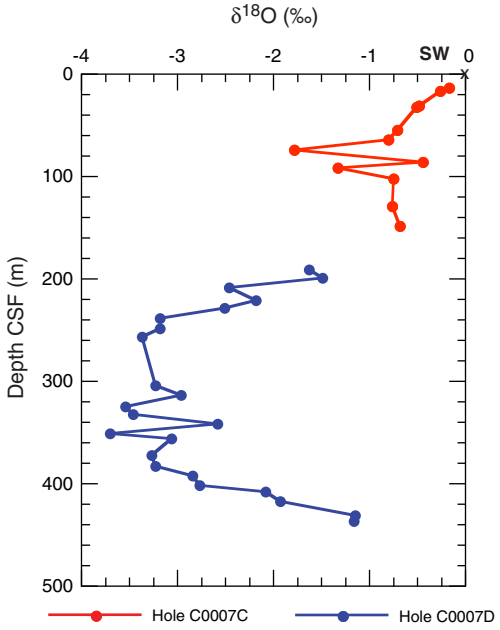

Figure F47. Dissolved methane and ethane concentrations calculated from headspace samples (see Table T16) and values of methane ethane ratio (C_1/C_2) in sediments, Site C0007. Note the different concentration scales for methane. CSF = core depth below seafloor.

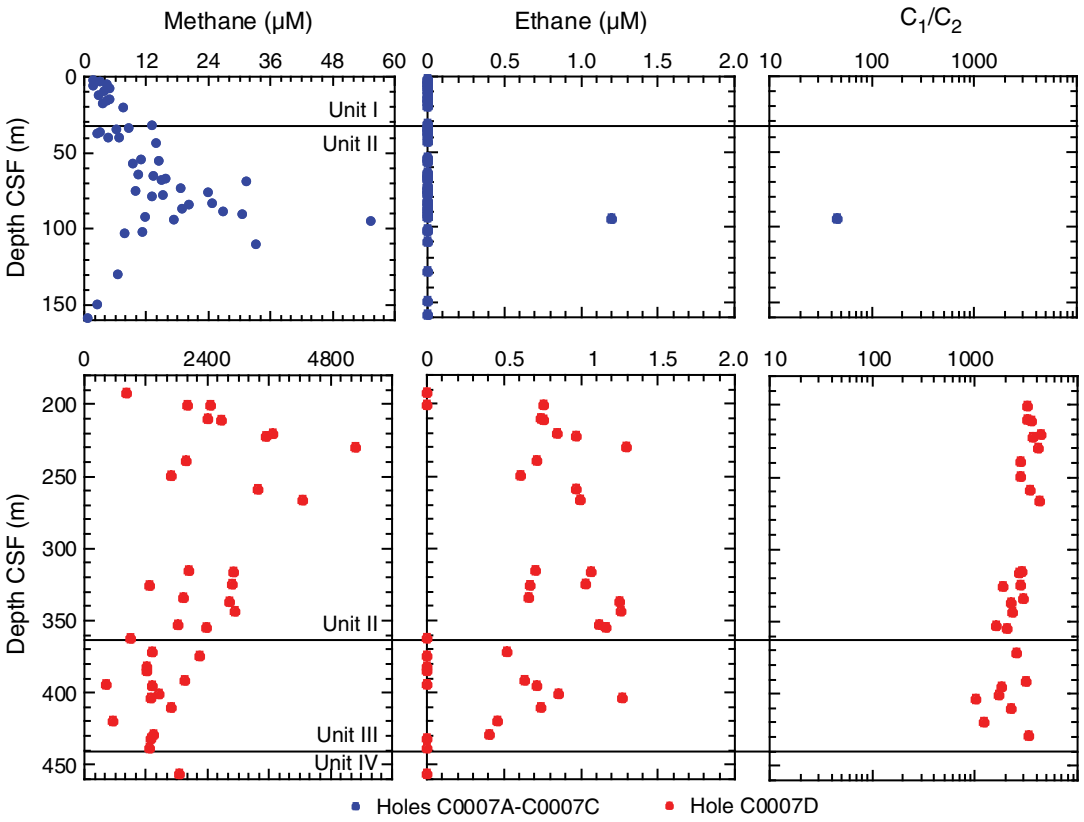

Figure F48. Calcium carbonate ($CaCO_3$), total organic carbon (TOC), total nitrogen (TN), carbon to nitrogen (C/N) ratio, and total sulfur (TS) in sediments, Site C0007. CSF = core depth below seafloor.

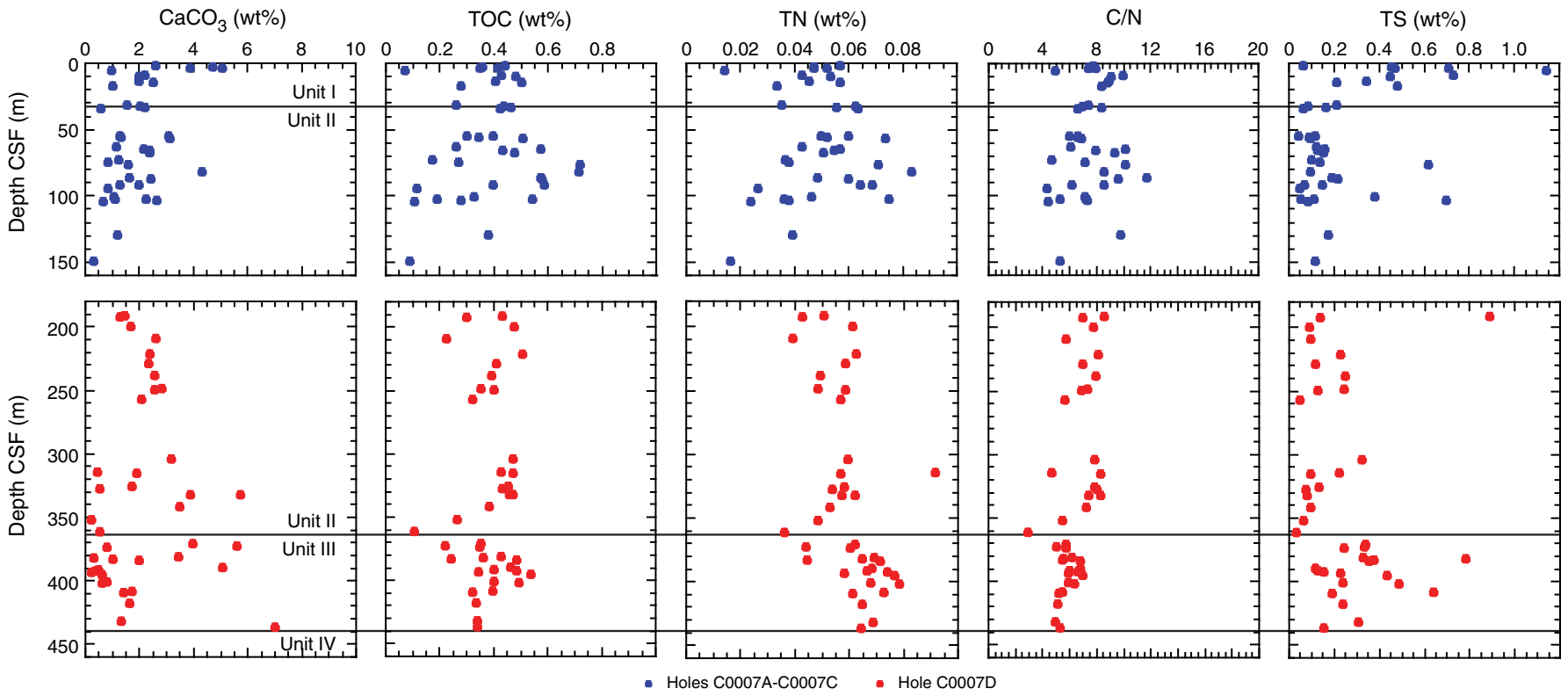

Figure F49. Microbial cell abundance enumerated by microscopic direct count of SYBR Green I–stained cells, Site C0007. CSF = core depth below seafloor.

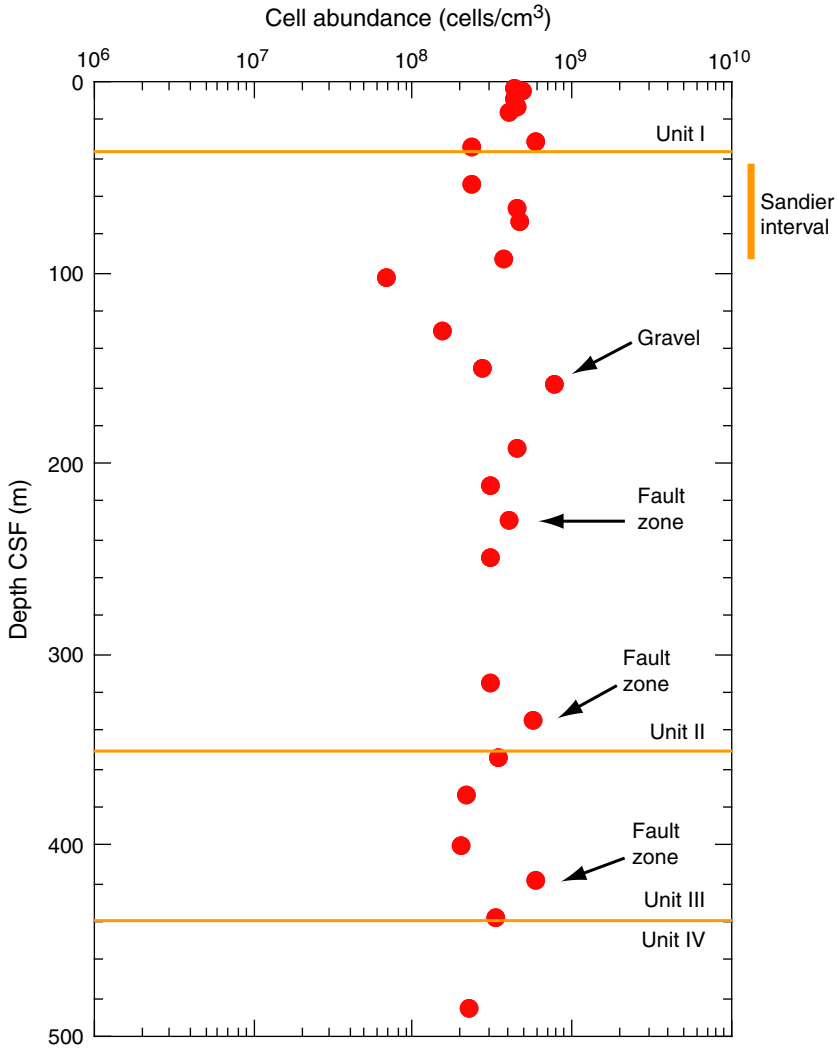

Figure F50. Fluorescent microscopic image of SYBR Green I–stained cells detected from the gravel layer (Sample 316-C0007D-17H-1, 157.7 m CSF).

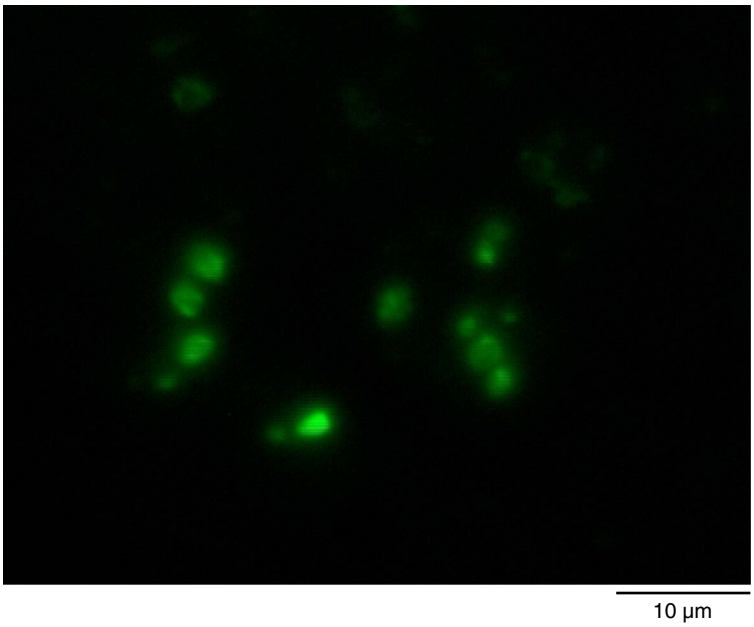

Figure F51. Density and porosity measurement results. **A.** Gamma ray attenuation (GRA) density using a multisensor core logger (MSCL) system on whole-round core sections (gray) and wet bulk density of discrete samples using MAD methods (red), Holes C0007A–C0007C. **B.** Grain density of discrete samples using MAD methods, Holes C0007A–C0007C. **C.** MSCL (gray) and MAD (red) porosity, Holes C0007A–C0007C. **D.** GRA density using a MSCL system on whole-round core sections (gray) and wet bulk density of discrete samples using MAD methods (red), Hole C0007D. **E.** Grain density of discrete samples using MAD methods, Hole C0007D. **F.** MSCL (gray) and MAD (red) porosity, Hole C0007D. CSF = core depth below seafloor.

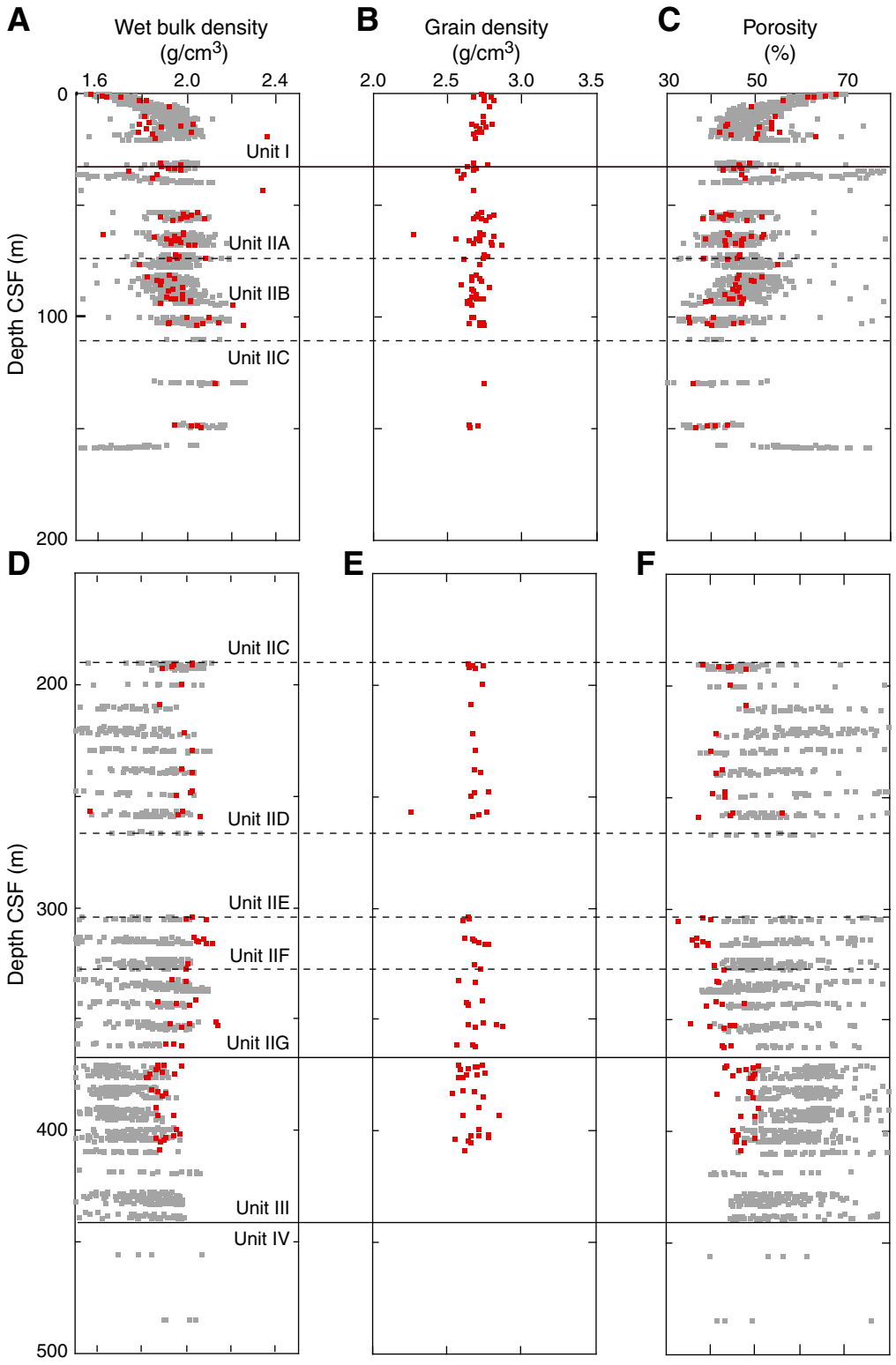

Figure F52. Measurements on discrete samples. **A.** *P*-wave velocity. Black crosses = individual measurements, black squares = measurements along core axis, red squares = average velocity per sample. **B.** *P*-wave velocity anisotropy. For transverse anisotropy, positive values equal lower magnitude along the core axis. **C.** Electrical conductivity. **D.** Electrical conductivity anisotropy. CSF = core depth below seafloor.

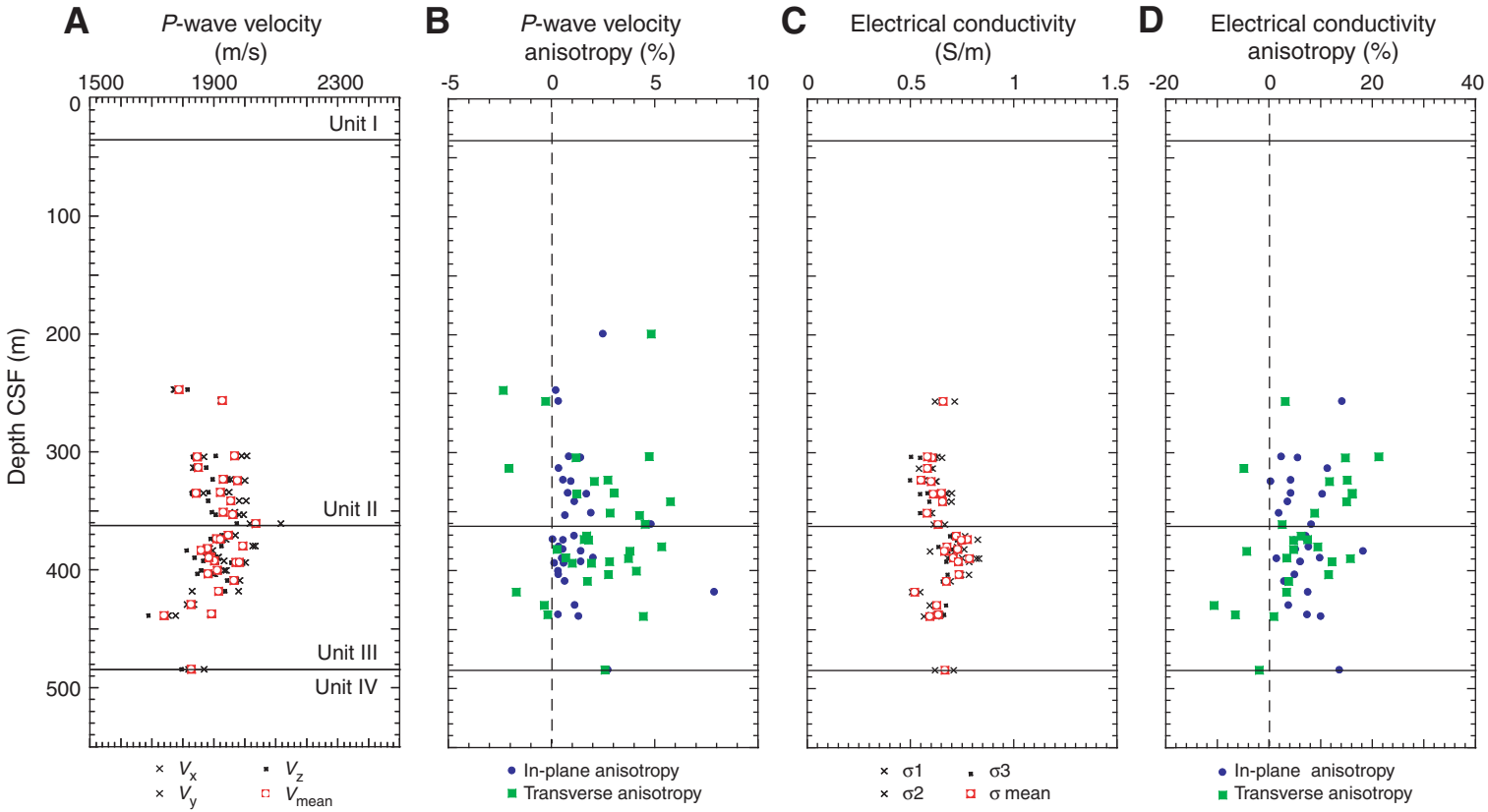

Figure F53. Thermal data. **A.** Thermal conductivity, Holes C0007A, C0007B, and C0007C. **B.** Thermal conductivity, Hole C0007D. **C.** Equilibrium temperatures (circles) and projected temperatures (line). The best-fit linear gradient to the equilibrium temperature is 42°C/km. **D.** Temperature as a function of thermal resistance. The best-fit slope gives a heat flow value of 53 mW/m^2 and a bottom water temperature of 2.0°C. CSF = core depth below seafloor.

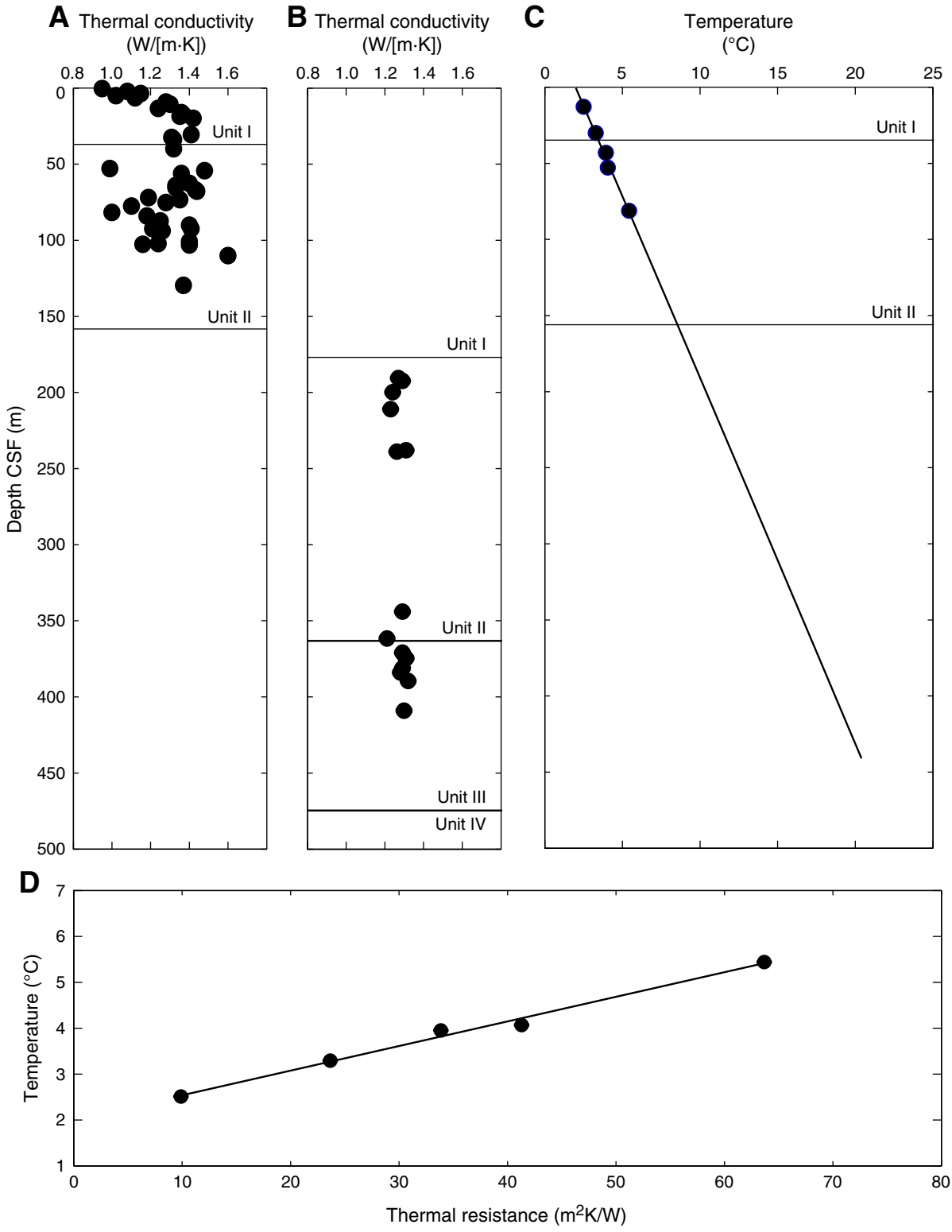

Figure F54. Temperature time series, Site C0007 (blue line). APCT3 measurements at (**A**) 12.6 m CSF, (**B**) 30.1 m CSF, and (**C**) 43.1 m CSF. Unshaded area = data used for equilibrium temperature fit, red line = theoretical equilibrium curve, triangle = shows beginning of fit, inverted triangle = end of fit, dashed red line with circles = estimate of equilibrium temperature. Note frictional heating at penetration (dashed vertical line) and at pull out. (**Continued on next page.**)

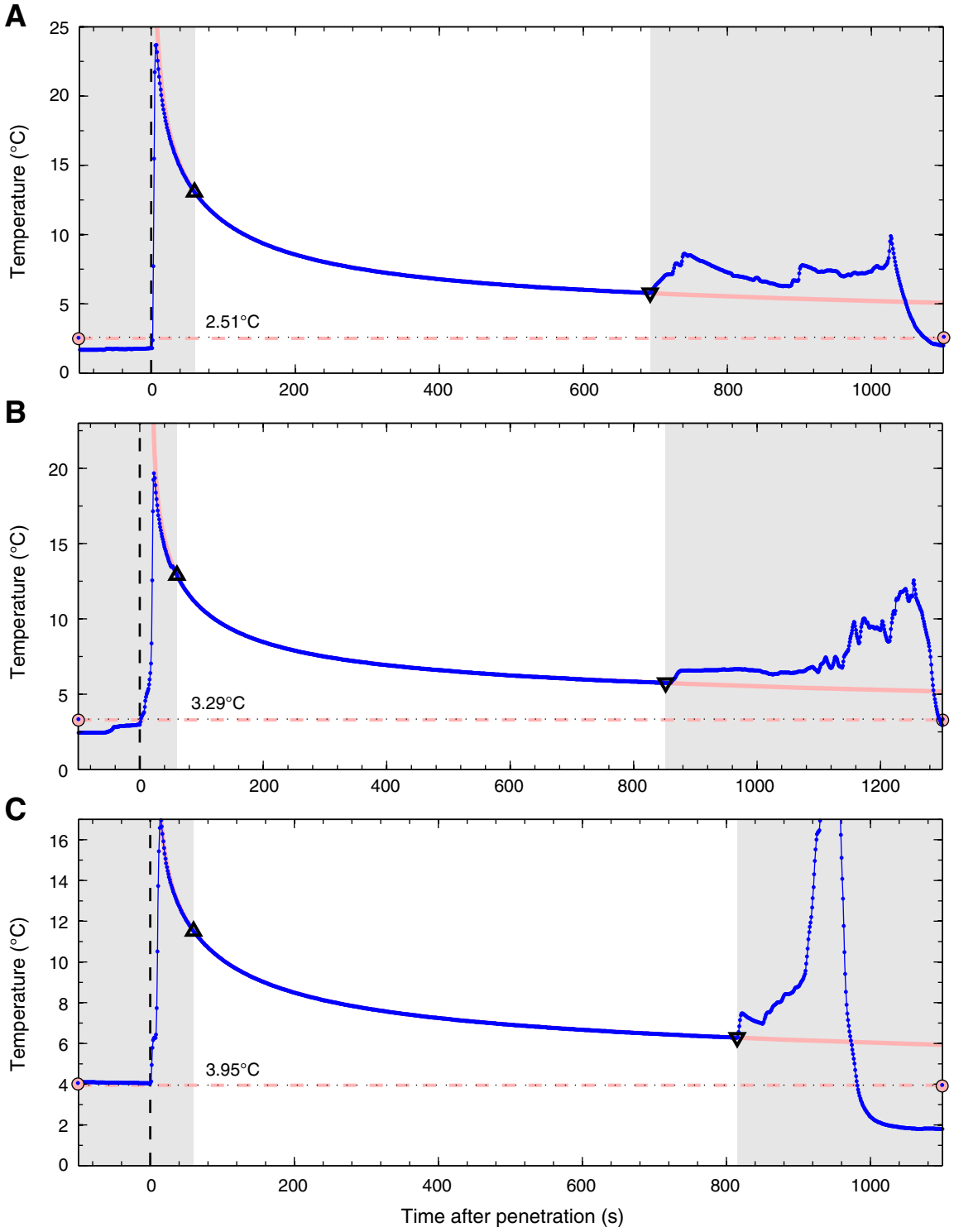

Figure F54 (continued). SET measurements at (**D**) 52.6 m CSF and (**E**) 81.1 m CSF.

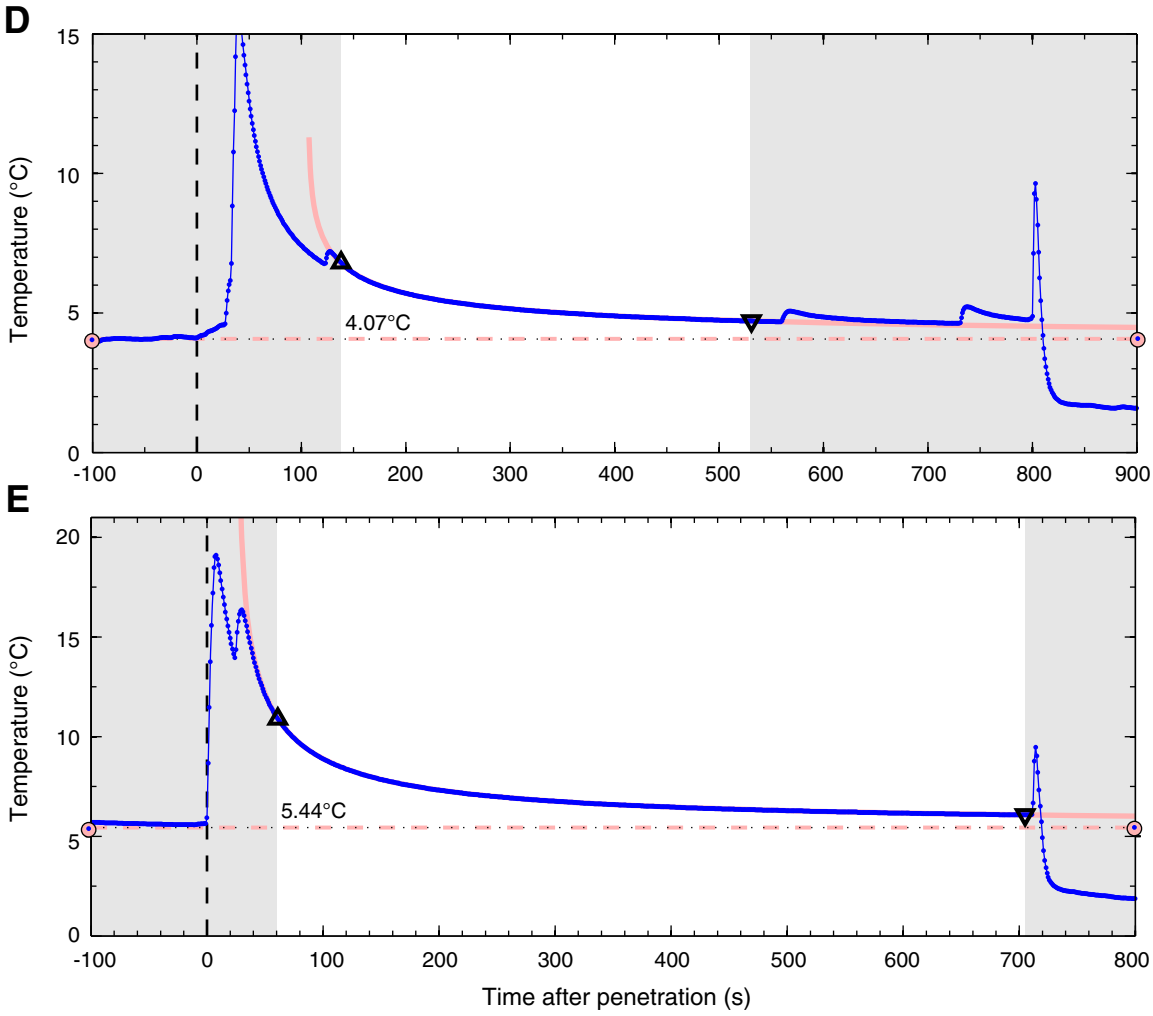

Figure F55. Shear strength measurements, Site C0007. Penetrometer measurements are consistently higher than those measured with the vane shear apparatus. CSF = core depth below seafloor.

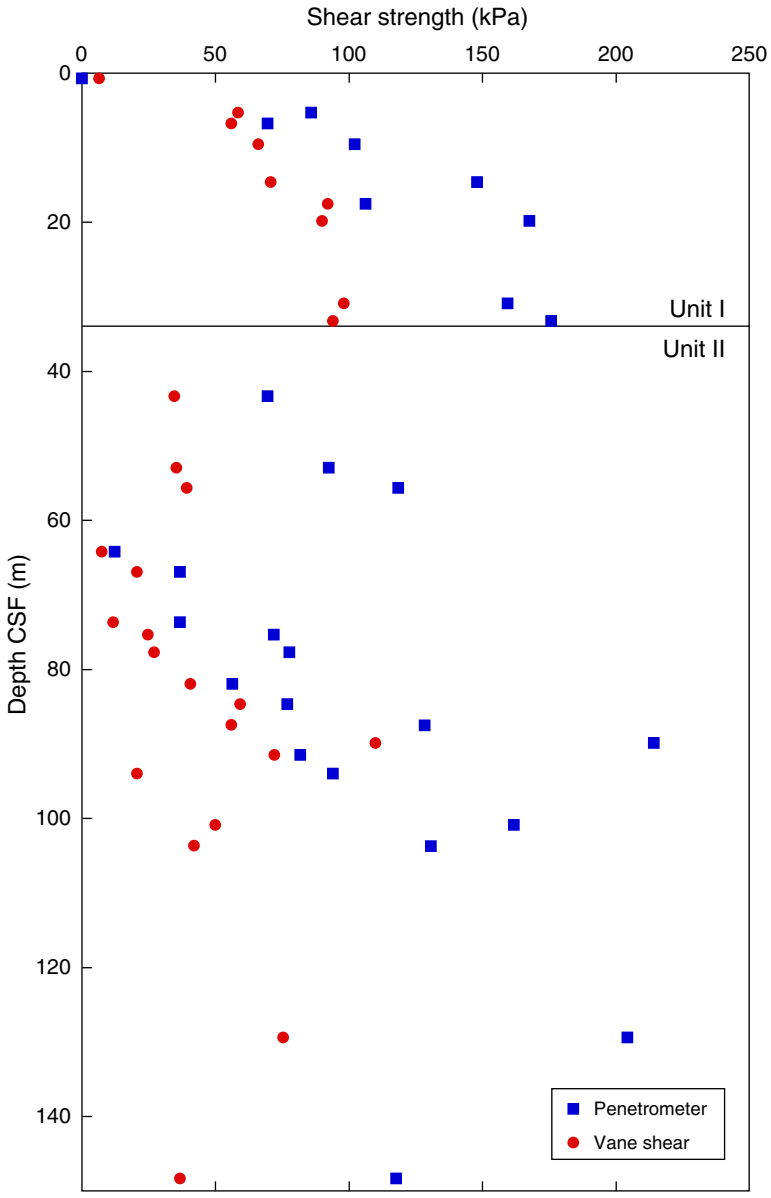

Figure F56. L*, a*, and b* values with depth. L* values at (**A**) Holes C0007A, C0007B, and C0007C and (**B**) Hole C0007D. a* values at (**C**) Holes C0007A, C0007B, and C0007C and (**D**) Hole C0007D. b* values at (**E**) Holes C0007A, C0007B, and C0007C and (**F**) Hole C0007D. CSF = core depth below seafloor.

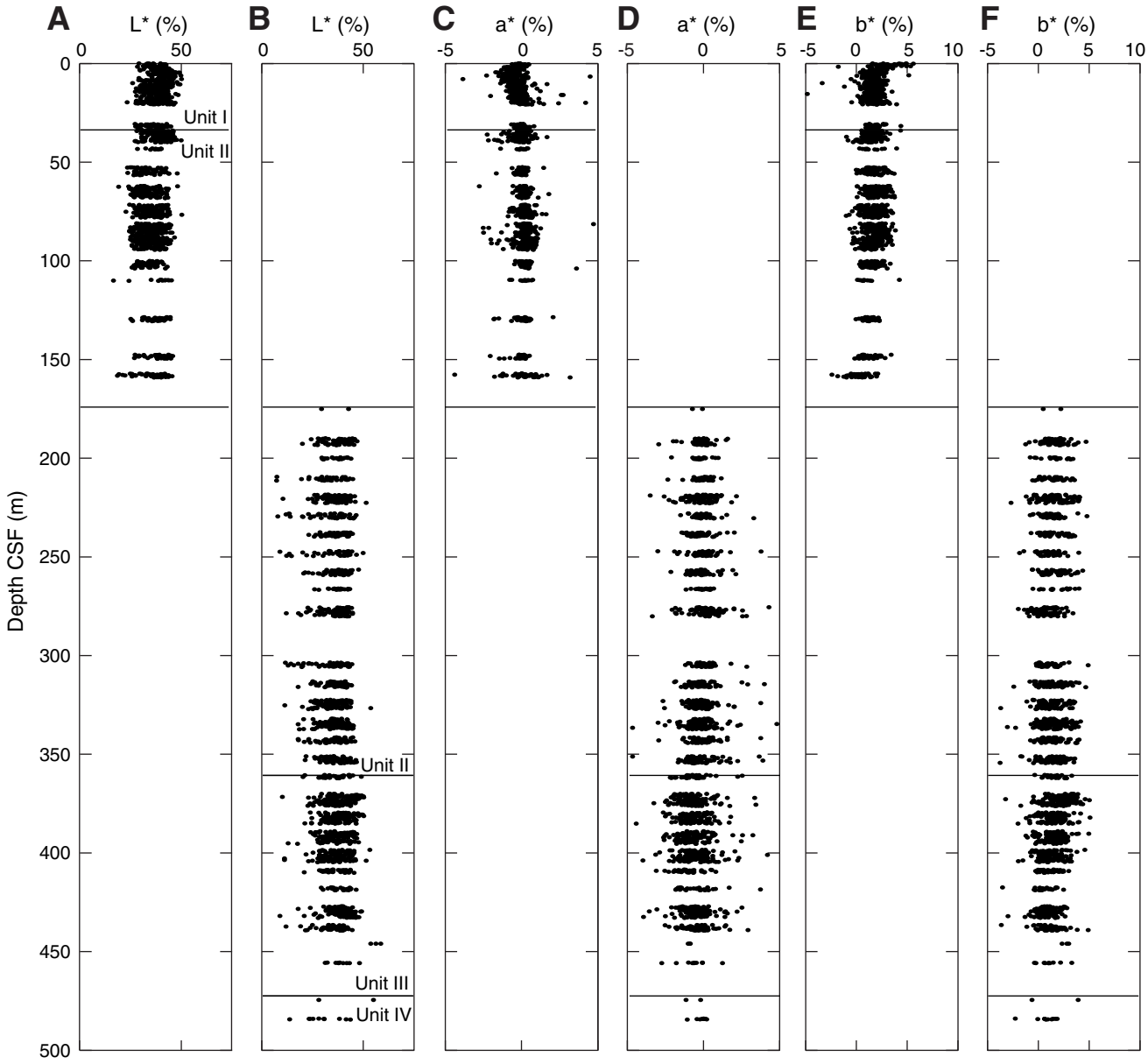

Figure F57. Magnetic susceptibility as a function depth. **A.** Holes C0007A, C0007B, and C0007C. **B.** Hole C0007D. CSF = core depth below seafloor.

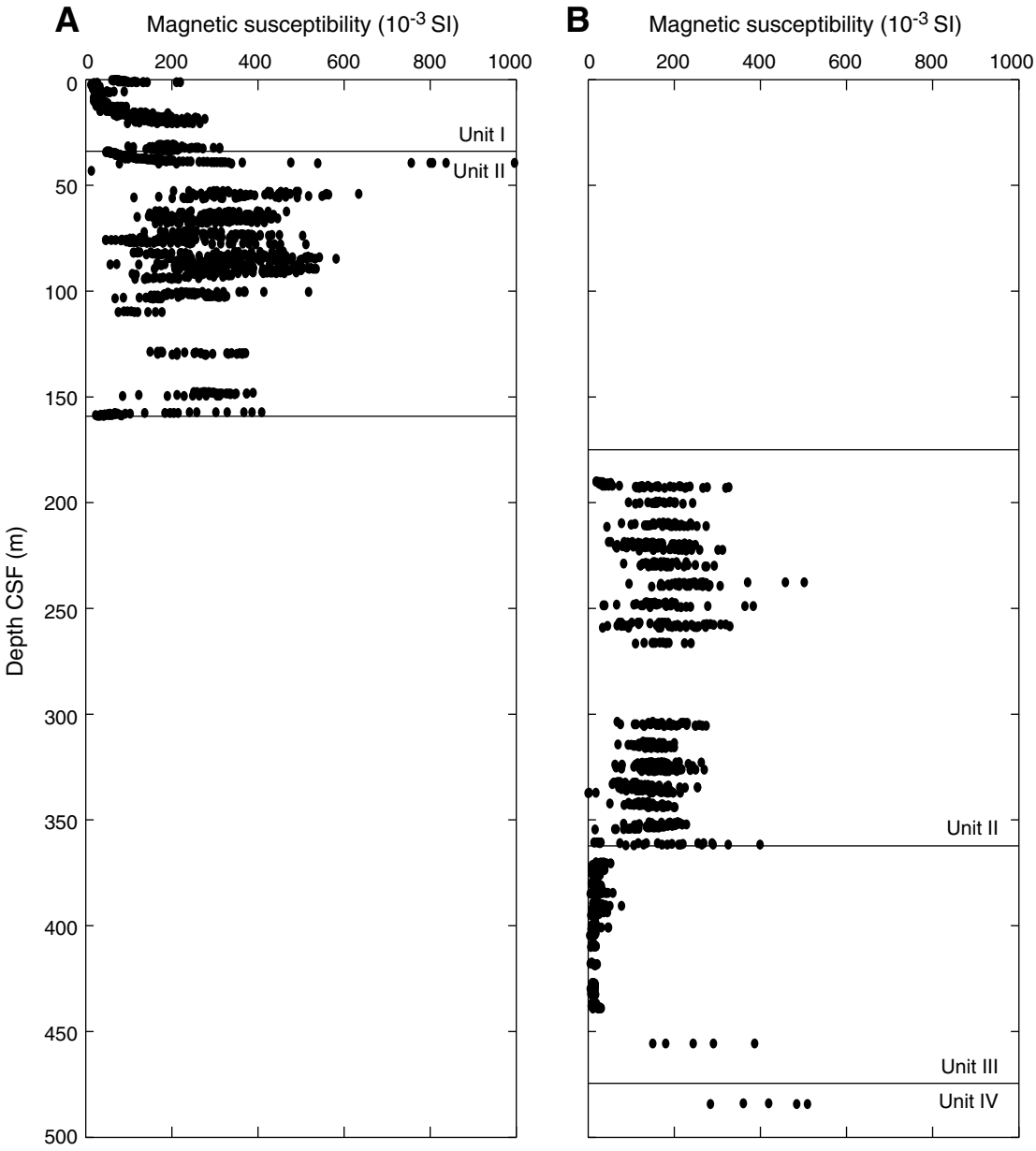

Figure F58. Natural gamma ray (NGR) values with depth. **A.** Holes C0007A, C0007B, and C0007C. **B.** Hole C0007D. CSF = core depth below seafloor. cps = counts per second.

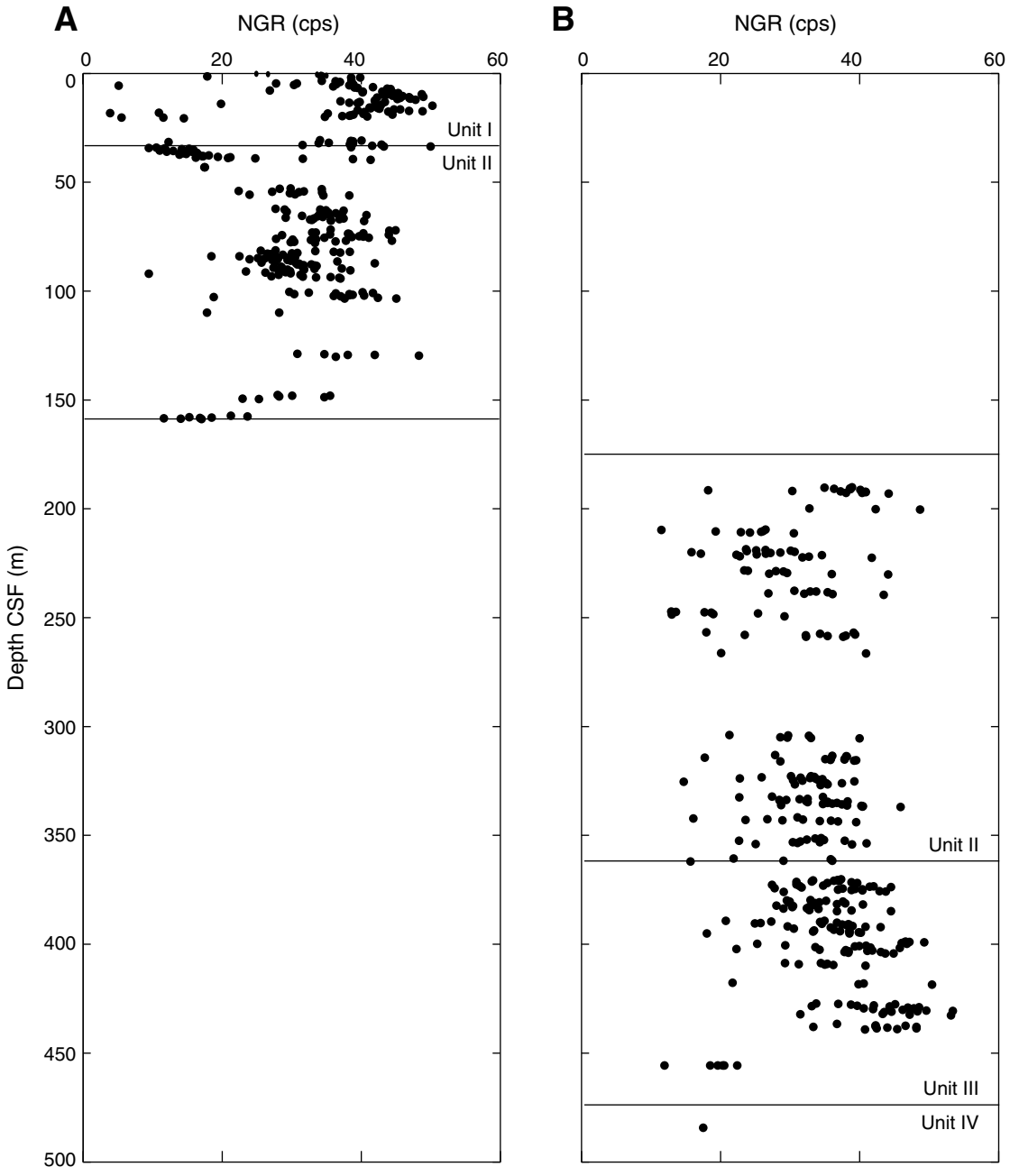

Figure F59. Natural gamma ray (NGR) counts from cores (MSCL-W) at all Site C0007 holes and Holes C0006E and C0006F. Numbers below holes are water depth (meters below mean sea level). For location of Inline 2437 see Figure **F1.** cps = counts per second. VE = vertical exaggeration.

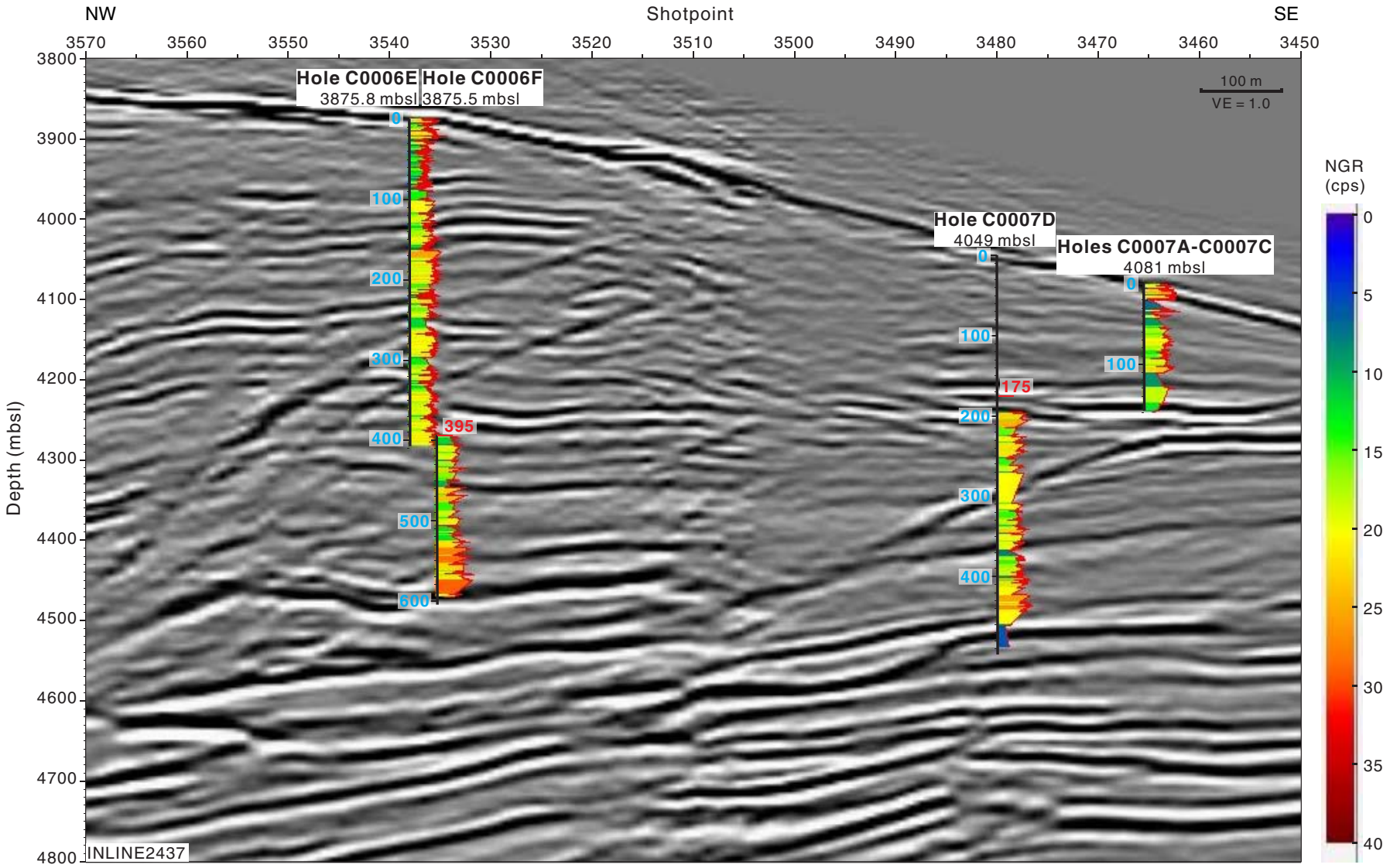

Table T1. Coring summary, Holes C0007A, C0007B, and C0007C. (See table note.)

Hole C0007A
Latitude: 33°01.2326′N
Longitude: 136°47.9485′E
Seafloor (drillers measurement from rig floor, m): 4109.5
Distance between rig floor and sea level (m): 28.5
Water depth (drillers measurement from sea level, m): 4081.0
Total depth (drillers depth below rig floor, m): 4112.64
Total penetration (core depth below seafloor, m): 3.14
Total length of cored section (m): 3.14
Total core recovered (m): 3.14
Core recovery (%): 100.00
Total number of cores: 1

Hole C0007B
Latitude: 33°01.2326′N
Longitude: 136°47.9485′E
Seafloor (drillers measurement from rig floor, m): 4109.5
Distance between rig floor and sea level (m): 28.5
Water depth (drillers measurement from sea level, m): 4081.0
Total depth (drillers depth below rig floor, m): 4122.14
Total penetration (core depth below seafloor, m): 12.64
Total length of cored section (m): 9.5
Total core recovered (m): 10.03
Core recovery (%): 105.58
Total number of cores: 1

Hole C0007C
Latitude: 33°01.2326′N
Longitude: 136°47.9485′E
Seafloor (drillers measurement from rig floor, m): 4109.5
Distance between rig floor and sea level (m): 28.5
Water depth (drillers measurement from sea level, m): 4081.0
Total depth (drillers depth below rig floor, m): 4285.59
Total penetration (core depth below seafloor, m): 176.09
Total length of cored section (m): 163.5
Total core recovered (m): 59.31
Core recovery (%): 36.29
Total number of cores: 18

Core	Date (Jan 2008)	Local time Shot	Local time On deck	Depth DRF (m) Top	Depth DRF (m) Bottom	Depth CSF (m) Top	Depth CSF (m) Bottom	Advanced (m)	Recovered (m)	Recovery (%)
316-C0007A-										
1H	14	2341	0021	4103.00	4112.50	0.00	3.14	3.14	3.14	100.00
316-C0007B-										
1H	15	0140	0231	4112.50	4122.00	3.14	12.64	9.50	10.03	105.58
316-C0007C-										
1H	15	0405	0444	4122.00	4129.95	12.64	20.59	7.95	7.95	100.00
2H	15	0630	0735	4129.95	4139.45	20.59	30.09	9.50	0.06	0.63
3H	15	1034	1118	4139.45	4148.95	30.09	39.59	9.50	9.88	104.00
4H	15	1233	1326	4148.95	4152.45	39.59	43.09	3.50	0.09	2.57
5X	15	1521	1759	4152.45	4161.95	43.09	52.59	9.50	0.53	5.58
6X	15	2101	2334	4161.95	4171.45	52.59	62.09	9.50	4.02	42.32
7X	16	0038	0223	4171.45	4180.95	62.09	71.59	9.50	6.06	63.79
8X	16	0310	0503	4180.95	4190.45	71.59	81.09	9.50	6.48	68.21
9X	16	0833	1015	4190.45	4199.95	81.09	90.59	9.50	9.79	103.05
10X	16	1052	1228	4199.95	4209.45	90.59	100.09	9.50	3.87	40.74
11X	16	1325	1530	4209.45	4218.95	100.09	109.59	9.50	3.77	39.68
12X	16	1616	1804	4218.95	4228.45	109.59	119.09	9.50	0.56	5.89
13X	16	1905	2105	4228.45	4237.95	119.09	128.59	9.50	0.00	0.00
14X	16	2310	0456	4237.95	4247.45	128.59	138.09	9.50	2.03	21.37
15X	17	0600	0747	4247.45	4256.95	138.09	147.59	9.50	0.09	0.95
16H	17	0851	0956	4256.95	4266.45	147.59	157.09	9.50	2.12	22.32
17H	17	1240	1320	4266.45	4275.95	157.09	166.59	9.50	2.01	21.16

Note: DRF = drillers depth below rig floor, CSF = core depth below seafloor.

Table T2. Coring summary, Hole C0007D. (See table note.)

Hole C0007D
Latitude: 33°01.3167′N
Longitude: 136°47.8872′E
Seafloor (drillers measurement from rig floor, m): 4077.5
Distance between rig floor and sea level (m): 28.5
Water depth (drillers measurement from sea level, m): 4049.0
Total depth (drillers depth below rig floor, m): 4571.00
Total penetration (core depth below seafloor, m): 493.50
Total length of cored section (m): 318.5
Total core recovered (m): 87.93
Core recovery (%): 27.61
Total number of cores: 35

Core	Date (Jan 2008)	Local time Shot	Local time On deck	Depth DRF (m) Top	Depth DRF (m) Bottom	Depth CSF (m) Top	Depth CSF (m) Bottom	Advanced (m)	Recovered (m)	Recovery (%)
316-C0007D-										
1R	19	1404	1534	4252.50	4262.00	175.00	184.50	9.50	0.16	1.68
2R	19	1625	1757	4262.00	4267.50	184.50	190.00	5.50	0.00	0.00
3R	19	2020	2157	4267.50	4277.00	190.00	199.50	9.50	3.36	35.37
4R	19	2321	0114	4277.00	4286.50	199.50	209.00	9.50	1.12	11.79
5R	20	0245	0428	4286.50	4296.00	209.00	218.50	9.50	2.47	26.00
6R	20	0521	0714	4296.00	4305.50	218.50	228.00	9.50	4.26	44.84
7R	20	0832	1015	4305.50	4315.00	228.00	237.50	9.50	2.52	26.53
8R	20	1522	1647	4315.00	4324.50	237.50	247.00	9.50	2.32	24.42
9R	20	1745	1924	4324.50	4334.00	247.00	256.50	9.50	2.59	27.26
10R	20	2059	2241	4334.00	4343.50	256.50	266.00	9.50	2.82	29.68
11R	21	0055	0310	4343.50	4353.00	266.00	275.50	9.50	0.71	7.47
12R	21	0517	0725	4353.00	4362.50	275.50	285.00	9.50	4.72	49.68
13R	21	0905	1106	4362.50	4372.00	285.00	294.50	9.50	0.00	0.00
14R	21	1240	1403	4372.00	4381.00	294.50	303.50	9.00	0.00	0.00
15R	21	1604	1731	4381.00	4390.50	303.50	313.00	9.50	2.34	24.63
16R	21	1927	2043	4390.50	4400.00	313.00	322.50	9.50	2.98	31.37
17R	21	2244	0023	4400.00	4409.50	322.50	332.00	9.50	4.73	49.79
18R	22	0200	0336	4409.50	4419.00	332.00	341.50	9.50	5.33	56.11
19R	22	0445	1007	4419.00	4428.50	341.50	351.00	9.50	2.77	29.16
20R	22	1110	1254	4428.50	4438.00	351.00	360.50	9.50	3.58	37.68
21R	22	1420	1547	4438.00	4447.50	360.50	370.00	9.50	1.70	17.89
22R	22	1651	1842	4447.50	4457.00	370.00	379.50	9.50	6.17	64.95
23R	22	1953	2130	4457.00	4466.50	379.50	389.00	9.50	5.70	60.00
24R	22	2234	0028	4466.50	4476.00	389.00	398.50	9.50	6.24	65.68
25R	23	0152	0413	4476.00	4485.50	398.50	408.00	9.50	6.10	64.21
26R	23	0527	0720	4485.50	4495.00	408.00	417.50	9.50	2.02	21.26
27R	23	0951	1117	4495.00	4504.50	417.50	427.00	9.50	1.42	14.95
28R	23	1239	1457	4504.50	4514.00	427.00	436.50	9.50	5.88	61.89
29R	23	1655	1849	4514.00	4523.50	436.50	446.00	9.50	2.88	30.32
30R	23	2032	2156	4523.50	4533.00	446.00	455.50	9.50	0.12	1.26
31R	23	2248	0018	4533.00	4538.00	455.50	460.50	5.00	0.40	7.90
32R	24	0156	0326	4538.00	4542.50	460.50	465.00	4.50	0.00	0.00
33R	24	0435	0600	4542.50	4552.00	465.00	474.50	9.50	0.00	0.00
34R	24	0847	1019	4552.00	4561.50	474.50	484.00	9.50	0.09	0.89
35R	24	1331	1446	4561.50	4571.00	484.00	493.50	9.50	0.44	4.63

Note: DRF = drillers depth below rig floor, CSF = core depth below seafloor.

Table T3. Summary of lithologic units, Holes C0007A, C0007B, and C0007C. (See table note.)

Unit	Hole, core, section, interval (cm) Top	Hole, core, section, interval (cm) Bottom	Depth CSF (m) Top	Depth CSF (m) Bottom	Thickness (m)	Stratigraphic age	Lithologic description	Processes of formation
I	316-C0007A-1H-1, 0	316-C0007C-3H-5, 80	0.00	33.94	33.94	Pleistocene	Nannofossil-bearing mud, interbedded sand layers (thinning upward), and volcanic ash layers	Hemipelagic settling, turbidites, and volcanic ash layers; slumping
IIAi	C0007C-3H-5, 80	C0007C-8X-2, 98	33.94	73.99	40.05	Pleistocene	Thick to thin sands (thickening upward) with thin interbedded nannofossil-bearing mud layers and volcanic ash layers	Turbidites, hemipelagic settling, and volcanic ash layers
IIB	C0007C-8X-2, 98	C0007C-12X-1, 0	74.00	109.59	35.6	Pleistocene	Sands (thinning upward) interbedded with nannofossil-bearing mud	Turbidites, hemipelagic settling
IIAii	C0007C-12X-1,0	C0007C-17H-CC, 13	109.59	159.13	49.54	Pleistocene	Thinning and fining-upward beds of gravel and sand with thin interbeds of nannofossil-bearing mud	Gravelly and sandy turbidites, hemipelagic settling

Note: CSF = core depth below seafloor.

Table T4. Summary of lithologic units, Hole C0007D. (See table note.)

Unit	Core, section, interval (cm) Top	Core, section, interval (cm) Bottom	Depth CSF (m) Top	Depth CSF (m) Bottom	Thickness (m)	Stratigraphic age	Lithologic description	Processes of formation
IIAii	316-C0007D-1R-1, 0	316-C0007D-3R-1, 5	175.00	190.05	15.05	Pleistocene	Thinning and fining upward beds of gravel and sand with thin interbeds of nannofossil-bearing mud	Gravelly and sandy turbidites, hemipelagic settling
IICi	3R-1, 5	11R-1, 20	190.05	266.20	76.15	Pleistocene	Mud, mudstone with sand/silt layers and rare volcanic layers	Hemipelagic settling, thin-bedded turbidites, and rare volcanic ash falls
IIAiii	11R-1, 20	15R-1, 0	266.20	303.50	37.30	Pleistocene	Thinning and fining-upwards bed of gravel and sand with thin interbeds of nannofossil-bearing mud	Gravelly and sandy turbidites, hemipelagic settling
IICii	15R-1, 0	17R-3, 79	303.50	326.02	22.52	Pleistocene	Mud, mudstone with silt layers and rare volcanic layers	Hemipelagic settling, thin-bedded turbidites, and rare volcanic ash falls
IID	17R-3, 79	21R-CC, 36	326.02	362.26	36.24	Pleistocene	Mudstone with volcanic ash layers and rare thin silt layers	Hemipelagic settling, volcanic ash layers, and rare thin-bedded turbidites
III	21R-CC, 36	29R-CC, 29	362.26	439.44	77.18	Pliocene	Mudstone with volcanic ashstone layers	Hemipelagic settling, volcanic ash layers
IV	29R-CC, 29	35R-CC, 19	439.44	484.44	45.00	Pliocene	Sand, mudstone	Sandy turbidites, hemipelagic settling

Note: CSF = core depth below seafloor.

Table T5. XRD data, Holes C0007A, C0007B, and C0007C. (See table notes.) (Continued on next page.)

				Peak intensity (counts/step)				Integrated peak area (total counts)				Abundance calculated from SVD normalization factor										
												Calculated abundance (wt%)						Normalized abundance (wt%)				
Unit	Core, section, interval (cm)	Core type	Depth CSF (m)	Clay	Quartz	Plagioclase	Calcite	Clay	Quartz	Plagioclase	Calcite	Clay	Quartz	Plagioclase	Calcite	Corrected calcite	Absolute total	Clay	Quartz	Plagioclase	Calcite	Relative total
	316-C0007A-																					
I	1H-2, 0–1.5	WR	1.42	76	1,413	437	83	2,809	41,177	24,803	2,643	44.0	22.7	31.2	–0.8	0.0	98.0	44.9	23.2	31.9	0.0	100
	1H-4, 0–1.5	WR	2.73	54	1,202	319	134	2,236	37,904	21,243	5,500	36.0	21.0	26.7	3.6	3.6	87.3	41.3	24.1	30.5	4.1	100
	1H-CC, 14–15.5	WR	3.09	46	1,260	442	158	1,678	38,648	26,190	6,088	34.1	21.3	33.6	4.6	4.6	93.6	36.4	22.8	35.9	4.9	100
	316-C0007B-																					
I	1H-1, 66–67.5	WR	3.80	57	1,164	292	111	2,169	38,595	20,136	3,937	34.5	21.5	25.1	1.6	1.6	82.7	41.7	26.0	30.4	2.0	100
	1H-3, 0–1.5	WR	5.73	52	152	178	85	1,121	5,634	13,627	2,948	20.9	2.6	18.1	2.4	2.4	43.9	47.6	5.8	41.2	5.4	100
	1H-6, 60–61	W	9.37	67	1,614	361	81	2,303	51,781	22,061	1,620	36.5	29.1	27.1	–2.0	0.0	92.7	39.3	31.4	29.2	0.0	100
	1H-6, 15–16.5	WR	8.92	70	1,777	420	95	1,909	54,729	29,610	2,946	38.0	30.6	37.4	–0.3	0.0	106.0	35.8	28.9	35.3	0.0	100
	1H-7, 0–1.5	WR	9.77	66	1,178	316	60	2,626	40,691	18,625	2,641	37.7	22.7	22.8	–0.4	0.0	83.3	45.3	27.3	27.4	0.0	100
	1H-9, 114–115	W	11.36	93	1,144	242	91	3,584	38,792	14,144	3,689	44.1	21.6	16.5	0.5	0.5	82.7	53.3	26.2	20.0	0.6	100
	316-C0007C-																					
I	1H-1, 60–61.5	WR	13.24	52	1,735	435	82	1,580	53,461	30,351	2,956	35.3	29.9	38.6	–0.1	0.0	103.8	34.0	28.8	37.2	0.0	100
	1H-2, 0–1.5	WR	14.05	13	1,480	292	78	1,353	50,658	24,181	3,228	28.7	28.5	30.3	0.8	0.8	88.4	32.5	32.3	34.3	0.9	100
	1H-5, 0–1.5	WR	16.89	45	1,696	415	68	1,728	54,235	24,998	1,610	32.8	30.5	31.2	–1.8	0.0	94.5	34.7	32.3	33.0	0.0	100
	1H-6, 116–118	W	18.28	45	483	262	91	1,024	15,175	17,228	3,775	22.1	8.0	22.6	3.1	3.1	55.8	39.6	14.4	40.5	5.5	100
	3H-2, 0–1.5	WR	31.50	49	1,110	467	41	1,815	52,793	33,021	2,714	39.6	29.3	42.2	–0.6	0.0	111.2	35.6	26.4	38.0	0.0	100
	3H-3, 39–40	W	32.12	66	1,183	253	103	2,736	36,701	18,291	3,679	38.8	20.4	22.5	1.0	1.0	82.7	46.9	24.6	27.2	1.2	100
	3H-3, 103–104.5	WR	32.76	59	1,331	274	85	2,831	42,408	16,977	2,979	38.5	23.8	20.4	–0.1	0.0	82.7	46.6	28.7	24.7	0.0	100
	3H-4, 0–1.5	WR	32.92	31	1,384	289	68	2,124	42,722	22,454	2,346	35.4	23.8	28.1	–0.6	0.0	87.4	40.6	27.3	32.2	0.0	100
	3H-5, 0–1.5	WR	33.14	68	1,143	361	50	2,623	41,265	25,113	1,272	42.3	22.8	31.7	–2.5	0.0	96.8	43.7	23.5	32.8	0.0	100
IIAi	3H-7, 78–80	A	36.52	31	1,316	512	53	1,166	45,116	31,880	1,949	32.7	25.0	41.2	–0.9	0.0	98.9	33.1	25.3	41.7	0.0	100
	5X-1, 3–4	W	43.12	72	1,200	264	69	2,826	38,939	17,126	2,442	38.7	21.7	20.8	–0.7	0.0	81.2	47.6	26.7	25.6	0.0	100
	6X-2, 75.5–77	WR	54.75	75	972	241	105	2,851	32,478	17,782	2,962	39.7	17.9	22.0	0.1	0.1	79.8	49.8	22.4	27.6	0.1	100
	6X-3, 0–1.5	WR	55.18	55	1,473	435	110	1,641	46,846	27,929	2,813	34.5	26.1	35.6	0.0	0.0	96.2	35.9	27.1	37.0	0.0	100
	6X-4, 55.5–57	WR	55.95	11	1,458	449	57	1,637	48,664	29,058	1,841	35.1	27.1	37.1	–1.4	0.0	99.3	35.4	27.3	37.3	0.0	100
	6X-CC, 22.5–24	WR	56.47	62	1,042	224	71	3,338	35,034	15,930	2,300	43.1	19.4	19.2	–1.1	0.0	81.7	52.7	23.7	23.5	0.0	100
	7X-1, 95–96.5	WR	63.04	55	1,422	452	53	1,795	46,428	27,160	1,621	35.4	25.8	34.5	–1.6	0.0	95.8	37.0	27.0	36.0	0.0	100
	7X-3, 0–1.5	WR	64.68	45	1,475	431	74	1,759	47,341	30,504	2,429	37.5	26.2	39.1	–0.7	0.0	102.8	36.5	25.5	38.0	0.0	100
	7X-4, 39–40.5	WR	65.30	56	1,135	331	76	2,348	37,113	23,550	3,052	38.8	20.4	29.8	0.3	0.3	89.3	43.4	22.9	33.4	0.3	100
	7X-5, 102–103.5	WR	67.34	72	1,356	389	88	1,767	43,526	27,239	2,519	35.4	24.1	34.8	–0.3	0.0	94.3	37.5	25.6	36.9	0.0	100
	8X-2, 15–16.5	WR	73.16	50	1,513	662	72	1,439	46,013	37,041	2,031	39.1	25.2	48.2	–1.2	0.0	112.5	34.8	22.4	42.8	0.0	100
IIB	8X-3, 0–1.5	WR	74.42	49	1,495	363	44	1,985	50,334	23,312	1,668	34.3	28.3	29.0	–1.7	0.0	91.6	37.5	30.9	31.7	0.0	100
	8X-5, 64–65.5	WR	76.48	47	950	314	53	2,300	30,164	19,920	2,024	35.9	16.5	25.2	–0.7	0.0	77.7	46.3	21.3	32.5	0.0	100
	9X-1, 65–66.5	WR	81.74	65	1,016	247	98	2,867	34,200	17,073	2,937	39.3	18.9	20.9	0.0	0.0	79.2	49.6	23.9	26.4	0.1	100
	9X-5, 0–1.5	WR	86.52	16	1,155	583	73	1,420	36,636	38,563	2,289	40.5	19.7	50.7	–0.6	0.0	110.9	36.5	17.7	45.8	0.0	100
	9X-6, 40–41.5	WR	87.14	66	1,059	342	101	2,127	35,551	25,353	2,786	37.9	19.5	32.5	0.1	0.1	89.9	42.2	21.7	36.1	0.1	100
	10X-1, 111–112.5	WR	91.70	57	1,057	282	45	2,742	35,893	18,683	1,552	39.1	19.9	23.1	–1.8	0.0	82.1	47.6	24.2	28.2	0.0	100
	10X-2, 0–1.5	WR	92.00	67	1,192	265	91	2,496	39,322	17,996	1,934	36.0	22.0	22.1	–1.2	0.0	80.1	45.0	27.4	27.6	0.0	100
	10X-CC, 6–7.5	WR	94.31	37	2,475	574	36	910	71,742	40,771	1,055	35.3	40.3	52.2	–3.0	0.0	127.9	27.6	31.5	40.9	0.0	100
	11X-1, 22.5–24	WR	100.32	59	1,485	417	49	2,004	46,174	28,208	1,299	38.2	25.6	35.9	–2.2	0.0	99.8	38.3	25.7	36.0	0.0	100
	11X-1, 118–119	W	101.27	53	2,068	476	54	983	65,043	42,428	1,526	37.6	36.3	54.8	–2.3	0.0	128.7	29.2	28.2	42.6	0.0	100
	11X-2, 56–57.5	WR	102.07	81	1,203	248	73	3,204	38,498	15,359	2,303	41.2	21.5	18.3	–1.1	0.0	80.9	50.9	26.5	22.6	0.0	100
	11X-3, 0–1.5	WR	102.70	48	1,966	587	85	1,520	59,558	33,624	2,742	36.8	33.3	42.8	–0.6	0.0	113.0	32.6	29.5	37.9	0.0	100
	11X-4, 67–68.5	WR	103.61	47	1,926	834	86	1,122	58,490	45,425	2,407	41.5	32.3	59.2	–1.1	0.0	133.0	31.2	24.3	44.5	0.0	100

Table T5 (continued).

Unit	Core, section, interval (cm)	Core type	Depth CSF (m)	Peak intensity (counts/step)				Integrated peak area (total counts)				Abundance calculated from SVD normalization factor									
												Calculated abundance (wt%)						Normalized abundance (wt%)			
				Clay	Quartz	Plagioclase	Calcite	Clay	Quartz	Plagioclase	Calcite	Clay	Quartz	Plagioclase	Calcite	Corrected calcite	Absolute total	Clay	Quartz	Plagioclase	Calcite	Relative total
	11X-CC, 21–22.5	WR	103.83	42	2,396	507	40	943	72,235	39,825	1,010	35.0	40.6	50.9	–3.1	0.0	126.5	27.6	32.1	40.3	0.0	100
IIAii	12X-1, 34–36	W	109.93	48	2,153	817	46	792	65,270	46,439	1,234	38.6	36.3	60.4	–2.7	0.0	135.2	28.6	26.8	44.6	0.0	100
	14X-1, 67–68	W	129.26	81	1,062	257	84	2,998	36,473	18,586	2,818	41.6	20.2	22.9	–0.3	0.0	84.6	49.1	23.8	27.0	0.0	100
	14X-2, 0–1.5	WR	129.73	62	1,692	420	60	1,771	52,599	35,904	1,933	41.3	29.1	46.2	–1.7	0.0	116.6	35.4	25.0	39.6	0.0	100
	16H-1, 100–101	W	148.59	35	3,973	1,173	37	695	110,575	82,626	1,359	61.9	61.4	107.9	–5.2	0.0	231.1	26.8	26.6	46.7	0.0	100
	16H-2, 0–1.5	WR	149.00	32	3,799	1,189	30	644	103,656	77,085	1,113	57.6	57.5	100.6	–5.0	0.0	215.8	26.7	26.7	46.6	0.0	100

Notes: CSF = core depth below seafloor. SVD = singular value decomposition. WR = whole-round, W = working half, A = archive half.

Table T6. XRD mineralogy by unit. (See table note.)

Mineral	Maximum	Minimum	Average	Standard deviation
Unit I				
Clay	53.3	32.5	41.1	5.7
Quartz	32.3	5.8	25.2	6.4
Plagioclase	41.2	20.0	32.3	5.5
Calcite	5.5	0.0	1.4	2.1
Calcite	5.5	0.6	3.1	2.1
Subunit IIA				
Clay	52.7	26.7	38.1	8.2
Quartz	27.3	22.4	25.3	1.7
Plagioclase	46.7	23.5	36.5	7.4
Calcite	0.3	0.0	0.0	0.1
Calcite	0.3	0.1	0.3	0.3
Subunit IIB				
Clay	50.9	27.6	38.7	8.3
Quartz	32.1	17.7	26.1	4.2
Plagioclase	45.8	22.6	35.2	7.2
Calcite	0.1	0.0	0.0	0.0
Calcite	0.1	0.1	0.1	0.0

Note: For each subunit, calcite results are first presented for all samples and then for only those samples containing calcite.

Table T7. XRD data, Hole C0007D. (See table notes.) (Continued on next page.)

				Peak intensity (counts/step)				Integrated peak area (total counts)				Abundance calculated from SVD normalization factor									
												Calculated abundance (wt%)						Normalized abundance (wt%)				
Unit	Core, section, interval (cm)	Core type	Depth CSF (m)	Clay	Quartz	Plagioclase	Calcite	Clay	Quartz	Plagioclase	Calcite	Clay	Quartz	Plagioclase	Calcite	Corrected calcite	Absolute total	Clay	Quartz	Plagioclase	Calcite	Relative Total
	316-C0007D-																					
I	3R-2, 0–1.5	WR	191.42	55	1,426	348	64	2,864	47,472	23,372	1,901	43.2	26.5	29.0	–1.9	0.0	98.6	43.8	26.8	29.4	0.0	100
	3R-3, 69–70.5	WR	192.45	75	1,651	373	53	2,638	50,974	24,925	1,253	41.9	28.5	31.0	–2.8	0.0	101.4	41.3	28.1	30.6	0.0	100
	4R-1, 0–6	W	199.50	3	376	110	59	505	11,182	5,239	1,319	8.3	6.3	6.5	0.8	0.8	21.9	38.0	28.6	29.6	3.7	100
	4R-1, 37–38.5	WR	199.87	68	1,006	283	80	3,032	37,119	19,022	2,150	42.2	20.5	23.4	–1.3	0.0	86.2	49.0	23.8	27.2	0.0	100
	5R-1, 0–1.5	WR	209.00	49	1,165	404	75	1,846	38,441	29,954	2,770	38.4	21.0	38.7	0.0	0.0	98.1	39.1	21.4	39.5	0.0	100
	6R-1, 29–30	W	218.79	55	1,047	266	119	2,872	34,026	16,994	3,967	39.4	18.8	20.8	1.4	1.4	80.4	48.9	23.4	25.9	1.7	100
	6R-3, 98.5–100	WR	221.44	58	1,011	260	112	2,939	36,525	18,800	3,214	41.2	20.2	23.2	0.2	0.2	84.8	48.6	23.8	27.3	0.3	100
	7R-1, 68–69	W	228.68	71	1,092	271	75	3,008	35,667	17,443	2,672	40.9	19.7	21.3	–0.5	0.0	82.0	49.9	24.1	26.0	0.0	100
	7R-1, 98.5–100	WR	228.99	62	887	245	68	3,366	33,445	17,893	1,859	44.8	18.4	22.0	–1.7	0.0	85.2	52.6	21.6	25.8	0.0	100
	8R-1, 72–73	W	238.22	67	1,006	239	110	2,884	34,900	18,035	3,836	40.2	19.3	22.2	1.1	1.1	82.9	48.5	23.3	26.8	1.4	100
	8R-1, 90–91.5	WR	238.40	58	775	201	96	2,759	26,277	15,458	3,960	37.5	14.4	19.1	1.8	1.8	72.7	51.5	19.7	26.3	2.4	100
	9R-2, 23–24.5	WR	248.65	57	1,047	255	131	3,035	34,403	17,313	4,782	41.2	19.0	21.2	2.3	2.3	83.8	49.2	22.7	25.3	2.8	100
	9R-2, 77.5–79	WR	249.20	65	1,143	289	106	3,403	39,257	19,907	2,979	46.4	21.7	24.4	–0.6	0.0	92.6	50.2	23.4	26.4	0.0	100
	10R-1, 50–51.5	WR	257.00	68	1,028	249	164	3,703	34,103	16,949	6,137	47.6	18.8	20.5	3.6	3.6	90.5	52.6	20.7	22.7	4.0	100
	15R-1, 85–86.5	WR	304.35	64	1,046	250	82	3,680	35,081	17,378	2,631	47.5	19.3	21.1	–1.0	0.0	87.9	54.1	22.0	24.0	0.0	100
	16R-1, 95–96.5	WR	313.95	82	1,126	227	64	3,533	36,327	15,916	1,697	44.9	20.1	19.1	–2.1	0.0	84.1	53.4	23.9	22.7	0.0	100
	16R-2, 100–101.5	WR	315.42	69	1,136	219	86	3,459	36,613	16,798	2,941	44.9	20.3	20.3	–0.5	0.0	85.4	52.5	23.7	23.8	0.0	100
	17R-3, 0–1.5	WR	325.30	72	1,122	266	53	3,126	38,099	20,610	2,173	44.2	21.0	25.5	–1.4	0.0	90.8	48.7	23.2	28.1	0.0	100
II	17R-CC, 10–11.5	WR	327.12	60	783	236	43	3,832	36,529	18,945	1,714	50.1	20.1	23.1	–2.4	0.0	93.2	53.7	21.5	24.8	0.0	100
	18R-1, 24–25.5	WR	332.24	82	1,048	231	164	4,122	33,950	16,170	5,366	51.2	18.6	19.3	2.3	2.3	91.5	55.9	20.4	21.1	2.5	100
	18R-1, 62–63.5	WR	332.62	68	945	233	182	3,106	32,345	15,999	6,669	41.1	17.9	19.5	4.8	4.8	83.3	49.4	21.4	23.4	5.8	100
	19R-1, 31–32.5	WR	341.81	67	1,026	261	99	3,118	33,034	17,577	3,717	42.2	18.2	21.6	0.9	0.9	82.9	50.9	21.9	26.1	1.1	100
	20R-1, 84.5–86	WR	351.85	60	803	250	29	3,835	37,400	19,998	1,791	50.8	20.5	24.5	–2.4	0.0	95.9	53.0	21.4	25.6	0.0	100
	21R-1, 57–58.5	WR	361.07	75	678	353	41	3,470	22,361	21,705	1,467	49.1	11.7	27.7	–2.1	0.0	88.5	55.5	13.2	31.3	0.0	100
	21R-CC, 32–34	W	362.22	88	1,097	192	77	4,537	32,504	12,453	1,680	52.5	17.9	14.2	–2.6	0.0	84.6	62.1	21.1	16.8	0.0	100
	22R-1, 47–48.5	WR	370.47	77	847	165	125	4,607	29,341	11,541	4,621	52.8	16.0	13.1	1.3	1.3	83.2	63.4	19.3	15.7	1.6	100
	22R-2, 78–112	WR	372.19	64	786	161	94	4,162	24,649	10,685	3,588	48.0	13.4	12.3	0.5	0.5	74.1	64.7	18.1	16.6	0.6	100
III	22R-3, 97–98.5	WR	373.79	82	949	203	53	5,445	31,878	14,391	1,093	62.9	17.3	16.6	–4.1	0.0	96.8	65.0	17.8	17.2	0.0	100
	23R-2, 23–24.5	WR	381.14	102	853	187	111	4,775	29,541	11,260	4,228	54.2	16.1	12.6	0.7	0.7	83.7	64.8	19.3	15.1	0.8	100
	23R-2, 113–114.5	WR	382.04	81	865	171	41	5,239	29,770	11,436	791	58.8	16.2	12.7	–4.2	0.0	87.7	67.0	18.4	14.5	0.0	100
	23R-3, 62–63.5	WR	382.96	76	985	171	79	4,243	29,774	13,324	2,311	50.4	16.3	15.6	–1.5	0.0	82.3	61.2	19.8	19.0	0.0	100
	23R-4, 14–15.5	WR	383.89	85	1,080	157	94	5,459	33,715	11,061	2,754	60.6	18.5	12.0	–1.9	0.0	91.1	66.5	20.3	13.2	0.0	100
	24R-1, 16.5–18	WR	389.17	85	995	187	155	5,014	31,569	11,749	5,056	56.9	17.3	13.1	1.5	1.5	88.8	64.1	19.5	14.8	1.7	100
	24R-2, 105.5–107	WR	391.47	81	1,073	188	38	5,840	34,105	13,343	1,253	65.9	18.6	15.0	–4.2	0.0	99.5	66.3	18.6	15.1	0.0	100
	24R-3, 66.5–68	WR	392.51	103	1,010	176	14	5,014	34,179	12,482	1,157	57.1	18.8	14.0	–3.7	0.0	89.9	63.5	20.9	15.6	0.0	100
	24R-3, 98.5–100	WR	392.83	64	768	173	8	4,108	28,702	11,424	1,259	47.7	15.7	13.1	–2.7	0.0	76.5	62.3	20.6	17.1	0.0	100
	24R-5, 42–43.5	WR	395.09	88	1,110	224	68	5,976	32,254	12,460	1,108	66.7	17.5	13.8	–4.4	0.0	98.0	68.1	17.8	14.1	0.0	100
	25R-2, 80–81.5	WR	400.73	75	946	227	49	5,258	32,664	15,796	1,714	62.1	17.7	18.6	–3.2	0.0	98.3	63.1	18.0	18.9	0.0	100
	25R-3, 22–23	W	401.59	83	1,032	194	58	5,453	34,072	11,673	1,679	60.9	18.7	12.8	–3.3	0.0	92.4	65.9	20.2	13.9	0.0	100
	25R-3, 50–51.5	WR	401.87	90	947	214	62	5,137	33,820	12,275	2,164	58.3	18.5	13.7	–2.5	0.0	90.5	64.4	20.5	15.2	0.0	100
	26R-1, 0–1.5	WR	408.00	92	966	174	57	5,982	32,999	11,919	1,852	66.4	17.9	13.0	–3.5	0.0	97.4	68.2	18.4	13.4	0.0	100
	26R-1, 133.5–135	WR	409.34	76	841	191	90	4,845	31,571	11,414	2,176	54.9	17.3	12.7	–2.1	0.0	84.9	64.6	20.4	15.0	0.0	100
	27R-1, 24–25.5	WR	417.74	117	997	189	63	4,361	31,834	12,581	2,006	50.9	17.5	14.5	–2.0	0.0	82.9	61.4	21.1	17.5	0.0	100

Table T7 (continued).

Unit	Core, section, interval (cm)	Core type	Depth CSF (m)	Peak intensity (counts/step)				Integrated peak area (total counts)				Abundance calculated from SVD normalization factor									
												Calculated abundance (wt%)						Normalized abundance (wt%)			
				Clay	Quartz	Plagioclase	Calcite	Clay	Quartz	Plagioclase	Calcite	Clay	Quartz	Plagioclase	Calcite	Corrected calcite	Absolute total	Clay	Quartz	Plagioclase	Calcite	Relative Total
	28R-4, 12–13.5	WR	431.37	85	1,155	184	48	5,534	34,340	9,866	1,821	60.4	18.9	10.3	–3.1	0.0	89.6	67.4	21.1	11.5	0.0	100
	29R-1, 31–32.5	WR	436.81	88	867	163	191	4,919	29,983	10,569	6,614	55.2	16.4	11.6	3.7	3.7	87.0	63.5	18.9	13.4	4.3	100

Notes: CSF = core depth below seafloor. SVD = singular value decomposition. WR = whole-round, W = working half.

Table T8. XRD mineralogy by unit. (See table note.)

Mineral	Maximum	Minimum	Average	Standard deviation
Subunit IIC				
Clay	54.1	38.0	48.4	4.8
Quartz	28.6	19.7	23.6	2.3
Plagioclase	39.5	22.7	27.1	3.8
Calcite	4.0	0.0	0.9	1.4
Calcite	4.0	0.3	2.3	1.3
Subunit IID				
Clay	62.1	49.4	54.4	4.1
Quartz	21.9	13.2	20.1	3.1
Plagioclase	31.3	16.8	24.2	4.5
Calcite	5.8	0.0	1.3	2.2
Calcite	5.8	1.1	3.1	2.4
Unit III				
Clay	68.2	61.2	64.8	2.0
Quartz	21.1	17.8	19.4	1.1
Plagioclase	19.0	11.5	15.3	1.9
Calcite	4.3	0.0	0.4	1.0
Calcite	4.3	0.6	1.8	1.5

Note: For each subunit, calcite results are first presented for all samples and then for only those samples containing calcite.

Table T9. Calcareous nannofossil range chart of age-diagnostic fossils, Hole C0007C. (See table notes.)

Epoch	Nannofossil zone		Core, sample, interval (cm)	Depth CSF (m) Top	Bottom	Mean	Abundance	Preservation	*Calcidiscus macintyrei*	*Emiliania huxleyi*	*Gephyrocapsa* spp. large (>5.5 µm)	*Gephyrocapsa* spp. medium I (>3.5–4 µm)	*Gephyrocapsa* spp. medium II (>4–5.5 µm)	*Gephyrocapsa* spp. smaller (<3.5 µm)	*Helicosphaera sellii*	*Pseudoemiliania lacunosa*	*Reticulofenestra asanoi*	*Reticulofenestra haqii-minutula*	*Reticulofenestra pseudoumbilicus* (5–7 µm)	*Reticulofenestra pseudoumbilicus* (>7 µm)	*Sphenolithus abies*
			316-C0007C-																		
			1H-CC, 7–12	20.59	20.65	20.62	D	M	R	C?	T	D	D	A	R	C		R	R	R	
			2H-CC, 0–6	20.83	20.88	20.86	C	P				C	C	C		R			T		
			3H-CC, 0–5	39.59	39.68	39.64	A	P				C	A	A		C		R			
			4H-CC, 0–9	39.78	39.83	39.81	C	P				C	C	?		C					
			5X-CC, 0–5	43.19	43.24	43.22	A	P	T		T	C	A	C		C	T	R	T	T	
			6X-CC, 0–5	56.25	56.30	56.27	A	P	R		R	C	A	C		C		R	T	T	
			7X-CC, 0–5	68.02	68.07	68.04	A	M	R		R	C	A	A		C		R	T	T	R
		NN19	8X-CC, 0–5	77.93	77.98	77.95	R	P				R	R			R		R			
			9X-CC, 0–5	90.56	90.61	90.59	C	P				F	F	F		F		F			
Pleistocene	NN19e		10X-1, 20			90.79	C	P	R		R	F	C	F		C	R?	F	R	R	T
			10X-CC, 0–6	94.25	94.31	94.28	B														
			11X-1, 24			100.33	F	P	T			T	R	R		F		R			
			11X-CC, 0–6	103.62	103.68	103.65	B														
			12X-1, 24			109.83	C	P			T	R	R			F	R	F			
			12X-CC, 0–5	110.01	110.06	110.03	B														
			14X-CC, 0–5			130.26	F	P				F	F	F		F		F			
		Reversed NN20	14X-CC, 24	130.23	130.28	130.47	D	M				D	D	A	R	R		R			
		Reversed NN19	15X-CC, 0–9			138.14	A	M			T	A	A	A		C		R			
			16X-1, 46	138.09	138.18	148.05	A	M			T	C	C	C		C		R			
		?	16H-CC, 0–5	149.62	149.67	149.65	B														
			17H-CC, 0–5	159.00	159.05	159.02	B														

Notes: CSF = core depth below seafloor. Abundance: D = dominant, A = abundant, C = common, F = few, R = rare, T = trace, B = barren. Preservation: M = medium, P = poor. ? = uncertain determination.

Table T10. Calcareous nannofossil range chart of age-diagnostic fossils, Hole C0007D. (See table notes.)

Epoch	Nannofossil zone	Core, section, interval (cm)	Depth CSF (m) Top	Bottom	Mean	Abundance	Preservation	*Amaurolithus delicatus*	*Amaurolithus primus*	*Calcidiscus macintyrei*	*Ceratolithus acutus*	*Ceratolithus rugosus*	*Discoaster asymmetricus*	*Discoaster brouweri*	*Discoaster pentaradiatus*	*Discoaster surculus*	*Discoaster tamalis*	*Emiliania huxleyi*	*Gephyrocapsa* spp. large (>5.5 µm)	*Gephyrocapsa* spp. medium I (>3.5–4 µm)	*Gephyrocapsa* spp. medium II (>4–5.5 µm)	*Gephyrocapsa* spp. smaller (<3.5 µm)	*Helicosphaera sellii*	*Pseudoemiliania lacunosa*	*Reticulofenestra asanoi*	*Reticulofenestra pseudoumbilicus* (>7 µm)	*Sphenolithus abies*
		316-C0007D-																									
		1R-CC, 0–5	175.00	175.05	175.03	F	P			R								R?	T	F	F	F	T	F	T		
		1R-CC, 10			175.10	C	M			T								C?	T	C	C	C	T	C			
		3R-1, 77			190.77	C	P			F				R	R			C?	R	C	C	C		C	F	R	R
		3R-CC, 0–5	193.15	193.20	193.17	B																					
		4R-1, 87			200.37	B																					
		4R-CC, 0–5	200.44	200.49	200.47	C	P			R									R	C	C	R		C	R	R	R
		5R-CC, 9–14	211.38	211.43	211.40	C	M													C	C	C		C	C		
		6R-CC, 6–11	222.64	222.69	222.67	C	M												T	C	C	C		C	C		
		7R-CC, 14			230.44	B																					
		7R-CC, 0–5	230.30	230.35	230.32	B																					
		8R-CC, 0–5	239.62	239.67	239.65	F	P													R	R			F	F		
		9R-CC, 0–5	249.43	249.48	249.46	C	M			T										C	C	C		C	C	T	T
		10R-2, 60			258.52	C	M			T										C		C		C	C		
Pleistocene	NN19	10R-CC, 0–5	259.07	259.12	259.09	T	P																	T	T		
		11R-CC, 0–5	266.54	266.59	266.57	T	P													T	T	T		T			
		12R-1, 4			275.54	C	M			T									T	C	F	C		C	C		
		12R-CC, 81–85	280.17	280.22	280.20	C	M			R										R		C		C	C		
		15R-CC, 20–25	305.80	305.85	305.82	C	P			T										F	C	C		C	C		
		16R-CC, 0–5	316.01	316.06	316.04	D	M			R										C		D		C	C	R	R
		17R-2, 118			323.68	B																					
		17R-CC, 21–26	327.23	327.28	327.25	B																					
		18R-CC, 0–5	337.17	337.22	337.19	C	P			R									T	R	R	C		C		R	R
		19R-CC, 0–5	344.03	344.08	344.06	D	G			C										C		D		C		R	R
		20R-CC, 18.5–23.5	354.58	354.63	354.60	A	P			T									T	T		F		C			
		21R-1, 11			360.61	D	M			T									C	T	C	A		A		T	
		21R-1, 92			361.42	T	P																	T			
		21R-CC, 25			362.15	F	P			R		T		F	F	R								F			
	NN16	21R-CC, 34–36	362.24	362.26	362.25	F	P			R		T		F	F	R								F			
		22R-1, 89			370.89	D	G			C	T		F	C	C	F	T					F	R	R		F	C
Pliocene		22R-CC, 9–14	376.15	376.20	376.17	B																					
		23R-1, 112			380.62	C	M			C	T		F	C	C	R						F	F	F		C	C
	NN15–NN14	23R-CC, 19.5–24.5	385.20	385.25	385.22	B																					
		24R-1, 135			390.35	C	M			C	T		F	C	C	R						F	F	F		C	C
		24R-CC, 0–5	395.20	395.25	395.23	R	P				T			R												R	R
	NN13	25R-4, 56			403.34	R	P			R	T	T		R	R							R		T		R	R
		25R-CC, 0–5	404.45	404.50	404.48	T	P							T												T	
		26R-2, 15			409.42	C	P			R				F	F	R						R		R		F	F
		26R-CC, 0–5	409.91	409.96	409.93	A	M			C	R			C	C	T						F		F		C	C
		27R-1, 86			418.36	C	M			C		T		C	C	R										C	C
		27R-CC, 0–5	418.70	418.75	418.72	R	P							R												R	R
		28R-5, 22			432.28	A	M			R	T			C	C	F										C	C
	NN12	28R-CC, 0–5	432.79	432.84	432.81	A	M		T	R	T			C	C	F										C	C
		29R-1, 16			436.66	C	M		T	R	T			F	F	R										C	R
		29R-2, 22			438.13	R	P			R				R	R											R	T
		29R-2, 33			438.24	F	P			R				F	F	R										F	R
	Reversed NN16	29R-2, 70			438.61	D	G			C			R	C	C	F	T					F	F	C		R	C
		29R-CC, 0–5	439.15	439.20	439.17	C	M			C			R	C	C	R	T					R		C		T	T
		29R-CC, 24			439.39	F	P			F	T	T	R	F	F	R	T					R		F			
	Fallings	30R-CC, 0–5	446.00	446.05	446.03	B																					
?	Fallings	31R-CC, 0–5	455.75	455.80	455.77	C	M	T	T	R	T			C	C	R							R			C	C
	?	34R-CC, 8–9	474.58	474.59	474.59	T	P																	T?		T	
	Fallings	35R-CC, 0–5			484.30	C	M			R				C	C											C	C

Notes: CSF = core depth below seafloor. Abundance: D = dominant, A = abundant, C = common, F = few, R = rare, T = trace, B = barren. Preservation: G = good, M = medium, P = poor. ? = uncertain determination.

Table T11. Recognized nannofossil events, Holes C0007C and C0007D. (See table notes.)

Nannofossil zone	Age (Ma)	Nannofossil event	Top		Bottom		Mean depth CSF (m)
			Core, section, interval (cm)	Depth CSF (m)	Core, section, interval (cm)	Depth CSF (m)	
			316-C0007C-		316-C0007C-		
NN19	0.436	LO *Pseudoemiliania lacunosa*		0.00	1H-CC, 7–12	20.62	10.31
Reversed NN19	0.436	LO *Pseudoemiliania lacunosa*	14X-CC, 24	130.47	15X-CC, 0–9	138.14	134.30
			316-C0007D-		316-C0007D-		
Reversed NN19	0.436	LO *Pseudoemiliania lacunosa*	1R-CC, 0–5	175.03	1R-CC, 10	175.10	175.06
NN19	0.9	LCO *Reticulofenestra asanoi*	4R-1, 87	200.37	4R-CC, 0–5	200.47	200.42
	1.04	RE *Gephyrocapsa* spp. (≥4 µm)	9R-CC, 0–5	249.46	10R-2, 60	258.52	253.99
	1.04	RE *Gephyrocapsa* spp. (≥4 µm)	15R-CC, 20–25	305.82	16R-CC, 0–5	316.04	310.93
	1.078	FCO *Reticulofenestra asanoi*	16R-CC, 0–5	316.04	17R-2, 118	323.68	319.86
	1.24	LO *Gephyrocapsa* spp. large (>5.5 µm)	17R-CC, 21–26	327.25	18R-CC, 0–5	337.19	332.22
	1.46	FCO *Gephyrocapsa* spp. large (>5.5 µm)	21R-1, 11	360.61	21R-1, 92	361.42	361.02
NN16	2.06	LO *Discoaster brouweri*	21R-1, 92	361.42	21R-CC, 25	362.15	361.79
	2.512	LO *Discoaster pentaradiatus*	21R-1, 92	361.42	21R-CC, 25	362.15	361.79
	2.52	LO *Discoaster surculus*	21R-1, 92	361.42	21R-CC, 25	362.15	361.79
	3.65	LO *Sphenolithus* spp.	21R-CC, 34–36	362.25	22R-1, 89	370.89	366.57
NN15–NN14	3.79	LO *Reticulofenestra pseudoumbilicus* (>7 µm)	22R-CC, 9–14	376.17	23R-1, 112	380.62	378.40
	4.13	FCO *Discoaster asymmetricus*	24R-1, 135	390.35	24R-CC, 0–5	395.23	392.79
NN13	5.04	LO *Ceratolithus acutus*	26R-2, 15	409.42	26R-CC, 0–5	409.93	409.67
	5.12	FO *Ceratolithus rugosus*	27R-1, 86	418.36	27R-CC, 0–5	418.72	418.54
NN12	5.32	FO *Ceratolithus acutus*	29R-1, 16	436.66	29R-2, 22	438.13	437.39
Reversed NN16	3.65	LO *Sphenolithus* spp.	29R-2, 33	438.24	29R-2, 70	438.61	438.42

Notes: CSF = core depth below seafloor. LO = last occurrence, LCO = last consistent occurrence, RE = reentrance, FCO = first consistent occurrence, FO = first occurrence.

Table T12. Uncorrected geochemistry results from interstitial waters, Site C0007. (See table notes.)

Core, section	Depth CSF (m) Top	Bottom	Average	pH	Alkalinity (mM)	Refractive index	Salinity	Cl (mM)	Br (mM)	SO_4 (mM)	Na (mM)	Na/Cl	K (mM)	Mg (mM)	Ca (mM)	PO_4 (µM)	NH_4 (µM)
316-C0007A-																	
1H-2	1.42	1.67	1.54	7.6	4.55	1.33940	35.33	555	0.83	26.73	486	0.875	12.0	48.10	9.49	10	167
1H-4	2.73	2.95	2.84	7.5	5.34	1.33941	35.39	554	0.84	25.44	485	0.875	11.9	47.90	8.73	11	386
316-C0007B-																	
1H-2	5.73	5.97	5.85	7.7	9.03	1.33935	35.06	556	0.85	20.42	490	0.881	11.4	44.60	7.37	28	1208
1H-4	9.77	9.99	9.88	7.7	11.55	1.33939	35.28	559	0.86	16.16	495	0.885	10.0	42.00	6.13	45	1892
316-C0007C-																	
1H-2	14.05	14.29	14.17	7.8	14.80	1.33922	34.33	553	0.85	12.33	490	0.887	10.2	39.40	5.21	60	2920
1H-5	16.89	17.12	17.01	8.0	16.20	1.33920	34.22	551	0.86	10.57	488	0.887	11.3	37.90	4.88	42	3325
3H-2	31.50	31.73	31.61	7.9	18.06	1.33920	34.22	557	0.87	8.28	495	0.888	9.6	37.00	4.77	78	4127
3H-4	32.92	33.14	33.03	7.8	18.34	1.33922	34.33	558	0.87	8.11	495	0.887	8.9	37.50	4.85	59	4074
6X-3	55.18	55.40	55.29	7.7	14.29	1.33931	34.83	563	0.88	10.92	501	0.890	10.1	36.74	5.35	49	4404
7X-3	64.68	64.91	64.79	7.7	13.76	1.33922	34.33	560	0.86	11.28	498	0.889	9.1	37.36	5.50	28	4235
8X-3	74.42	74.71	74.56	7.7	13.48	1.33921	34.28	558	0.88	10.59	496	0.887	9.4	36.64	5.60	21	4073
9X-5	86.52	86.74	86.63	7.8	11.67	1.33925	34.50	552	0.87	13.24	489	0.887	10.2	37.45	6.17	17	3742
10X-2	92.00	92.22	92.11	7.8	13.21	1.33919	34.17	556	0.86	9.76	494	0.889	9.5	35.32	5.37	27	3887
11X-3	102.70	102.94	102.82	7.9	11.92	1.33921	34.28	555	0.88	11.84	492	0.886	10.4	36.74	5.86	6	3548
14X-2	129.73	130.02	129.87	7.9	11.81	1.33929	34.72	555	0.88	13.71	492	0.887	8.8	38.63	6.41	13	3640
16H-2	149.00	149.22	149.11	8.1	4.40	1.33942	35.44	552	0.83	28.07	492	0.891	10.3	45.48	9.14	9	1289
316-C0007D-																	
3R-2	191.42	191.76	191.59	7.7	15.35	1.33895	32.83	553	0.90	1.55	494	0.894	8.5	27.18	5.48	24	3867
4R-1	199.87	199.99	199.93	7.5	11.43	1.33907	33.50	556	0.90	8.08	501	0.902	7.7	28.24	7.47	3	3481
5R-1	209.00	209.42	209.21	7.8	12.02	1.33901	33.17	552	0.92	5.22	500	0.906	8.5	22.94	8.51	7	3589
6R-3	221.44	221.86	221.65	7.7	10.56	1.33899	33.06	553	0.90	6.15	502	0.908	8.4	22.29	8.76	6	3504
7R-1	228.99	229.40	229.19	7.7	10.43	1.33904	33.33	553	0.91	5.82	503	0.910	8.6	21.17	9.07	6	3288
8R-1	238.40	238.90	238.65	8.1	9.66	1.33887	32.39	550	0.92	3.17	498	0.907	8.4	19.38	8.60	3	3450
9R-2	248.65	248.82	248.74	8.0	8.83	1.33888	32.44	551	0.94	3.93	501	0.909	8.7	18.69	8.83	2	3408
9R-2	248.99	249.21	249.10	—	—	1.33890	32.56	550	0.94	5.47	491	0.893	8.8	20.19	9.04	3	3219
10R-1	257.10	257.40	257.25	8.1	9.63	1.33883	32.17	548	0.96	1.49	497	0.908	8.5	17.20	8.80	3	3190
15R-1	304.35	304.70	304.53	8.2	7.83	1.33882	32.11	543	0.89	3.72	497	0.914	7.9	15.79	10.00	4	2760
16R-1	313.95	314.36	314.16	8.3	7.83	1.33887	32.39	548	0.89	2.35	494	0.903	8.9	17.05	10.31	2	2715
17R-3	325.30	325.71	325.50	8.2	7.30	1.33832	29.33	499	0.82	3.95	460	0.922	7.2	12.73	9.67	3	2330
18R-1	332.62	333.04	332.83	8.0	7.62	1.33882	32.11	548	0.92	3.04	499	0.910	7.6	16.69	10.21	6	2234
19R-1	341.81	342.23	342.02	8.1	6.90	1.33885	32.28	542	0.88	6.48	491	0.906	7.9	19.88	10.62	0	2061
20R-1	351.46	351.86	351.66	8.2	8.01	1.33874	31.67	545	0.91	1.46	496	0.910	7.4	14.30	10.90	6	2341
21R-1	361.07	351.88	356.48	8.5	7.77	1.33879	31.94	543	0.89	3.47	493	0.908	8.5	16.30	10.74	4	2177
22R-2	372.19	372.53	372.36	8.7	6.97	1.33876	31.78	544	0.89	2.27	496	0.911	7.4	14.29	11.05	4	1849
23R-3	382.96	383.37	383.16	8.2	7.87	1.33875	31.72	544	0.89	2.74	495	0.910	6.9	14.59	12.30	4	1801
24R-3	392.83	393.24	393.03	8.0	7.94	1.33879	31.94	544	0.88	2.75	492	0.904	7.3	15.74	12.85	4	1665
25R-3	401.87	402.28	402.07	8.0	7.46	1.33885	32.28	544	0.87	4.70	496	0.912	6.5	15.24	13.57	2	1282
26R-1	408.00	408.42	408.21	7.7	5.52	1.33876	31.78	539	0.88	4.21	488	0.906	6.7	15.81	12.83	0	1201
27R-1	417.74	418.01	417.87	7.9	6.47	1.33885	32.28	547	0.87	5.12	497	0.907	6.0	16.86	13.33	2	1289
28R-4	431.37	431.81	431.59	—	—	1.33890	32.56	548	0.86	4.96	—	—	6.6	22.77	10.34	3	1337
29R-1	436.81	437.19	437.00	—	—	1.33902	33.23	556	0.90	0.00	—	—	7.4	22.92	8.61	3	1403

Notes: CSF = core depth below seafloor. Na calculated by charge balance. — = not analyzed.

Table T13. Uncorrected concentrations of minor elements in interstitial waters, Site C0007. (See table notes.)

Core, section	Depth CSF (m)			Minor elements (µm)							
	Top	Bottom	Average	Li	B	Sr	Ba*	Ba†	Si	Fe	Mn
316-C0007A-											
1H-2	1.42	1.67	1.54	25.4	498	79	0.0	0.1	496	2.11	12.21
1H-4	2.73	2.95	2.84	23.7	522	77	0.0	0.2	506	1.00	8.45
316-C0007B-											
1H-2	5.73	5.97	5.85	14.9	477	76	0.0	0.3	491	0.40	1.38
1H-4	9.77	9.99	9.88	9.9	532	73	0.0	0.4	505	3.14	1.75
316-C0007C-											
1H-2	14.05	14.29	14.17	7.9	466	65	0.4	0.8	432	7.25	3.30
1H-5	16.89	17.12	17.01	11.7	421	63	1.3	1.7	347	3.94	2.82
3H-2	31.50	31.73	31.61	13.1	447	59	1.6	2.1	531	16.84	3.65
3H-4	32.92	33.14	33.03	14.0	380	60	1.5	1.9	458	1.81	3.59
6X-3	55.18	55.40	55.29	14.8	304	57	1.2	1.6	437	0.83	5.50
7X-3	64.68	64.91	64.79	12.2	290	59	1.1	1.5	405	0.76	4.03
8X-3	74.42	74.71	74.56	18.9	270	65	1.8	2.3	374	0.59	5.10
9X-5	86.52	86.74	86.63	19.1	265	72	1.6	2.1	392	0.15	4.50
10X-2	92.00	92.22	92.11	16.7	342	73	0.8	1.2	628	5.15	4.01
11X-3	102.70	102.94	102.82	20.7	267	79	1.2	1.6	385	0.81	4.31
14X-2	129.73	130.02	129.87	14.1	286	83	1.1	1.2	449	0.73	4.69
16H-2	149.00	149.22	149.11	23.0	407	83	1.0	1.1	199	0.55	3.38
316-C0007D-											
3R-2	191.42	191.76	191.59	15.3	238	74	11.9	9.7	674	4.28	4.20
4R-1	199.87	199.99	199.93	16.9	292	83	12.7	3.3	708	1.38	7.32
5R-1	209.00	209.42	209.21	18.7	278	86	12.7	11.1	676	1.02	4.83
6R-3	221.44	221.86	221.65	18.3	277	91	13.2	11.4	724	1.01	5.08
7R-1	228.99	229.40	229.19	18.2	257	93	13.5	11.5	639	1.52	5.91
8R-1	238.40	238.90	238.65	20.5	255	96	16.5	14.1	569	0.51	6.83
9R-2	248.65	248.82	248.74	22.9	192	101	18.4	10.0	465	0.56	3.41
9R-2	248.99	249.21	249.10	22.6	195	100	18.9	10.1	520	0.43	4.37
10R-1	257.10	257.40	257.25	27.0	146	104	23.2	20.3	518	0.50	5.02
15R-1	304.35	304.70	304.53	25.4	151	110	18.7	15.8	395	0.66	3.49
16R-1	313.95	314.36	314.16	25.4	177	109	21.6	7.8	444	0.46	4.58
17R-3	325.30	325.71	325.50	26.7	153	97	24.9	9.0	484	0.53	3.60
18R-1	332.62	333.04	332.83	32.8	207	110	41.3	4.3	669	0.48	4.62
19R-1	341.81	342.23	342.02	37.6	191	106	30.5	2.2	538	0.62	4.50
20R-1	351.46	351.86	351.66	49.7	152	119	144.8	9.9	430	0.45	4.69
21R-1	361.07	351.88	356.48	61.9	124	106	80.1	2.5	417	0.45	1.40
22R-2	372.19	372.53	372.36	76.8	159	111	137.6	5.1	539	0.48	3.59
23R-3	382.96	383.37	383.16	82.7	148	111	141.5	5.1	559	0.49	11.15
24R-3	392.83	393.24	393.03	85.5	164	104	47.6	2.6	660	0.55	14.27
25R-3	401.87	402.28	402.07	90.8	155	105	35.1	2.7	693	0.38	17.17
26R-1	408.00	408.42	408.21	100.4	166	103	23.5	6.0	745	0.52	13.74
27R-1	417.74	418.01	417.87	107.0	135	104	59.3	2.4	576	0.32	15.13
28R-4	431.37	431.81	431.59	93.1	218	106	85.0	2.8	575	0.39	8.15
29R-1	436.81	437.19	437.00	80.5	285	108	121.0	5.2	604	0.34	7.63

Notes: * = shipboard ICP-AES, † = shore-based ICP-MS. CSF = core depth below seafloor.

Table T14. Uncorrected concentrations of trace elements and $\delta^{18}O$ in interstitial waters, Site C0007. (**See table notes.**)

Core, section	Depth CSF (m) Top	Bottom	Average	V (nM)	Cu (nM)	Zn (nM)	Rb (µM)	Mo (µM)	Cs (nM)	Pb (nM)	U (nM)	Y (pM)	$\delta^{18}O$ (‰)
316-C0007A-													
1H-2	1.42	1.67	1.54	16.6	8,600	285	1.52	81	2.9	1.2	6.4	1.45	–0.11
1H-4	2.73	2.95	2.84	86.9	4,923	257	1.51	220	3.3	0.6	1.4	0.75	–0.11
316-C0007B-													
1H-2	5.73	5.97	5.85	122.2	8,007	301	1.32	86	2.8	2.1	2.3	0.91	–0.11
1H-4	9.77	9.99	9.88	67.8	4,419	379	1.24	123	3.8	0.9	0.6	0.33	–0.13
316-C0007C-													
1H-2	14.05	14.29	14.17	68.8	5,480	302	1.16	158	4.1	1.0	1.3	0.63	–0.17
1H-5	16.89	17.12	17.01	111	1,951	65	1.28	526	6.3	0.3	3.6	0.88	–0.26
3H-2	31.50	31.73	31.61	52.4	5,125	161	1.09	191	5.2	1.4	1.1	0.90	–0.48
3H-4	32.92	33.14	33.03	48.6	2,194	115	1.11	386	5.7	0.9	1.1	4.9	–0.51
6X-3	55.18	55.40	55.29	31.0	3,773	137	1.23	226	6.7	0.5	1.2	1.11	–0.71
7X-3	64.68	64.91	64.79	47.1	3,625	208	1.16	283	6.4	0.2	2.1	1.27	–0.80
8X-3	74.42	74.71	74.56	28.2	3,688	174	1.21	255	6.9	0.6	1.5	2.5	–1.78
9X-5	86.52	86.74	86.63	25.4	2,996	373	1.23	348	6.3	1.6	2.9	0.82	–0.44
10X-2	92.00	92.22	92.11	28.0	12,122	114	1.03	68	5.5	1.3	2.3	0.86	–1.33
11X-3	102.70	102.94	102.82	32.4	1,595	204	1.33	368	7.3	3.3	1.4	2.2	–0.75
14X-2	129.73	130.02	129.87	24.2	1,204	136	1.25	423	6.1	0.3	2.6	0.52	–0.76
16H-2	149.00	149.22	149.11	14.6	534	254	1.10	418	4.1	0.6	10.0	0.63	–0.68
316-C0007D-													
3R-2	191.42	191.76	191.59	23.3	32,983	357	0.92	57	4.4	2.4	1.4	2.0	–1.63
4R-1	199.87	199.99	199.93	12.0	8,664	240	0.87	86	4.0	2.2	1.3	0.75	–1.49
5R-1	209.00	209.42	209.21	16.1	1,947	73	0.84	167	4.0	0.1	1.4	0.60	–2.46
6R-3	221.44	221.86	221.65	14.3	3,505	143	0.86	168	4.4	0.2	0.9	0.91	–2.18
7R-1	228.99	229.40	229.19	17.0	4,913	138	0.84	115	3.7	1.3	1.3	1.71	–2.51
8R-1	238.40	238.90	238.65	16.8	8,159	164	0.92	132	5.1	1.9	1.4	1.79	–3.18
9R-2	248.65	248.82	248.74	20.2	21,884	82	0.95	235	4.8	1.5	3.6	2.1	–3.18
9R-2	248.99	249.21	249.10	20.3	21,999	116	0.95	236	4.8	1.5	3.6	2.1	—
10R-1	257.10	257.40	257.25	19.1	5,333	32	1.02	290	4.9	0.3	2.1	0.99	–3.37
15R-1	304.35	304.70	304.53	27.9	9,838	81	0.91	376	4.4	2.5	5.5	1.33	–3.23
16R-1	313.95	314.36	314.16	24.9	13,197	198	0.92	444	4.4	2.4	4.5	1.09	–2.96
17R-3	325.30	325.71	325.50	28.1	20,471	38	0.82	380	4.1	1.5	5.4	0.78	–3.54
18R-1	332.62	333.04	332.83	23.0	5,693	387	0.90	266	4.1	1.9	2.0	0.95	–3.46
19R-1	341.81	342.23	342.02	22.8	26,160	33	0.88	333	4.3	0.7	3.4	0.70	–2.58
20R-1	351.46	351.86	351.66	17.1	21,207	81	0.78	141	3.2	0.8	2.7	0.64	–3.70
21R-1	361.07	351.88	356.48	24.3	12,037	5	0.91	67	3.3	0.4	3.0	0.65	–3.06
22R-2	372.19	372.53	372.36	18.7	5,296	17	0.80	247	3.1	0.5	2.8	1.22	–3.27
23R-3	382.96	383.37	383.16	10.8	10,731	24	0.70	227	2.1	2.3	4.5	0.56	–3.23
24R-3	392.83	393.24	393.03	22.0	12,345	69	0.75	480	2.4	4.4	4.6	1.03	–2.84
25R-3	401.87	402.28	402.07	13.1	28,420	137	0.62	118	1.9	2.0	4.1	0.46	–2.77
26R-1	408.00	408.42	408.21	10.7	27,895	105	0.62	222	1.9	2.9	4.5	0.59	–2.08
27R-1	417.74	418.01	417.87	9.5	24,881	165	0.53	183	2.0	5.3	4.6	0.80	–1.93
28R-4	431.37	431.81	431.59	7.5	23,254	49	0.55	186	3.2	52.6	3.4	0.96	–1.15
29R-1	436.81	437.19	437.00	8.8	27,990	167	0.63	395	2.8	19.8	3.5	0.46	–1.16

Notes: CSF = core depth below seafloor. — = not analyzed.

Table T15. Headspace gas composition for safety monitoring in sediments, Site C0007. (**See table notes.**)

Core, section, interval (cm)	Depth CSF (m)	Headspace gas (ppmv)		
		Methane	Ethane	C_1/C_2
316-C0007A-				
1H-1, 137.5–141.5	1.40	2.3	0.0	—
316-C0007B-				
1H-1, 136.5–140.5	4.53	3.1	0.0	—
316-C0007C-				
1H-1, 137–141	14.03	3.7	0.0	—
3H-1, 136.5–140.5	31.48	3.5	0.0	—
6X-1, 136.5–140.5	53.98	18.9	0.0	—
7X-1, 136.5–140.5	63.48	6.9	0.0	—
8X-1, 138–142	72.99	9.2	0.0	—
9X-1, 137–141	82.48	4.1	0.0	—
10X-1, 136.5–140.5	91.98	4.5	0.0	—
11X-1, 138–142	101.49	9.0	0.0	—
12X-1, 37.5–41.5	109.99	49.9	0.0	—
14X-1, 109.5–113.5	129.71	5.4	0.0	—
16H-1, 136.5–140.5	148.98	2.5	0.0	—
17H-1, 137–141	158.48	2.1	0.0	—
316-C0007D-				
3R-1, 138–142	191.40	2,535.4	1.8	1,442.5
4R-1, 90–94	200.42	4,018.0	2.2	1,829.5
5R-1, 136.5–140.5	210.39	5,439.8	0.0	—
6R-1, 136.5–140.5	219.89	11,372.6	3.2	3,509.4
7R-1, 136–140	229.38	15,597.3	4.0	3,872.7
8R-1, 137–141	238.89	10,677.8	3.7	2,922.0
9R-1, 138–142	248.40	7,162.4	2.5	2,922.0
10R-1, 137.5–141.5	257.90	6,853.0	1.9	3,683.5
11R-1, 50–54	266.52	10,906.7	2.8	3,906.4
15R-1, 136.5–140.5	304.89	6,756.8	2.4	2,764.5
16R-1, 137.5–141.5	314.40	5,220.4	0.0	—
17R-1, 133–137	323.85	11,721.5	3.4	3,411.7
18R-1, 136.5–140.5	333.39	12,090.0	3.6	3,375.2
19R-1, 137–141	342.89	11,300.8	5.1	2,235.0
20R-1, 138–142	352.40	8,409.2	3.3	2,520.4
21R-1, 136–140	361.88	5,441.4	0.0	—
22R-1, 137–141	371.39	4,413.4	1.7	2,638.8
23R-1, 136.5–140.5	380.89	8,371.4	2.3	3,715.6
24R-1, 137–141	390.39	8,518.1	2.5	3,450.4
25R-1, 139–143	399.91	5,081.5	2.4	2,088.4
26R-1, 137.5–141.5	409.40	4,797.8	1.8	2,681.6
27R-1, 115.5–119.5	418.68	2,680.4	2.0	1,348.8
28R-1, 137.5–141.5	428.40	6,857.6	0.0	—
29R-1, 136.5–140.5	437.89	6,774.9	0.0	—

Notes: CSF = core depth below seafloor. — = not applicable.

Table T16. Hydrocarbon gas concentration from additional headspace gas analysis, Site C0007. (See table notes.) (Continued on next page.)

Core, section, interval (cm)	Depth CSF (m)	Headspace gas (ppmv)			Headspace gas (µM)	
		Methane	Ethane	C_1/C_2	Methane	Ethane
316-C0007A-						
1H-1, 137.5–141.5	1.40	10.1	0.0	—	2	0.00
1H-4, 18–22	2.93	13.6	0.0	—	3	0.00
316-C0007B-						
1H-1, 136.5–140.5	4.53	17.4	0.0	—	4.1	0.00
1H-2, 114.5–118.5	5.71	4.7	0.0	—	2	0.00
1H-4, 136.5–140.5	7.35	16.50	0.0	—	5	0.00
1H-6, 18–22	8.97	16.66	0.0	—	4	0.00
1H-8, 137–141	11.38	9.2	0.0	—	2.55	0.00
316-C0007C-						
1H-1, 137–141	14.03	16.1	0.0	—	5	0.00
1H-3, 115–119	15.46	14.8	0.0	—	4	0.00
1H-4, 137.5–141.5	16.87	13.0	0.0	—	3	0.00
1H-7, 136.5–140.5	19.70	35.4	0.0	—	7	0.00
3H-1, 136.5–140.5	31.48	37.9	0.0	—	13	0.00
3H-3, 115.5–119.5	32.90	29.7	0.0	—	8	0.00
3H-5, 116–120	34.32	19.0	0.0	—	6	0.00
3H-7, 0–4	35.76	13.3	0.0	—	3	0.00
3H-7, 138.5–142.5	37.14	11.5	0.0	—	2	0.00
3H-9, 118–122	39.76	19.8	0.0	—	5	0.00
4H-CC, 0–5	39.62	22.8	0.0	—	7	0.00
5X-1, 0–4	43.21	44.7	0.0	—	14	0.00
6X-1, 136.5–140.5	53.98	47.2	0.0	—	11	0.00
6X-2, 114–118	55.16	47.5	0.0	—	14	0.00
6X-4, 81–85	56.23	40.7	0.0	—	9	0.00
7X-1, 136.5–140.5	63.48	51.9	0.0	—	10	0.00
7X-2, 114.5–118.5	64.66	43.2	0.0	—	13	0.00
7X-4, 137–141	66.30	65.7	0.0	—	16	0.00
7X-5, 136.5–140.5	67.70	48.0	0.0	—	15	0.00
7X-6, 25.5–29.5	68.00	91.3	0.0	—	31	0.00
8X-1, 138–142	72.99	59.5	0.0	—	18	0.00
8X-2, 136.5–140.5	74.40	41.9	0.0	—	10	0.00
8X-4, 109.5–113.5	75.82	96.0	0.0	—	24	0.00
8X-5, 136.5–140.5	77.23	77.5	0.0	—	15	0.00
8X-6, 64–68	77.91	60.2	0.0	—	13	0.00
9X-1, 137–141	82.48	109.3	0.0	—	25	0.00
9X-2, 136.5–140.5	83.89	88.0	0.0	—	20	0.00
9X-4, 117–121	86.50	85.8	0.0	—	19	0.00
9X-6, 137–141	88.13	97.9	0.0	—	27	0.00
9X-7, 136–140	89.53	99.2	0.0	—	30	0.00
10X-1, 136.5–140.5	91.98	31.2	0.0	—	12	0.00
10X-3, 115–119	93.39	40.7	0.0	—	17	0.00
10X-4, 79.5–83.5	94.23	150.3	0.3	46	55	1.20
11X-1, 138–142	101.49	29.8	0.0	—	11	0.00
11X-2, 115–119	102.68	23.0	0.0	—	8	0.00
12X-1, 37.5–41.5	109.99	66.3	0.0	—	33	0.00
14X-1, 109.5–113.5	129.71	13.0	0.0	—	6	0.00
16H-1, 136.5–140.5	148.98	8.7	0.0	—	2	0.00
17H-1, 137–141	158.48	1.6	0.0	—	1	0.00
316-C0007D-						
3R-1, 138–142	192.09	1,439.7	0.0	—	807	0.00
4R-1, 33–37	200.30	7,978.4	2.5	3,227	2,457	0.76
4R-1, 90–94	200.87	3,642.0	0.0	—	1,996	0.00
5R-1, 41.5–45.5	210.12	10,098.8	3.1	3,231	2,394	0.74
5R-1, 136.5–140.5	211.07	8,198.5	2.3	3,536	2,667	0.75
6R-1, 136.5–140.5	220.57	14,756.4	3.4	4,350	3,676	0.84
6R-3, 136–140	222.52	11,925.7	3.3	3,641	3,535	0.97
7R-1, 94.5–98.5	229.65	12,835.6	3.1	4,089	5,293	1.29
8R-1, 137–141	239.58	7,860.5	2.9	2,748	1,971	0.72
9R-1, 138–142	249.09	5,551.5	2.0	2,773	1,693	0.61
10R-1, 137.5–141.5	258.58	9,532.5	2.7	3,480	3,378	0.97
11R-1, 50–54	266.77	14,308.9	3.4	4,261	4,249	1.00
16R-1, 137.5–141.5	315.08	6,374.4	2.2	2,858	2,024	0.71
16R-2, 137.5–141.5	316.50	9,662.9	3.5	2,735	2,921	1.07
17R-1, 133–137	324.52	7,837.3	2.8	2,778	2,869	1.03
17R-2, 138.5–142.5	325.97	4,134.7	2.2	1,899	1,266	0.67

Table T16 (continued).

Core, section, interval (cm)	Depth CSF (m)	Headspace gas (ppmv)			Headspace gas (μM)	
		Methane	Ethane	C_1/C_2	Methane	Ethane
18R-1, 136.5–140.5	334.07	7,872.8	2.7	2,927	1,931	0.66
18R-3, 138.5–142.5	336.92	9,570.5	4.2	2,272	2,837	1.25
19R-1, 137–141	343.58	11,131.6	4.8	2,338	2,939	1.26
20R-1, 138–142	353.09	6,596.7	4.0	1,631	1,828	1.12
20R-2, 136.5–140.5	354.49	9,062.2	4.4	2,052	2,390	1.16
21R-1, 136–140	362.56	2,882.3	0.0	—	886	0.00
22R-1, 137–141	372.08	5,661.7	2.3	2,513	1,315	0.52
22R-3, 140–144	374.94	4,067.1	0.0	—	2,238	0.00
23R-1, 136.5–140.5	381.57	2,747.9	0.0	—	1,211	0.00
23R-4, 0–4	384.37	2,632.2	0.0	—	1,216	0.00
24R-1, 137–141	391.08	7,819.8	2.5	3,108	1,959	0.63
24R-3, 137–141	393.92	1,811.8	0.0	—	426	0.00
24R-4, 138–141	395.34	3,931.1	2.1	1,845	1,324	0.72
25R-1, 139–143	400.61	5,085.9	3.0	1,701	1,458	0.86
25R-3, 137–141	403.44	5,240.2	5.2	1,011	1,285	1.27
26R-1, 137.5–141.5	410.08	7,680.1	3.4	2,271	1,684	0.74
27R-1, 115.5–119.5	419.25	2,371.7	1.9	1,223	562	0.46
28R-1, 137.5–141.5	429.08	6,550.7	2.0	3,336	1,354	0.41
28R-3, 137–141	431.91	5,929.0	0.0	—	1,287	0.00
29R-2, 0–4	438.53	6,490.1	0.0	—	1,256	0.00
31R-CC, 0–4	455.82	8,632.4	0.0	—	1,861	0.00

Notes: CSF = core depth below seafloor. — = not applicable.

Table T17. Carbonate, carbon, nitrogen, and sulfur in sediments, Site C0007. (See table notes.)

Core, section, interval (cm)	Depth CSF (m)	$CaCO_3$ (wt%)	TOC (wt%)	TN (wt%)	C/N	TS (wt%)
316-C0007A-						
1H-2, 0–1.5	1.42	2.60	0.44	0.06	7.72	0.06
1H-4, 0–1.5	2.73	4.71	0.35	0.05	7.53	0.46
1H-CC, 21–22.5	3.16	5.07	0.35	0.05	7.37	0.47
316-C0007B-						
1H-1, 66–67.5	3.81	3.88	0.41	0.05	7.95	0.71
1H-3, 0–1.5	5.74	0.95	0.07	0.01	4.90	1.14
1H-6, 15–16.5	8.93	2.20	0.43	0.04	9.95	0.73
1H-7, 0–1.5	9.78	1.97	0.48	0.05	9.05	0.45
316-C0007C-						
1H-1, 60–61.5	13.25	1.99	0.40	0.05	8.87	0.34
1H-2, 0–1.5	14.06	2.53	0.50	0.06	8.81	0.21
1H-5, 0–1.5	16.90	1.01	0.28	0.03	8.39	0.48
3H-2, 0–1.5	31.50	1.53	0.26	0.04	7.39	0.21
3H-3, 103–104.5	32.76	2.01	0.43	0.06	6.95	0.08
3H-4, 0–1.5	32.93	2.22	0.46	0.06	8.33	0.17
3H-5, 60–61.5	33.75	0.57	0.42	0.06	6.64	0.06
6X-2, 75.5–77	54.76	3.07	0.40	0.06	6.63	0.04
6X-3, 0–1.5	55.18	1.26	0.30	0.05	6.01	0.11
6X-4, 55.5–57	55.96	1.33	0.35	0.05	6.63	0.09
6X-CC, 22.5–24	56.48	3.12	0.51	0.07	6.90	0.09
7X-1, 95–96.5	63.05	1.13	0.26	0.04	6.10	0.12
7X-3, 0–1.5	64.69	2.15	0.57	0.06	10.11	0.16
7X-4, 39–40.5	65.30	2.37	0.43	0.05	7.89	0.13
7X-5, 102–103.5	67.34	2.40	0.48	0.05	9.36	0.15
8X-2, 15–16.5	73.17	1.25	0.17	0.04	4.71	0.10
8X-3, 0–1.5	74.42	0.83	0.27	0.04	7.10	0.14
8X-5, 64–65.5	76.49	1.59	0.72	0.07	10.13	0.62
9X-1, 65–66.5	81.75	4.32	0.71	0.08	8.58	0.10
9X-5, 0–1.5	86.52	1.63	0.57	0.05	11.76	0.19
9X-6, 40–41.5	87.14	2.42	0.58	0.06	9.64	0.22
10X-1, 111–112.5	91.71	1.28	0.40	0.06	6.16	0.07
10X-2, 0–1.5	92.00	1.98	0.58	0.07	8.52	0.15
10X-CC, 6–7.5	94.31	0.85	0.12	0.03	4.33	0.05
11X-1, 22.5–24	100.32	1.06	0.33	0.05	7.10	0.38
11X-2, 56–57.5	102.08	2.26	0.54	0.07	7.22	0.11
11X-3, 0–1.5	102.71	1.11	0.19	0.04	5.29	0.05
11X-4, 67–68.5	103.61	2.65	0.28	0.04	7.32	0.70
11X-CC, 21–22.5	103.84	0.68	0.11	0.02	4.39	0.08
14X-2, 0–1.5	129.73	1.20	0.38	0.04	9.76	0.18
16H-2, 0–1.5	149.00	0.30	0.09	0.02	5.26	0.12
316-C0007D-						
3R-2, 0–1.5	191.43	1.45	0.43	0.05	8.53	0.89
3R-3, 69–70.5	192.46	1.29	0.30	0.04	6.99	0.14
4R-1, 37–38.5	199.88	1.69	0.48	0.06	7.79	0.09
5R-1, 0–1.5	209.01	2.61	0.23	0.04	5.76	0.09
6R-3, 98.5–100	221.45	2.39	0.51	0.06	8.12	0.22
7R-1, 98.5–100	228.99	2.34	0.41	0.06	6.99	0.11
8R-1, 90–91.5	238.41	2.54	0.39	0.05	7.95	0.25
9R-2, 23–24.5	248.66	2.80	0.35	0.05	7.29	0.24
9R-2, 77.5–79	249.20	2.56	0.40	0.06	6.87	0.13
10R-1, 50–51.5	257.01	2.07	0.32	0.06	5.66	0.05
15R-1, 85–86.5	304.36	3.17	0.47	0.06	7.87	0.32
16R-1, 95–96.5	313.96	0.43	0.43	0.09	4.65	0.22
16R-2, 100–101.5	315.42	1.91	0.47	0.06	8.28	0.10
17R-3, 0–1.5	325.30	1.71	0.46	0.06	7.81	0.13
17R-CC, 10–10.5	327.12	0.53	0.43	0.05	8.05	0.07
18R-1, 24–25.5	332.25	3.88	0.46	0.06	7.37	0.08
18R-1, 62–63.5	332.63	5.74	0.47	0.06	8.25	0.08
19R-1, 31–32.5	341.82	3.48	0.38	0.05	7.24	0.09
20R-1, 84.5–86	351.85	0.23	0.26	0.05	5.43	0.06
21R-1, 57–58.5	361.08	0.52	0.11	0.04	2.90	0.03
22R-1, 47–48.5	370.48	3.97	0.35	0.06	5.69	0.34
22R-2, 78–112	372.36	5.59	0.22	0.04	5.05	0.33
22R-3, 97–98.5	373.80	0.80	0.35	0.06	5.75	0.24
23R-2, 23–24.5	381.14	3.44	0.43	0.07	6.18	0.33
23R-2, 113–114.5	382.04	0.30	0.36	0.06	5.59	0.78
23R-3, 62–63.5	382.96	1.03	0.24	0.04	5.45	0.37
23R-4, 14–15.5	383.89	1.96	0.48	0.07	6.77	0.35
24R-1, 16.5–18	389.17	5.05	0.46	0.07	6.78	0.12
24R-2, 105.5–107	391.47	0.49	0.40	0.07	6.01	0.13
24R-3, 66.5–68	392.51	0.35	0.49	0.07	6.57	0.15
24R-3, 98.5–100	392.83	0.21	0.34	0.06	5.89	0.23
24R-5, 42–43.5	395.09	0.64	0.54	0.08	6.97	0.43
25R-2, 80–81.5	400.74	0.78	0.40	0.07	5.91	0.24
25R-3, 50–51.5	401.87	0.63	0.50	0.08	6.34	0.49
26R-1, 0–1.5	408.01	1.73	0.40	0.07	5.47	0.64
26R-1, 133.5–135	409.34	1.43	0.32	0.06	5.24	0.19
27R-1, 24–25.5	417.75	1.63	0.33	0.06	5.15	0.24
28R-4, 12–13.5	431.37	1.31	0.34	0.07	4.95	0.31
29R-1, 31–32.5	436.82	6.99	0.34	0.06	5.26	0.15

Notes: CSF = core depth below seafloor. TOC = total organic carbon, TN = total nitrogen, TS = total sulfur.

Table T18. Sample depth and processing for microbiological and biogeochemical studies, Site C0007. (See table notes.)

Core, section	Depth CSF (m)	Frozen –80°C	Frozen –20°C	Anaerobic pack (4°C)	Slurry (–20°C) FISH	Slurry (–20°C) Acetone
316-C0007A-						
1H-2	1.54	X			X	
1H-3	2.25	X			X	X
1H-3	2.34			X		
1H-3	2.40			X		
1H-3	2.63	X		X	X	
1H-3	2.68	X				
1H-3	2.79		X			
1H-4	2.84	X			X	
316-C0007B-						
1H-1	4.17	X			X	X
1H-1	4.32			X		
1H-3	5.85	X			X	
1H-5	7.95	X				
1H-5	7.98		X			
1H-5	8.10	X		X	X	
1H-5	8.18			X	X	
1H-7	9.98	X			X	
1H-10	12.33	X				
1H-10	12.33			X	X	X
316-C0007C-						
1H-1	14.04	X			X	
1H-3	15.01			X		
1H-3	15.07	X			X	
1H-3	15.12	X			X	X
1H-3	15.29	X		X	X	
1H-3	15.36			X		
1H-3	15.42	X				
1H-3	15.47		X			
1H-4	16.88	X			X	
3H-1	30.18	X			X	X
3H-1	30.32			X		
3H-1	30.48	X		X	X	
3H-1	30.54	X				
3H-1	30.60			X		
3H-1	30.63		X			
3H-1	31.49	X			X	
3H-3	32.92	X			X	
6X-1	53.27		X			
6X-1	53.32	X				
6X-1	53.46	X		X	X	
6X-1	53.54			X		
6X-1	53.69	X			X	X
6X-1	53.99	X			X	
6X-2	55.17	X			X	
7X-2	64.67	X			X	
7X-4	66.31	X			X	
8X-1	72.29	X			X	
8X-1	72.38	X			X	X
8X-1	72.53			X		
8X-1	72.68	X		X	X	
8X-1	72.75	X				
8X-1	72.79		X			
8X-2	74.41	X			X	
9X-4	86.51	X			X	
9X-7	89.54	X			X	
10X-1	91.99	X			X	
10X-3	92.72	X			X	X
10X-3	92.87			X		
10X-3	93.03	X		X	X	
10X-3	93.10	X				
10X-3	93.14		X			
11X-2	102.69	X			X	
14X-1	129.72	X			X	
16H-1	148.75			X		
16H-1	148.90	X			X	X
16H-1	148.99	X			X	
17H-1	157.69	X		X	X	X
316-C0007D-						
3R-1	191.41	X			X	
3R-2	191.58	X			X	
5R-1	209.21		X			
5R-1	209.92		X			
5R-1	210.40	X			X	
6R-3	221.65	X			X	
6R-3	221.85	X			X	
7R-1	229.19	X			X	
8R-1	238.59	X			X	
9R-1	248.19	X			X	X
9R-1	248.19		X			
10R-1	257.42	X			X	
12R-CC	279.71	X				
5R-1	290.54	X				
5R-1	297.54	X		X		
15R-1	303.75	X			X	X
15R-1	303.75			X		
15R-1	303.75		X	X		
15R-1	303.75	X				
10R-1	304.20		X			
5R-1	304.54	X			X	X
15R-1	304.90	X			X	
16R-1	314.16	X			X	
16R-2	315.82	X			X	
17R-3	325.50	X			X	
18R-1	332.83	X			X	
18R-1	333.40	X			X	
19R-1	342.02	X			X	
15R-1	352.67		X			
20R-2	353.76	X			X	X
20R-2	353.76			X		
20R-2	353.76	X		X		
20R-2	353.76	X				
20R-3	353.89	X			X	X
20R-3	353.89			X		
20R-3	353.89	X		X		
20R-3	353.89	X				
20R-1	354.49		X			
9R-1	356.10			X		
9R-1	356.10		X	X		
9R-1	356.10	X				
21R-1	361.23	X			X	
22R-2	372.36	X			X	
23R-3	383.16	X			X	
24R-3	393.03	X			X	
25R-2	400.16	X			X	X
25R-2	400.16			X		
25R-2	400.16	X		X		
25R-2	400.16	X				
25R-2	400.16		X			
26R-1	408.21	X			X	
27R-1	417.87	X			X	
28R-4	431.59	X			X	
29R-1	437.00	X			X	X
35R-1	484.24	X			X	

Notes: CSF = core depth below seafloor. FISH = fluorescence in situ hybridization.

Table T19. Thermal conductivity measurements, Site C0007. (See table notes.)

Core, section, interval (cm)	Depth CSF (m)	Method*	Thermal conductivity (W/[m·K])		N	Standard deviation (W/[m·K])	Thermal conductivity (W/[m·K])‡
			Raw average	Calibrated†			
316-C0007A-							
1H-1, 40	0.40	V10305	0.97	0.92	3	0.01	0.95
1H-3, 30	2.00	V10305	1.09	1.05	3	0.02	1.08
316-C0007B-							
1H-1, 50	3.60	V10305	1.16	1.12	3	0.01	1.15
1H-2, 55	5.10	V10305	1.03	0.99	3	0.02	1.02
1H-4, 55	6.50	V10305	1.18	1.14	2	0.00	1.18
1H-6, 50	9.30	V10305	1.28	1.24	3	0.00	1.28
1H-9, 60	10.80	V10305	1.30	1.26	3	0.01	1.30
316-C0007C-							
1H-1, 55	13.20	V10305	1.24	1.20	3	0.01	1.24
1H-4, 50	16.00	V10305	1.35	1.32	3	0.00	1.36
1H-6, 40	17.50	V10305	1.37	1.33	2	0.00	1.37
1H-7, 30	18.60	V10305	1.34	1.30	2	0.01	1.34
1H-8, 25	20.00	V10305	1.45	1.41	2	0.00	1.45
3H-1, 40	30.50	V10305	1.43	1.39	2	0.00	1.43
3H-3, 50	32.20	V10305	1.31	1.27	3	0.00	1.31
3H-5, 50	33.60	V10305	1.33	1.29	2	0.01	1.33
3H-9, 110	39.70	V10305	1.32	1.28	2	0.01	1.33
6X-1, 40	53.00	V10305	1.01	0.96	3	0.03	0.99
6X-2, 30	54.30	V10305	1.47	1.43	3	0.01	1.48
6X-4, 65	56.00	V10305	1.35	1.31	3	0.01	1.36
7X-1, 50	62.60	V10305	1.39	1.36	3	0.01	1.40
7X-2, 50	64.00	V10305	1.33	1.29	3	0.00	1.33
7X-4, 50	65.40	V10305	1.33	1.29	3	0.00	1.33
7X-5, 50	66.80	V10305	1.42	1.39	2	0.19	1.43
7X-5, 115	67.50	V10305	1.44	1.40	3	0.01	1.44
8X-1, 40	72.00	V10305	1.20	1.16	3	0.02	1.19
8X-2, 60	73.60	V10305	1.35	1.31	3	0.00	1.35
8X-4, 60	75.30	V10305	1.29	1.25	3	0.02	1.28
8X-6, 20	77.40	V10305	1.11	1.07	3	0.01	1.10
9X-1, 60	81.70	V10305	1.01	0.97	3	0.03	1.00
9X-3, 30	84.20	V10305	1.19	1.15	3	0.01	1.18
9X-6, 40	87.10	V10305	1.26	1.22	3	0.02	1.25
9X-8, 50	90.10	V10305	1.40	1.36	3	0.01	1.40
10X-1, 85	91.40	V10305	1.22	1.18	3	0.00	1.22
10X-3, 20	92.40	V10305	1.21	1.17	2	0.02	1.21
10X-3, 30	92.50	V10305	1.41	1.37	3	0.01	1.41
10X-4, 30	93.70	V10305	1.26	1.22	3	0.01	1.26
11X-1, 60	100.70	V10305	1.40	1.36	3	0.02	1.40
11X-2, 60	102.10	V10305	1.24	1.20	3	0.03	1.24
11X-2, 100	102.50	V10305	1.16	1.12	3	0.06	1.16
11X-4, 40	103.30	V10305	1.39	1.35	3	0.00	1.40
12X-1, 34	109.90	V10305	1.68	1.65	2	0.01	1.70
14X-1, 80	129.40	V10305	1.37	1.33	3	0.04	1.37
316-C0007D-							
3R-1, 62	190.60	V10305	1.19	1.15	3	0.07	1.19
3R-3, 40	192.20	V10305	1.25	1.21	3	0.01	1.25
4R-1, 30	199.80	V10305	1.08	1.03	3	0.01	1.06
5R-2, 56	211.00	V10305	1.07	1.02	3	0.01	1.06
8R-1, 53	238.00	V10305	1.31	1.27	3	0.03	1.31
8R-2, 9	239.00	V10305	1.09	1.04	2	0.03	1.08
19R-2, 103	343.90	H10304	1.29	1.25	10	0.02	1.29
21R-1, 97	361.50	H10304	1.04	0.99	3	0.02	1.02
22R-1, 71	370.70	H10304	1.30	1.26	5	0.01	1.30
22R-4, 45	374.70	H10304	1.33	1.29	7	0.08	1.32
23R-2, 7	381.00	H10304	1.29	1.25	4	0.04	1.29
23R-4, 22	384.00	H10304	1.27	1.23	5	0.00	1.27
24R-1, 70	389.70	H10304	1.32	1.28	9	0.04	1.32
26R-1, 90	408.90	H10304	1.30	1.26	7	0.02	1.29

Notes: * = V10305 refers to full-space needle probe and H10404 refers to half-space line source, † = thermal conductivities were adjusted based on calibration formulas and constants given in the "Expedition 316 methods" chapter, ‡ = thermal conductivities were corrected for temperature and pressure as described in the "Expedition 316 methods" chapter. CSF = core depth below seafloor.

Table T20. Temperature measurements, Hole C0007C. (See table notes.)

Core	Tool	Depth CSF (m)	BWT (°C)	Time delay (s)	Fit		Equilibrium temperature (°C)
					Start (s)	End (s)	
316-C0007C-							
1H	APCT3	12.60	1.64	3.7	60	693	2.51
2H	APCT3	30.10	1.65	20.7	60	852	3.29
4H	APCT3	43.10	1.57	11.5	60	815	3.95
5X	SET	52.60	1.56	81.1	111	531	4.07
8X	SET	81.10	—	27.8	60	705	5.44

Notes: CSF = core depth below seafloor. BWT = bottom water temperature. APCT3 = advanced piston corer temperature tool, SET = sediment temperature. — = not measured.